



HELLENIC REPUBLIC  
UNIVERSITY OF IOANNINA  
SCHOOL OF ENGINEERING  
DEPARTMENT OF MATERIALS SCIENCE AND ENGINEERING

Development and study of low-dimensional hybrid and nanocomposite materials  
based on layered nanostructures

Antonios Kouloumpis

DOCTORAL THESIS

Ioannina, 2017







**ΕΛΛΗΝΙΚΗ ΔΗΜΟΚΡΑΤΙΑ  
ΠΑΝΕΠΙΣΤΗΜΙΟ ΙΩΑΝΝΙΝΩΝ  
ΠΟΛΥΤΕΧΝΙΚΗ ΣΧΟΛΗ  
ΤΜΗΜΑ ΜΗΧΑΝΙΚΩΝ ΕΠΙΣΤΗΜΗΣ ΥΛΙΚΩΝ**

Ανάπτυξη και μελέτη χαμηλοδιάστατων υβριδικών και νανοσύνθετων υλικών με  
βάση φυλλόμορφες νανοδομές

Αντώνιος Κουλουμπής

ΔΙΔΑΚΤΟΡΙΚΗ ΔΙΑΤΡΙΒΗ

Ιωάννινα, 2017





HELLENIC REPUBLIC  
UNIVERSITY OF IOANNINA  
SCHOOL OF ENGINEERING  
DEPARTMENT OF MATERIALS SCIENCE AND ENGINEERING

Development and study of low-dimensional hybrid and nanocomposite  
materials based on layered nanostructures

Antonios Kouloumpis

DOCTORAL THESIS

Ioannina, 2017



*«Η έγκριση της διδακτορικής διατριβής από το Τμήμα Μηχανικών Επιστήμης Υλικών της Πολυτεχνικής Σχολής του Πανεπιστημίου Ιωαννίνων δεν υποδηλώνει αποδοχή των γνωμών του συγγραφέα Ν. 5343/32, άρθρο 202, παράγραφος 2».*





**Ημερομηνία αίτησης του κ. Αντωνίου Κουλουμπή: 07/02/2013****Ημερομηνία**

**ορισμού Τριμελούς Συμβουλευτικής Επιτροπής: 01/03/2013**

**Μέλη Τριμελούς Συμβουλευτικής Επιτροπής:**

Επιβλέπων:

Δημήτριος Γουρνής, Καθηγητής του Τμήματος Μηχανικών Επιστήμης Υλικών της Πολυτεχνικής Σχολής του Πανεπιστημίου Ιωαννίνων

Μέλη:

Δημήτριος Γουρνής, Καθηγητής του Τμήματος Μηχανικών Επιστήμης Υλικών της Πολυτεχνικής Σχολής του Πανεπιστημίου Ιωαννίνων

Μιχαήλ Καρακασίδης, Καθηγητής του Τμήματος Μηχανικών Επιστήμης Υλικών της Πολυτεχνικής Σχολής του Πανεπιστημίου Ιωαννίνων

Αθανάσιος Μπουρλίνος, Επίκουρος Καθηγητής του τμήματος Φυσικής της Σχολής Θετικών Επιστημών του Πανεπιστημίου Ιωαννίνων

**Ημερομηνία ορισμού θέματος: 01/03/2013**

Ανάπτυξη και μελέτη χαμηλοδιάστατων υβριδικών και νανοσύνθετων υλικών με βάση φυλλόμορφες νανοδομές

**ΔΙΟΡΙΣΜΟΣ ΕΠΤΑΜΕΛΟΥΣ ΕΞΕΤΑΣΤΙΚΗΣ ΕΠΙΤΡΟΠΗΣ : 28/11/2016**

- |                             |  |
|-----------------------------|--|
| <b>Δημήτριος Γουρνής,</b>   | Καθηγητής του Τμήματος Μηχανικών Επιστήμης Υλικών της Πολυτεχνικής Σχολής του Πανεπιστημίου Ιωαννίνων.               |
| <b>Μιχαήλ Καρακασίδης</b>   | Καθηγητής του Τμήματος Μηχανικών Επιστήμης Υλικών της Πολυτεχνικής Σχολής του Πανεπιστημίου Ιωαννίνων.               |
| <b>Αθανάσιος Μπουρλίνος</b> | Επίκουρος Καθηγητής του Τμήματος Φυσικής της Σχολής Θετικών Επιστημών του Πανεπιστημίου Ιωαννίνων.                   |
| <b>Petra Rudolf</b>         | Καθηγήτρια του Zernike Institute for Advanced Materials, RUG   |
| <b>Αλκιβιάδης Παϊπέτης</b>  | Καθηγητής του Τμήματος Μηχανικών Επιστήμης Υλικών της Πολυτεχνικής Σχολής του Πανεπιστημίου Ιωαννίνων.               |
| <b>Χαράλαμπος Σταμάτης</b>  | Καθηγητής του Τμήματος Βιολογικών Εφαρμογών και Τεχνολογιών της Σχολής Επιστημών Υγείας του Πανεπιστημίου Ιωαννίνων. |
| <b>Γεώργιος Φρουδάκης</b>   | Καθηγητής του Τμήματος Χημείας της Σχολής Θετικών και Τεχνολογικών Επιστημών του Πανεπιστημίου Κρήτης.               |

Έγκριση Διδακτορικής Διατριβής με βαθμό «ΑΡΙΣΤΑ» στις 15/09/2017

**Ο Πρόεδρος του Τμήματος**

**Η Γραμματέας του Τμήματος**

**Καρακασίδης Μιχαήλ  
Καθηγητής**

**Ξανθή Τουτουτζόγλου**



**Date of application Mr. Antonios Kouloumpis, 07/02/2013**

**Date of appointing Three Membered Advisory committee: 01/03/2013**

**Three Membered Advisory committee:**

Supervisor

Dimitrios Gournis, Professor of Department of Materials Science & Engineering,  
School of Engineering of the University of Ioannina

Members

Dimitrios Gournis, Professor of Department of Materials Science & Engineering,  
School of Engineering of the University of Ioannina

Michael Karakassides, Professor of Department of Materials Science & Engineering,  
School of Engineering of the University of Ioannina

Athanasios Bourlinos, Assistant Professor of The Physics Department of School of  
Sciences of the University of Ioannina

**Date of thesis definition: 01/03/2013**

Development and study of low-dimensional hybrid and naocomposite materials based on layered nanostructures

**SEVEN MEMBERED COMMITTEE ASSIGNATION: 28/11/2016**

**Dimitrios Gournis** Professor of Department of Materials Science & Engineering,  
School of Engineering of the University of Ioannina

**Michael Karakassides** Professor of Department of Materials Science & Engineering,  
School of Engineering of the University of Ioannina

**Athanasios Bourlinos** Assistant Professor of Physics Department, School of Sciences  
of the University of Ioannina

**Petra Rudolf** Professor of Zernike Institute for Advanced Materials of RUG,  
University of Groningen.

**Alkiviadis Paipetis** Professor of Department of Materials Science & Engineering,  
School of Engineering of the University of Ioannina

**Haralambos Stamatis** Professor of Department of Biological Applications &  
Technologies, School of Medical Sciences of University of  
Ioannina

**Georgios Froudakis** Professor of Chemistry Department, School of Sciences &  
Engineering of University of Crete.

**Approval Dissertation with grade "EXCELLENT" on 15/09/2017**

**The President of the Department**

**The Secretary of the Department**

**Karakasidis Michael**

**Xanthi Toutounzoglou**

**Professor**



## Περίληψη

Οι εξαιρετικές φυσικοχημικές ιδιότητες και η υψηλή ειδική επιφάνεια των 2D υλικών, τα καθιστούν ιδιαίτερα ελκυστικά σε μια πληθώρα εφαρμογών. Ανάμεσα σε άλλα μπορούν να χρησιμοποιηθούν ως πλατφόρμες για την ενσωμάτωση διαφορετικών συστάδων, μορίων ή νανοϋλικών επιτρέποντας τη δημιουργία υβριδίων και σύνθετων υλικών με νέες ή βελτιωμένες ιδιότητες. Από την άλλη πλευρά, η σπουδαιότητα της παρασκευής στρώμα με στρώμα (layer-by-layer) υβριδικών υμενίων, έγκειται στο γεγονός του ελέγχου της αρχιτεκτονικής, του πάχους, και της λειτουργικότητας των σχηματιζόμενων νανοδομών.

Τα κεφάλαια της παρούσας διδακτορικής διατριβής επικεντρώνονται στην ανάπτυξη και μελέτη χαμηλοδιάστατων υβριδικών υμενίων αποτελούμενων από ανόργανες φυλλόμορφες νανοδομές όπως το γραφένιο και το γερμανάνιο, κάνοντας χρήση της μεθόδου Langmuir-Blodgett (LB).

Η τεχνική Langmuir-Blodgett είναι μια από τις πιο ελπιδοφόρες στρώμα-με-στρώμα τεχνικές για την προετοιμασία λεπτών υμενίων με ποικίλες συστάσεις στρωμάτων (οργανικές ή/και ανόργανες νανοδομές). Αυτή η bottom-up προσέγγιση δίνει τη δυνατότητα για τον ακριβή έλεγχο του πάχους του μονοστρώματος ενώ επιτρέπει την ομοιογενή εναπόθεσή του σε μεγάλες περιοχές και επιφάνειες με υψηλό βαθμό δομικής τάξης. Πολυάριθμες μελέτες έχουν αναφερθεί τα τελευταία χρόνια, στην τροποποίηση των φύλλων γραφενίου με την LB τεχνική με σκοπό την παραγωγή υβριδικών λεπτών υμενίων για την βελτιστοποίηση των οπτοηλεκτρονικών και μηχανικών ιδιοτήτων του γραφενίου. Αυτά τα μονοστρωματικά ή πολυστρωματικά συστήματα με τις εξαιρετικές ιδιότητες, χρησιμοποιούνται σε ένα μεγάλο εύρος εφαρμογών, από ηλεκτρονικά συστήματα, φωτοβολταϊκά ως και αισθητήρες όπως περιγράφεται στο 2<sup>ο</sup> κεφάλαιο.

Ένα μεγάλο μέρος της επιστημονικής έρευνας σχετικά με το γραφένιο επικεντρώνεται στη χρήση του ως δομικό στοιχείο για την ανάπτυξη νέων υβριδικών νανοδομών με σαφώς καθορισμένες διαστάσεις και ιδιότητες, κατάλληλες για εφαρμογές όπως η αποθήκευση αερίων, η ετερογενή κατάλυση, ο διαχωρισμός αερίων/υγρών, οι νανοαισθητήρες και η βιοϊατρική. Προς την κατεύθυνση αυτή, στο 3<sup>ο</sup> κεφάλαιο περιγράφεται μια bottom-up προσέγγιση, η οποία συνδυάζει την αυτο-οργάνωση με την τεχνική εναπόθεσης Langmuir-Schaefer (LS) με σκοπό την δημιουργία υβριδικών υμενίων με βάση το γραφένιο στο οποίο περιέχονται μόρια φουλερενίων ( $C_{60}$ ) εντός του ενδοστρωματικού χώρου του φυλλόμορφου υλικού.

Συμπερασματικά, παρατηρήθηκε ότι η παρουσία των μορίων  $C_{60}$  στον ενδωστρωματικό χώρο του γραφενίου οδηγεί σε αύξηση της ηλεκτρικής αγωγιμότητας του υβριδικού υμενίου συγκριτικά με το οργανο-τροποποιημένο γραφένιο. Τέτοια υβριδικά υλικά σαν το αυτό του γραφενίου/φουλερενίου μπορούν να χρησιμοποιηθούν ως υλικά σε εφαρμογές όπως τα διαφανή ηλεκτρόδια, τα τρανζίστορ ή ως υπερπυκνωτές.

Μια περαιτέρω έρευνα για την ανάπτυξη υβριδικών υμενίων με βάση το γραφένιο στο οποίο περιέχονται παράγωγα μόρια των  $C_{60}$  παρουσιάζεται στο 4<sup>ο</sup> κεφάλαιο. Πιο συγκεκριμένα, φουλερόλια ( $C_{60}(OH)_{24}$ ) και βρώμο-φουλερένια ( $C_{60}Br_{24}$ ) εντέθηκαν ανάμεσα στα φύλλα οξειδίου του γραφενίου (GO) συνδυάζοντας την τεχνική Langmuir-Schaefer με ένα ή δύο στάδια της τεχνικής αυτο-οργάνωσης, αντίστοιχα. Τα υβριδικά λεπτά υμένια χαρακτηρίστηκαν με μια πληθώρα τεχνικών με στόχο την επιβεβαίωση της ύπαρξης των παραγώγων των φουλερενίων ανάμεσα στα φύλλα του GO. Όπως παρατηρήθηκε από τις μετρήσεις διαβροχής το υβριδικό σύστημα ODA-GO- $C_{60}(OH)_{24}$ , παρουσιάζει έναν πιο υδρόφοβο χαρακτήρα συγκριτικά με το σύστημα ODA-GO-HEX- $C_{60}Br_{24}$  υποδηλώνοντας ότι η υδροφοβικότητα δεν εξαρτάται από τις λειτουργικές ομάδες των αρχικών νανοϋλικών αλλά από την σχηματιζόμενη μορφολογία του υβριδικού συστήματος. Τα παραγόμενα υβριδικά λεπτά υμένια με βάση το γραφένιο στο οποίο περιέχονται παράγωγα των  $C_{60}$  μορίων συνιστούν νέα υβριδικά συστήματα που θα μπορούσαν να χρησιμοποιηθούν ως ιδανικά νανοϋλικά για εφαρμογές στα οπτοηλεκτρονικά συστήματα, στα φωτοβολταϊκά, στα φάρμακα καθώς επίσης και στον τομέα της φωτοκατάλυσης.

Στο 5<sup>ο</sup> κεφάλαιο, περιγράφεται η ενσωμάτωση νανοτελειών άνθρακα (C-dots) στη δομή του γραφενίου για πρώτη φορά, κάνοντας χρήση μιας τροποποιημένης Langmuir-Schaefer τεχνικής. Πιο συγκεκριμένα νέα υβριδικά πολυστρωματικά υμένια αποτελούμενα από οξείδιο του γραφενίου και εντεθειμένες φωτοβόλες νανοτελείες άνθρακα παρασκευάστηκαν συνδυάζοντας την τεχνική Langmuir-Schaefer με την τεχνική της αυτο-οργάνωσης. Ο ακριβής έλεγχος σε συνδυασμό με την ομοιογενή εναπόθεση, καθιστά την LS τεχνική ιδανική για την πρόληψη της συσσωμάτωσης των νανοδομών άνθρακα σε υβριδικά συστήματα, όπως τα φουλερένια και οι νανοτελείες άνθρακα. Οι νανοτελείες άνθρακα, με μέση διάμετρο 4 nm, παρήχθησαν με πυρόλυση υποβοηθούμενη από μικροκύματα, η οποία είναι μια προτιμητέα μέθοδος εξαιτίας τους χαμηλού κόστους, της εύκολης εγκατάστασης και της αποτελεσματικότητάς της. Τα υβριδικά πολυστρωματικά υμένια αποτελούμενα

από εντεθειμένες νανοτελείες άνθρακα ανάμεσα στα φύλλα του οξειδίου του γραφενίου, παρουσίασαν ελεγχόμενη διαφάνεια ανάλογα με την προσαρμογή του αριθμού των εναποθεθειμένων στρωμάτων. Τέλος, τα υβριδικά πολυστρωματικά υμένια εμφανίζουν υψηλής ποιότητας φωτοφωταύγεια με στενές εκπομπές γεγονός που οφείλεται στην επιτυχημένη ενσωμάτωση των νανοτελειών άνθρακα ανάμεσα σε φύλλα γραφενίου. Αυτά τα πολυστρωματικά υμένια αποτελούν ένα καινοτόμο υβριδικό σύστημα κατάλληλο για μια πληθώρα εφαρμογών όπως οι νανοανιχνευτές, οι οπτοηλεκτρονικές διατάξεις και τα διαφανή ηλεκτρόδια, καθώς επίσης και σε συστήματα χορήγησης φαρμάκων.

Το γερμανάνιο (GeH), ένα ανάλογο του γραφενίου, έχει προσελκύσει πρόσφατα ιδιαίτερο ενδιαφέρον λόγω των οπτοηλεκτρονικών ιδιοτήτων του καθώς και λόγω της σταθερότητάς του. Η υψηλή κινητικότητα των ηλεκτρονίων, το μη μηδενικό ενεργειακό χάσμα και οι χαμηλές διαστάσεις καθιστούν το γερμανάνιο ένα πολλά υποσχόμενο δισδιάστατο υλικό για μια πληθώρα εφαρμογών υψηλής απόδοσης. Στο 6<sup>ο</sup> κεφάλαιο, το γερμανάνιο παρασκευάστηκε σε θερμοκρασία περιβάλλοντος με μία καινούρια μέθοδο σύνθεσης βασισμένη στην τοποτακτική απένθεση της φάσης  $\beta$ -CaGe<sub>2</sub> σε υδατικό διάλυμα HF. Επιπλέον χρησιμοποιήθηκε η οργάνωση Langmuir-Schaefer για τον έλεγχο της πυκνότητας των αποφυλλοποιημένων νανοφυλλιδίων γερμανανίου, με σκοπό την δημιουργία νέων μονοστρωματικών υμενίων. Η επικάλυψη, η ομοιομορφία και ο έλεγχος της οργάνωσης σε μονοατομικό επίπεδο επιβεβαιώθηκαν από τις π-A ισόθερμες καμπύλες καθώς και από την μικροσκοπία ατομικών δυνάμεων (AFM). Η αντιμικροβιακή δράση του γερμανανίου σε υδατική διασπορά καθώς και σε μορφή μονοστρωματικού υμενίου διερευνήθηκε για πρώτη φορά με τη βοήθεια της μεθόδου πλάκας μικροτίτλου και των βιώσιμων κυττάρων επιβίωσης σε επιφάνειες επικαλυπτόμενες με γερμανάνιο, αντίστοιχα. Σύμφωνα με τα αποτελέσματα η αντιμικροβιακή δράση του γερμανανίου εξαρτάται από τη δομική διαφορά των κυτταρικών μεμβρανών και τη σύνθεση του κυτταρικού τοιχώματος των Gram-αρνητικών και Gram-θετικών βακτηριδίων. Πιο συγκεκριμένα, τα αποτελέσματα της υδατικής διασποράς του γερμανίου αποκάλυψαν ότι κατά τη διάρκεια των πρώτων έξι ωρών η βακτηριακή ανάπτυξη καταστέλλεται πολύ έντονα ενώ μία εξαιρετική αντιμικροβιακή δράση των υμενίων γερμανανίου παρατηρήθηκε για τα βακτηριακά στελέχη *Brevibacterium*. Τα μονοατομικά υμένια που παρασκευάστηκαν με την μέθοδο Langmuir-Schaefer θα μπορούσαν να εφαρμοστούν



στο μέλλον ως αντιμικροβιακές επιφάνειες υψηλών αποδόσεων σε νοσοκομεία καθώς επίσης και στη βιομηχανία τροφίμων.

## Summary

The extraordinary physicochemical properties and the high specific area of 2D materials render them very attractive for a plethora of potential applications; they can be used as platforms for integrating different moieties, clusters, molecules or nanomaterials into hybrids, allowing for the creation of composites with new or enhanced properties. On the other hand, the importance of preparing layer-by-layer hybrid films relies on the ability to control the architecture, the thickness, and the functionality of the formed nanostructures.

The aim of this thesis focuses on the development and study of novel low-dimensional films and hybrids based on layered nanomaterials such as graphene and germanane, assembled with the help of the Langmuir-Blodgett (LB) technique.

The Langmuir-Blodgett technique is one of the most promising layer-by-layer methods for preparing thin films with varying layer composition (organic or/and inorganic nanostructures). This bottom-up approach allows to accurately control the thickness of the deposited film and allows for a homogeneous deposition over large areas with a high degree of structural order. Numerous studies have been reported during the past years concerning the assembly of graphene sheets and different building blocks by the LB method in order to produce hybrid thin films with enhanced optoelectronic and mechanical properties. Such single layer or multilayer systems can be employed in a variety of different application areas such as in electronics, solar cells and sensors, as described in Chapter 2.

Much of the research effort on graphene focuses on its use in the development of new hybrid nanostructures suitable for applications in gas storage, heterogeneous catalysis, gas/liquid separations, nanosensing, and biomedicine. Towards this aim, in Chapter 3 we describe a bottom-up approach, which combines the self-assembly with the Langmuir-Schaefer (LS) deposition technique in order to fabricate graphene-based layered hybrid materials that host fullerene molecules within the interlayer space. As was revealed by conductivity measurements, the presence of C<sub>60</sub> within the interlayer spacing lowers the resistivity of the hybrid material as compared to the pure organo-graphene matrix. This graphene/fullerene hybrid could ideally be used as transparent electrodes as well as in thin film transistors or supercapacitors.

Motivated by the previous work, a further investigation of graphene-based hybrid thin films fabricated by the same bottom-up approach but hosting fullerene derivatives was reported in Chapter 4. More specifically, fullerols (C<sub>60</sub>(OH)<sub>24</sub>) and

bromo-fullerenes ( $C_{60}Br_{24}$ ) molecules were integrated in graphene oxide (GO) layers by combining the Langmuir-Schaefer technique with one and two self-assembly steps respectively. The hybrid thin films were characterized by a variety of techniques in order to prove the presence of the fullerene derivatives between the GO layers. Moreover, wetting experiments revealed that the ODA-GO- $C_{60}(OH)_{24}$  hybrid system exhibits a more hydrophobic character than ODA-GO-HEX- $C_{60}Br_{24}$ , suggesting that the hydrophobicity doesn't depend on the functional groups of the pristine nanomaterials but on the morphology of the hybrid system. These novel fullerene-based hybrid films could be candidates for potential applications in photovoltaics, sensors, or optoelectronic devices as well as in photocatalysis and drug delivery.

In Chapter 5 a new class of highly ordered hydrophilic luminescent carbon dot (C-dot) intercalated graphene oxide structures was reported for the first time; the material was produced by combining the Langmuir-Schaefer method with self-assembly. The precise thickness control combined with homogeneous deposition makes the LS technique ideal for preventing aggregation of carbon-based nanostructures such as fullerene or carbon dots in hybrid systems. C-dots with a mean diameter of 4 nm were produced by microwave-assisted pyrolysis, which is a convenient method because it is low-cost, facile and efficient. The transparency of the hybrid multilayers consisting of C-dots sandwiched between graphene oxide showed could be controlled by adjusting the number of the deposited layers. The high quality photoluminescence with narrow emissions of C-dots is preserved in these multilayer films. These novel hybrid systems are suitable for applications such as nanoprobe, optoelectronic devices and transparent electrodes as well as for drug delivery.

Germanane (GeH), the germanium graphane-analogue has recently attracted considerable interest due to its high mobility, non-zero band gap and optoelectronic properties. In Chapter 6, we describe how germanane was produced at room temperature by a new synthetic approach based on the topotactic deintercalation of  $\beta$ - $CaGe_2$  in aqueous HF solution. The exfoliated germanane nanosheets can be assembled into deposited monolayer films with different packing density exploiting the Langmuir-Schaefer method. The coverage, uniformity and single-layer level control of the assembly was confirmed by  $\pi$ -A isotherms and AFM measurements. The antimicrobial activity of germanane in aqueous dispersion and in monolayers form was investigated for the first time. Our results revealed that an antimicrobial effect of germanane for Gram-negative and Gram-positive bacteria, with an

especially outstanding activity against *Brevibacterium* bacterial strains. The monolayers produced by the Langmuir-Schaefer might be applied in the future as high efficiency antimicrobial surfaces in hospitals and in the food industry.

## ΠΡΑΚΤΙΚΟ

της Επαγγελματικής Εξεταστικής Επιτροπής για την αναγνώριση σε διδάκτορα του Τμήματος Μηχανικών Επιστήμης Υλικών του Πανεπιστημίου Ιωαννίνων του κ. **Αντώνη Κουλουμπή**.

Η Ειδική Διατμηματική Επιτροπή (ΕΔΕ) του ΔΠΜΣ «Χημεία και Τεχνολογία Υλικών» του Πανεπιστημίου Ιωαννίνων στη συνεδρίαση της αριθμ. 30/21.06.2017 όστερα από την κρίση της Τριμελούς Συμβουλευτικής Επιτροπής ότι η ερευνητική εργασία του υποψήφιου διδάκτορος κ. **Αντώνη Κουλουμπή** έχει ολοκληρωθεί και έχει κατατεθεί στο Τμήμα, όρισε σύμφωνα με το άρθρο 12 παρ.5 εδ. Β του Ν.2083/92, και το άρθ. 9 παρ.4 εδ. α του Ν. 3685/2008 Επταμελή Εξεταστική Επιτροπή που αποτελείται από τους κ.κ. **Δημήτριο Γουρνή** Καθηγητή του ΤΜΕΥ του Πανεπιστημίου Ιωαννίνων, **Μιχαήλ Καρακυσίδη** Καθηγητή και Πρόεδρο του ΤΜΕΥ του Πανεπιστημίου Ιωαννίνων, **Petra Rudolf** Καθηγήτρια στο Zernike Institute for Advanced Materials του University of Groningen (Ολλανδίας), **Αλκιβιάδη Παϊσιήτη** Καθηγητή του ΤΜΕΥ του Πανεπιστημίου Ιωαννίνων, **Χαράλαμπο Σταμάτη**, Καθηγητή του Τμήματος Βιολογικών Εφαρμογών και Τεχνολογιών του Πανεπιστημίου Ιωαννίνων, **Γεώργιος Φρουδάκης** Καθηγητή του Τμήματος Χημείας του Πανεπιστημίου Κρήτης, και **Αθανάσιο Μπουρλίνο** Επίκουρο Καθηγητή του Τμήματος Φυσικής του Πανεπιστημίου Ιωαννίνων, για να αναπτύξει ενόπιον της ο υποψήπιος διδάκτορας κ. **Αντώνης Κουλουμπής** τη διατριβή του με θέμα: «Ανάπτυξη και μελέτη χαμηλοδιάστατων υβριδικών και νανοσύνθετων υλικών με βάση φυλλάμορφες νανοδομές».

Η Επταμελής Εξεταστική Επιτροπή, συνήλθε σήμερα 15 Σεπτεμβρίου 2017 ημέρα Παρασκευή και ώρα 11:00 μ.μ. στο χώρο του Νέου Κτιρίου του ΤΜΕΥ του Πανεπιστημίου Ιωαννίνων για να εξετάσει την διδακτορική διατριβή του υποψήφιου διδάκτορα κ. **Αντώνη Κουλουμπή**. Ο Καθηγητής κ. Γεώργιος Φρουδάκης συμμετείχε στην διαδικασία μέσω τηλεδιάσκεψης όπως είχε ενημερώσει με έγγραφο του (στον Πρόεδρο της Εξεταστικής Επιτροπής κ. Δ. Γουρνή).

Χρή προέδρου της Εξεταστικής Επιτροπής ανέθεσαν τα μέλη της στον κ. **Δημήτριο Γουρνή**, Καθηγητή του Τμήματος Μηχανικών Επιστήμης Υλικών του Πανεπιστημίου Ιωαννίνων.

Στο σημείο αυτό, τίθεται υπόψη της 7μελούς Εξεταστικής Επιτροπής το αρθ. 36 του Ν.1268/82, τα αρθ. 12 και 13 του Ν. 2083/92 και το άρθ. 9 παρ.4 εδ. α του Ν. 3685/2008 και τα αρθ. 40 και 41 του Εσωτερικού Κανονισμού Λειτουργίας του Πανεπιστημίου Ιωαννίνων (ΦΕΚ 310/10.03.05 τ. 2<sup>ο</sup>). Τα μέλη της Επιτροπής έλαβαν

εγκρίρας (15 Ιουνίου 2017) και μελέτησαν τη διατριβή της υποψήφιας.

Ο υποψήφιος κ. Αντώνης Κουλούμητς ανέπτυξε ενώπιον της Επιτροπής τη διατριβή του με θέμα: «Ανάπτυξη και μελέτη χαμηλοδιάστατων υβριδικών και νανοσύνθετων υλικών με βάση φυλλόμορφες νανοδομές» τονίζοντας τα σημεία, στα οποία κατά τη γνώμη του η διατριβή είναι πρωτότυπη και αποτελεί συμβολή στην επιστήμη.

Τα μέλη της Εξεταστικής Επιτροπής απρόβουαν ερωτήσεις στον υποψήφιο, μετά την προφορική ανάπτυξη απ' αυτόν του θέματος. Η ανάπτυξη και οι ερωτήσεις έγιναν σε δημόσια συνεδρίαση.

Στη συνέχεια το ακροατήριο και η υποψήφια αποχώρησαν και τα μέλη της Εξεταστικής Επιτροπής συσκέφθηκαν και ψήφισαν, υπέρ της παραδοχής της διατριβής, με ψήφους επτά ( 7 ) και κατά μηδέν ( 0 ).

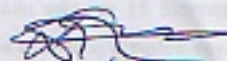
Πρότειναν, δε, με ψήφους έξι ( 7 ) έναντι μηδενός ( 0 ) το βαθμό **Λιπστα** εφαρμόζοντας την παρ. 6 του αρθ. 40 του Εσωτερικού Κανονισμού Λειτουργίας του Πανεπιστημίου Ιωαννίνων (ΦΕΚ 310/10.03.05 τ. 2\*).

Το παρόν πρακτικό μετά την υπογραφή του από τα υπόλοιπα μέλη της Επταμελούς Εξεταστικής Επιτροπής αποστέλλει ταχυδρομικώς στον Καθηγητή κ. Γεώργιο Φρουδάκη για την έγκρισή και τη σύμφωνη γνώμη του.

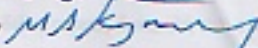
Ιωάννινα, 15 Σεπτεμβρίου 2017

#### Η Εξεταστική Επιτροπή


1. Δημήτριος Γουρνής, Καθ. του ΤΜΕΥ του Παν/μίου Ιωαννίνων



2. Μιχαήλ Καρακωσίδης, Καθ. του ΤΜΕΥ του Παν/μίου Ιωαννίνων



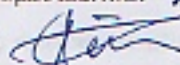
3. Petra Rudolf, Καθ. στο Zentke Inst. for Adv. Mater. του University of Goettingen



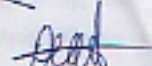
4. Χαρόλαμπος Σταμάτης, Καθ. του Τμ. Βιολ. Ερ. Τεχν. του Παν/μίου Ιωαννίνων



5. Αλκιβιάδης Παϊπέτης, Καθ. του ΤΜΕΥ του Παν/μίου Ιωαννίνων



6. Αθανάσιος Μπουράνης, Επισκ. Καθ. του Τμ. Φυσικής του Παν/μίου Ιωαννίνων



7. Γεώργιος Φρουδάκης, Καθ. του Τμ. Χημείας του Παν/μίου Κρήτης

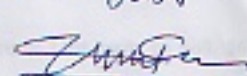


# Table of Contents

<b>Chapter 1: Introduction</b> .....	1
1.1 Layered nanomaterials .....	2
1.1.1 Graphene .....	3
1.1.2 Graphene oxide.....	4
1.1.3 Germanane .....	4
1.2 0D Carbon Nanoallotropes .....	5
1.2.1 Fullerenes .....	6
1.2.2 Carbon Dots .....	6
1.3 Langmuir-Blodgett technique.....	7
1.4 Outline of the thesis .....	7
1.5 References .....	9
<b>Appendix A: Characterization techniques</b> .....	11
A.1 FTIR spectroscopy .....	11
A.2 Raman spectroscopy .....	11
A.3 X-ray photoelectron spectroscopy .....	11
A.4 X-ray diffraction .....	12
A.5 Thermal analysis .....	12
A.6 UV-Vis spectroscopy .....	13
A.7 Photoluminescence spectroscopy .....	13
A.8 Nuclear magnetic resonance .....	13
A.9 Contact angle measurements.....	14
A.10 Scanning electron microscopy.....	14
A.11 Electrical conductivity measurements.....	14
A.12 Atomic force microscopy .....	15
A.13 References of Appendix A.....	15

**Chapter 2: Graphene-based hybrids through the Langmuir-Blodgett approach.....17**

2.1 Introduction .....	18
2.2 Monolayers of Graphene Oxide.....	19
2.3 Nanocomposite films .....	23
2.4 Applications and properties of LB thin films.....	25
2.5 Conclusions .....	31
2.6 References .....	32

**Chapter 3: A bottom-up approach for the synthesis of highly ordered fullerene-intercalated graphene hybrids.....35**

3.1 Introduction.....	36
3.2 Experimental Section.....	38
3.2.1 Materials .....	38
3.2.2 Synthesis of graphene oxide.....	38
3.2.3 Preparation of hybrid graphene/fullerene multilayers.....	38
3.3 Results and Discussion .....	40
3.3.1 Structure control of hybrid ODA-GO layer.....	40
3.3.2 Characterization of hybrid graphene/fullerene multilayers .....	42
3.4 Conclusions .....	48
3.5 References .....	49

**Chapter 4: Controlled deposition of fullerene derivatives within a graphene template by means of a modified Langmuir-Schaefer method.....53**

4.1 Introduction.....	54
4.2 Experimental Section.....	56
4.2.1 Materials .....	56
4.2.2 Synthesis of Graphene Oxide .....	56
4.2.3 Synthesis of fullerene derivatives.....	57



4.2.4 Preparation of hybrid multilayers of graphene oxide and C <sub>60</sub> -derivatives .....	57
4.3 Results-discussion.....	59
4.3.1 Structural characterization of C <sub>60</sub> derivatives .....	59
4.3.2 Structural control of hybrid monolayers.....	62
4.4 Conclusions .....	70
4.5 References .....	72

## **Chapter 5: Graphene/carbon-dot hybrid thin films prepared by a modified Langmuir-Schaefer method.....79**

5.1 Introduction.....	80
5.2 Experimental Section .....	82
5.2.1 Materials .....	82
5.2.2 Synthesis of graphene oxide.....	82
5.2.3 Synthesis of C-dots .....	82
5.2.4 Preparation of hybrid graphene/C-dots multilayers.....	83
5.3 Results and Discussion .....	84
5.3.1 Structural and morphological characterization of pristine C-dots.....	84
5.3.2 Structural control and characterization of hybrid ODA-GO/C-dot monolayers.....	86
5.3.3 Characterization of graphene/C-dot hybrid films.....	88
5.4 Conclusions .....	94
5.5 References .....	96

## **Appendix B.....101**

B.1 Experimental procedures .....	101
B.1.1 Preparation of hydrophobic quartz substrates .....	101
B.1.2 Deposition of isolated C-dots on Si-wafers for the AFM measurements ....	102
B.2 Characterization of pristine C-dots.....	103
B.3 References of Appendix B .....	108

<b>Chapter 6: Germanane: improved synthesis and application as antimicrobial agent</b> .....	109
6.1 Introduction .....	110
6.2 Experimental Section.....	114
6.2.2 Materials .....	114
6.2.3 Synthesis of Germanane.....	114
6.2.4 Preparation of germanane monolayers.....	115
6.2.5 Bacterial strains and growth media.....	116
6.2.6 Preparation of bacteria and treatment of germanane .....	116
6.3 Results and Discussion .....	118
6.3.1 Structural and morphological characterization of germanane.....	118
6.3.2 Structural control and characterization of GeH monolayers.....	121
6.3.3 Antimicrobial activity of germanane .....	125
6.4 Conclusions .....	128
6.5 References .....	130
<b>Summary</b> .....	137
<b>Samenvatting</b> .....	141
<b>Περίληψη</b> .....	145
<b>Acknowledgements</b> .....	149
<b>Publications</b> .....	153
<b>Curriculum Vitae</b> .....	157

# Chapter 1

## Introduction

This thesis comprises a representative part of a joint effort aimed at the development and study of novel types of low dimensional hybrid films based on layered nanomaterials like graphene and germanane by the use of the Langmuir-Blodgett technique. For a complete list of all the projects in which I participated in the past 6 years I refer the reader to the list of my publications at the end of this dissertation.

Considering the great physiochemical properties of layered nanomaterials in combination with the advantages of Langmuir-Blodgett method, the purpose of this research is to offer an insight into the formation process, structural details and properties of the produced 2D hybrid nanostructures. The described fabrication routes allow one to create entirely novel architectures whose final structure is encoded in the shape and properties of the clusters or moieties that are used.

The various chapters of this thesis can be read individually and demonstrate the potential use of hybrid thin films in a wide range of applications including optoelectronics, transparent electrodes, supercapacitors, sensors, photovoltaics, conductive inks as well as in biological and medical applications.

## 1.1 Layered nanomaterials

Layered nanomaterials are composed of two-dimensional (2D) layers of covalently bonded atoms, hold together by van den Waals forces. Ever since the use of natural clays in Upper Palaeolithic period (26.000-30.000 BC),<sup>1,2</sup> to the isolation of graphene in 2004 (single-layer of graphite), 2D materials have attracting enormous industrial and scientific interest because with the reduced dimensionality of their building blocks come very special physical and chemical properties.<sup>3</sup> These layered compounds can be built up from very different elements, their layers can be flat or buckled; examples are layered double hydroxides (LDHs), transition metal dichalcogenides (TMDs), transition metal oxides (TMOs) and 2D compounds such as BN, Bi<sub>2</sub>Te<sub>3</sub> and Bi<sub>2</sub>Se<sub>3</sub>.<sup>4,5</sup> A classification of layered nanomaterials is presented in Table 1.1. A high-throughput prediction of novel two-dimensional materials has identified close to 5000 layered materials by screening more than 300,000 three-dimensional structures from several crystallographic databases<sup>6</sup> and systematically checking for the absence of chemical bonds between adjacent layers.<sup>6</sup> Their structural characteristics and in particular their high surface area, combined with their often exotic electronic properties, make layered materials ideal for a wide range of diverse applications in (opto)electronics, spintronics, nanosensing, gas and energy storage, biomedical technology and drug delivery.<sup>7</sup> In this context it is particularly important that layered materials can be used as component for the development of novel hybrid nanostructures with well-defined dimensions and behaviour.

In this PhD thesis the Langmuir-Blodgett (LB) technique was used to form novel low dimensional films based on layered materials, namely graphene and germanane in order to investigate their structure and properties. More specifically graphene oxide was used as a platform to form hybrid multilayer systems hosting a variety of 0D carbon allotropes (fullerene molecules and carbon dots). Finally germanane was produced by a new synthetic approach and tested as antimicrobial agent. In the next paragraphs these materials will be shortly introduced.

**Table 1.1** Families of layered nanomaterials.

<p><b>Graphene family</b></p> <p><b>Graphene</b> <b>Graphene Oxide</b> <b>BCN</b> (B,N co-doped graphene) <b>Fluorographene</b></p>	<p><b>2D Chalcogenides</b></p> <p><b>Transition Metal Dichalcogenides</b> MoS<sub>2</sub>, ZrSe<sub>2</sub>, TaS<sub>2</sub>, NbSe<sub>2</sub> etc. <b>Transition Metal Trichalcogenides</b> AMo<sub>3</sub>X, NbX<sub>3</sub>, TiX<sub>3</sub>, X=S, Se or Te <b>Metal Phosphorous Trichalcogenides</b> (MPX<sub>3</sub>)</p>	<p><b>2D Oxides</b></p> <p><b>Transition metal oxides</b> Ti oxides, Nb oxides, Mn oxides, Vanadium oxide <b>Trioxides</b> MoO<sub>3</sub>, TaO<sub>3</sub> &amp; hydrated WO<sub>3</sub> <b>Perovskites-type &amp; niobates</b> LaNb<sub>2</sub>O<sub>7</sub>, CaLaNb<sub>2</sub>TiO<sub>10</sub>, Bi<sub>4</sub>Ti<sub>3</sub>O<sub>12</sub>, etc</p>
<p><b>Graphene analogues</b></p> <p><b>h-BN</b> (white graphene) <b>Germanene</b> <b>Silicene</b> <b>Germanene</b></p>	<p><b>Clays-LDHs</b></p> <p><b>2:1 Layered silicates</b> Smectites, Talc, etc <b>1:1 Layered silicates</b> Kaolite, halloysite <b>Layered Double Hydroxides</b></p>	<p><b>Oxychalcogenides &amp; oxypnictide:</b> (Ch, chalcogenide) &amp; derivatives LaOCuCh <b>Oxyhalides of transition metals</b> VOCl, CrOCl, FeOCl, NbO<sub>2</sub>F, WO<sub>2</sub>Cl<sub>2</sub>, FeMoO<sub>4</sub>Cl</p>
<p><b>Metal halides</b></p> <p><b>Transition-metal dihalides</b> MoCl<sub>2</sub> <b>Metal halides</b> MX<sub>3</sub> <b>Layer-type halides</b> MX<sub>4</sub>, MX<sub>5</sub>, MX</p>	<p><b>Layered semiconductors</b></p> <p><b>GaX, InX</b> X = S, Se, Te <b>Zirconium Phosphates &amp; Phosphonates</b> CaHPO<sub>4</sub></p>	<p><b>Ternary Transition Metal Carbides &amp; Nitrides</b></p> <p><b>Derivatives from MAX phases</b> M = transition metal; A=Al or Si; &amp; X=C or N, such as Ti<sub>3</sub>C<sub>2</sub></p>

### 1.1.1 Graphene

Graphene is a one-atom-thick planar sheet of sp<sup>2</sup>-bonded carbon atoms that are arranged in a honeycomb crystal lattice, as shown in Figure 1.1 (left). The isolation and discovery of the surprising electronic properties of graphene in 2004 by Andre Geim and Konstantin Novoselov (yielding in 2010 the Nobel Prize in Physics) started a scientific revolution around the unique electronic, mechanical, thermal and optical properties of this 2D material. The extraordinary electron mobility, combined with its high thermal and mechanical stability, chemical inertness, large surface area, elasticity and the possibility to electrochemically modify the electronic structure place graphene at the top of the list of candidates for the development of new nanomaterials for a plethora of applications.<sup>8-10</sup>

Graphane, a hydrogenated form of graphene with formula unit (CH)<sub>n</sub>, was predicted in 2007<sup>11</sup> and the first experimental confirmation was reported two years later by exposing pristine graphene to atomic hydrogen.<sup>12</sup> The addition of hydrogen to graphene causes a new configuration of the original flat monoatomic graphite layer because all carbon atoms in the resulting lattice change their hybridization from

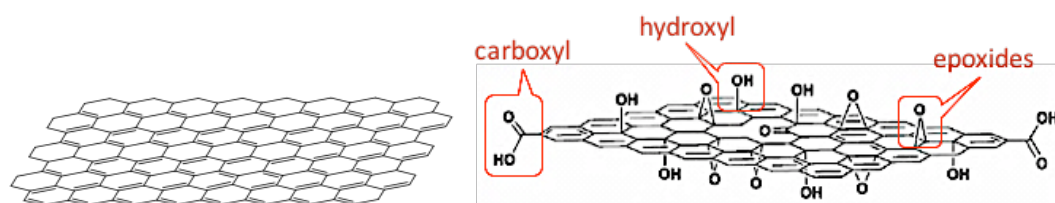


**Figure 1.1.** Schematic representation of graphene (left) and graphene oxide (right) structures.

the flat  $sp^2$  to the tetrahedral  $sp^3$  (bonded to one hydrogen atom)<sup>13</sup> without damaging or changing the pristine 2D hexagonal structure. This process transforms the conducting graphene into insulating graphene with a band gap around 3.5 eV<sup>11</sup> and renders it an ideal candidate for hydrogen storage applications.<sup>11</sup>

### 1.1.2 Graphene oxide

Graphene oxide (GO) is a graphene derivative with covalently attached oxygen-containing groups. GO exhibits a lamellar structure with distributed unoxidized aromatic regions ( $sp^2$ -carbon atoms), six-membered aliphatic regions ( $sp^3$ -carbon atoms) and a high concentration of exposed oxygen-containing functional groups such as, hydroxyl, epoxy and carboxyl, as shown in Figure 1.1 (right). These functional groups are created by strong oxidation and distributed randomly on the basal planes and edges of the GO sheets. Due to the existence of such hydrophilic groups, GO is an excellent host matrix for the accommodation of a variety of moieties (long chain aliphatic hydrocarbons, hydrophilic molecules, transition metal ions and polymers) in the interlayer space and promising for the fabrication of thin films with fascinating properties.

### 1.1.3 Germanane

Germanane (GeH), the germanium graphene-analogue (Figure 1.2) has recently attracted considerable interest due to its remarkable combination of expected properties.

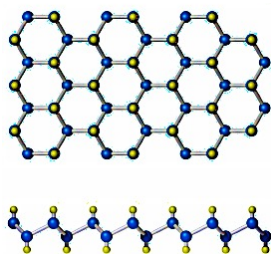


**Figure 1.2.** Schematic representation of the germanane (GeH) structure.

The predicted high mobility of GeH makes it an extremely suitable 2D material for electronic and optoelectronic applications, while its non-zero band gap and low dimensionality promise well for short channel field effect transistors with high on-off ratios and low quiescent currents<sup>14</sup> as well as for photocatalysis applications.<sup>15</sup> Moreover, Germanane's large spin-orbit coupling should allow to explore novel physical phenomena such as quantum spin Hall effect at room temperature.<sup>14</sup>

## 1.2 0D Carbon Nanoallotropes

The unique ability of carbon atoms to participate in covalent bonds with other carbon atoms in diverse hybridization states ( $sp$ ,  $sp^2$ ,  $sp^3$ ) or with nonmetallic elements enables them to form a wide range of structures, from small molecules to long chains.<sup>16</sup> The most known 0D nanoallotropes of carbon include fullerenes and carbon dots as shown in Figure 1.3.

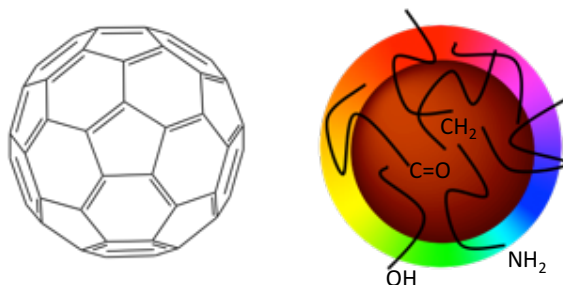


**Figure 1.3.** Schematic representation of a  $C_{60}$  structure (left) and an artist impression of a fluorescent carbon dot (right).

### **1.2.1 Fullerenes**

C<sub>60</sub>, also known as Buckminster fullerene, was the first carbon nanoallotrope discovered in 1985 by H. W. Kroto, R. F. Curl and R. E. Smalley (yielding in 1996 the Nobel Prize in Chemistry). Several other types of fullerenes were also discovered in the following, such as C<sub>20</sub> and C<sub>70</sub>. C<sub>60</sub> is the most widely studied fullerene up to date; each molecule consists of 60 sp<sup>2</sup> carbon atoms arranged in pentagons and hexagons to form a spherical nanostructure (cage).<sup>16</sup> Fullerenes are the smallest carbon nanostructures and can be regarded both as molecules and nanomaterials. Their size and electronic structure renders them very attractive for doping and functionalization, a precondition for the synthesis of novel fullerene-derivatives with unique properties for application in medical and electron-transport devices, such as sensors, transistors, or solar cells.<sup>16, 17</sup>

### **1.2.2 Carbon Dots**

Carbon dots (C-dots) are quasi-spherical carbon nanoparticles with diameters of 2-10 nm consisting of carbon, hydrogen and oxygen. C-dots are a new class of luminescent nanoparticles with properties matching the traditional metal-containing quantum dots.<sup>18</sup> The combination of multicolour and tunable emission, controlled surface chemistry, low toxicity and solvent dispersibility give C-dots great potential for a wide range of applications including light emitting diodes, solar cells, sensing, catalysis and photovoltaic devices as well as in the fields of bioimaging and nanomedicine.<sup>18, 19</sup> The most common synthetic methods for the fabrication of C-dots are the "top-down" and "bottom-up" approaches. The splitting up of larger carbon structures (graphite, carbon nanotubes and nanodiamonds) into C-dots is achieved by "top-down" synthetic methods such as arc discharge, laser ablation and electrochemical techniques.<sup>20</sup> In the other hand, "bottom-up" synthetic methods refer to the synthesis of C-dots from simple precursors such as carbohydrates, citrate and polymer-silica nanocomposites. Hydrothermal treatment and microwave-assisted methods are the most common synthetic routes.<sup>21</sup> Doping of C-dots with heteroatoms such as nitrogen and sulfur or metal ions (e.g., Zn, Gd, Si) is also common since it allows to tune the optical properties or to add new functionalities.<sup>18,</sup>

<sup>19, 22</sup>



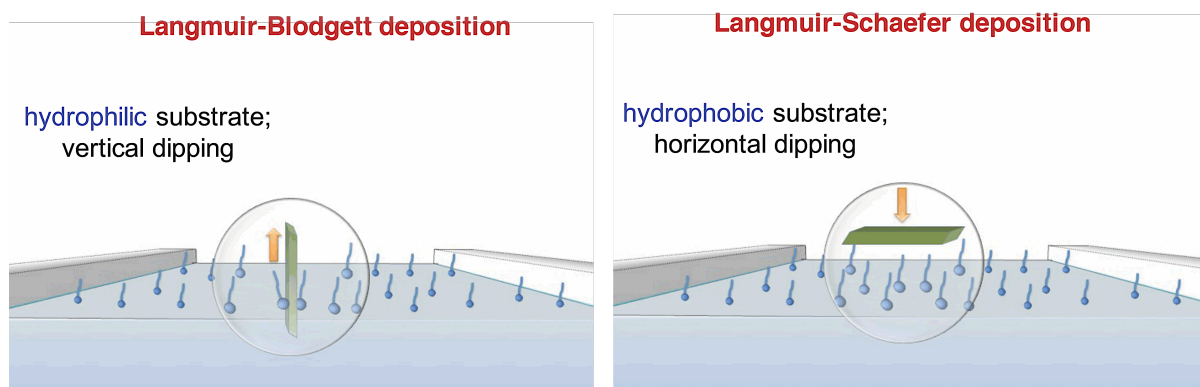


**Figure 1.4.** Schematic representation of the Langmuir-Blodgett (left) and Langmuir-Schaefer (right) deposition techniques.

### 1.3 Langmuir-Blodgett technique

The Langmuir-Blodgett (LB) technique is one of the most widely used layer-by-layer (LbL) deposition methods for preparing monolayer and multilayer thin films. Its invention was key to the Nobel Prize in Chemistry awarded to Langmuir in 1932 for his work in surface chemistry. The method consists in forming organic monolayers called Langmuir films, of amphiphilic molecules in the air-water interface and depositing them by immersing a solid substrate into the liquid (vertical dipping). If the substrate is instead horizontally dipped the method is called Langmuir-Schaefer (LS) deposition and the only difference with the LB technique is the geometry as shown in Figure 1.4. In both cases amphiphilic molecules are adsorbed homogeneously with accurate control of the thickness of the formed monolayers. This bottom-up approach enables the precise control over the packing density of the molecules but also allows the deposition over large areas.<sup>23</sup>

### 1.4 Outline of the thesis

The research work subject of this thesis is presented in five (5) chapters and two (2) appendixes.

In Chapter 2 the most recent developments in the use of the Langmuir-Blodgett technique for the design and preparation of novel graphene-based hybrids are presented in a comprehensive and critical overview. The structural, physicochemical,

electronic and mechanical properties of these hybrid systems are discussed and how these properties can be exploited applications in various fields is emphasized.

In Chapters 3 and 4 hybrid graphene-based multilayers and monolayers containing either pure Buckminster fullerene or a fullerenes derivative ( $C_{60}Br_{24}$  or  $C_{60}(OH)_{24}$ ) were developed by a modified Langmuir-Blodgett approach, which combines the Langmuir-Schaefer method with self-assembly. This approach uses graphene nanosheets as templates for the attachment of fullerenes in a bi-dimensional arrangement, allowing the control of layer-by-layer growth at the molecular level. The produced multilayer thin films constitute novel hybrid systems that could be used for potential applications in optoelectronics, photovoltaics, sensors, photocatalysis and drug delivery.

The combined properties of luminescent carbon dots and graphene in hybrids offer unique opportunities for highly efficient applications in the fields of optoelectronics, sensing, catalysis and biomedicine. Towards this aim, in Chapter 5, hydrophilic carbon nanodots were for first time inserted between graphene nanosheets by the same bottom-up approach, to form transparent hybrid multilayer nanostructures.

Finally, in Chapter 6, a new and facile approach for the synthesis of germanane is described, through which the final product can be obtained in significantly shorter time (few minutes) than reported so far. The antimicrobial activity of germanane was investigated for first time. Moreover a new technology for the preparation of antimicrobial thin films and coatings is presented. Nanoflakes of germanane produced by liquid exfoliation were injected in air-water interphase of the Langmuir-Blodgett trough without the use of organic molecules and compressed to obtain a Langmuir film of closed-packed GeH flakes. After transfer to a substrate, the antimicrobial activity of the germanane films was investigated for first time, revealing that the bacterial populations incubated on germanane films were importantly decreased. In addition the antimicrobial activity of GeH dispersions showed that during the first six hours bacterial growth is very strongly suppressed.

## 1.5 References

1. Violatti, C. Pottery in Antiquity. <http://www.ancient.eu/pottery/>
2. Pottery Timeline: Chronology of Ceramic Art Around the World. <http://www.visual-arts-cork.com/pottery-timeline.htm>
3. Kaul, A. B. *Journal of Materials Research* **2014**, 29, (03), 348-361.
4. Yang, G.; Zhu, C.; Du, D.; Zhu, J.; Lin, Y. *Nanoscale* **2015**, 7, (34), 14217-14231.
5. Nicolosi, V.; Chhowalla, M.; Kanatzidis, M. G.; Strano, M. S.; Coleman, J. N. *Science* **2013**, 340, (6139).
6. High-throughput prediction of novel two-dimensional materials. <http://adsabs.harvard.edu/abs/2016APS..MARL23002M>
7. Sun, Z.; Martinez, A.; Wang, F. *Nat Photon* **2016**, 10, (4), 227-238.
8. Spyrou, K.; Potsi, G.; Diamanti, E. K.; Ke, X.; Serestatidou, E.; Verginadis, I. I.; Velalopoulou, A. P.; Evangelou, A. M.; Deligiannakis, Y.; Van Tendeloo, G.; Gournis, D.; Rudolf, P. *Advanced Functional Materials* **2014**, 24, (37), 5841-5850.
9. Shao, Y.; Wang, J.; Wu, H.; Liu, J.; Aksay, I. A.; Lin, Y. *Electroanalysis* **2010**, 22, (10), 1027-1036.
10. Wang, Y.; Shi, Z.; Huang, Y.; Ma, Y.; Wang, C.; Chen, M.; Chen, Y. *The Journal of Physical Chemistry C* **2009**, 113, (30), 13103-13107.
11. Sofo, J. O.; Chaudhari, A. S.; Barber, G. D. *Physical Review B* **2007**, 75, (15), 153401.
12. Elias, D. C.; Nair, R. R.; Mohiuddin, T. M. G.; Morozov, S. V.; Blake, P.; Halsall, M. P.; Ferrari, A. C.; Boukhvalov, D. W.; Katsnelson, M. I.; Geim, A. K.; Novoselov, K. S. *Science* **2009**, 323, (5914), 610-613.
13. Zhou, C.; Chen, S.; Lou, J.; Wang, J.; Yang, Q.; Liu, C.; Huang, D.; Zhu, T. *Nanoscale Research Letters* **2014**, 9, (1), 26-26.
14. Walid, A.; Patrick, M. O.; Elizabeth, J. B.; Dante, J. O. H.; Yunqiu Kelly, L.; Jeremiah van, B.; Igor, P.; Yi, W.; Adam, S. A.; Jyoti, K.; Marc, W. B.; Harry, W. K. T.; Joshua, E. G.; Roland, K. K. *2D Materials* **2015**, 2, (3), 035012.
15. Liu, Z.; Lou, Z.; Li, Z.; Wang, G.; Wang, Z.; Liu, Y.; Huang, B.; Xia, S.; Qin, X.; Zhang, X.; Dai, Y. *Chemical Communications* **2014**, 50, (75), 11046-11048.

16. Georgakilas, V.; Perman, J. A.; Tucek, J.; Zboril, R. *Chemical Reviews* **2015**, 115, (11), 4744-4822.
17. Scharff, P., Fundamental Properties and Applications of Fullerene and Carbon Nanotube Systems. In *Frontiers of Multifunctional Nanosystems*, Springer Netherlands: Dordrecht, 2002; pp 213-224.
18. Bourlinos, A. B.; Karakassides, M. A.; Kouloumpis, A.; Gournis, D.; Bakandritsos, A.; Papagiannouli, I.; Aloukos, P.; Couris, S.; Hola, K.; Zboril, R.; Krysmann, M.; Giannelis, E. P. *Carbon* **2013**, 61, 640-643.
19. Bourlinos, A. B.; Bakandritsos, A.; Kouloumpis, A.; Gournis, D.; Krysmann, M.; Giannelis, E. P.; Polakova, K.; Safarova, K.; Hola, K.; Zboril, R. *Journal of Materials Chemistry* **2012**, 22, (44), 23327-23330.
20. Lim, S. Y.; Shen, W.; Gao, Z. *Chemical Society Reviews* **2015**, 44, (1), 362-381.
21. Peng, H.; Travas-Sejdic, J. *Chemistry of Materials* **2009**, 21, (23), 5563-5565.
22. Bourlinos, A. B.; Trivizas, G.; Karakassides, M. A.; Baikousi, M.; Kouloumpis, A.; Gournis, D.; Bakandritsos, A.; Hola, K.; Kozak, O.; Zboril, R.; Papagiannouli, I.; Aloukos, P.; Couris, S. *Carbon* **2015**, 83, 173-179.
23. Peterson, I. R. *Journal of Physics D: Applied Physics* **1990**, 23, (4), 379.

# Appendix A

## Characterization techniques

### A.1 FTIR spectroscopy

Infrared spectra reported in Chapters 4, 5 and 6 were measured with a SHIMADZU 8400 infrared spectrometer, in the region of 400-4000  $\text{cm}^{-1}$ , equipped with a deuterated triglycine sulphate (DTGS) detector. Each spectrum was the average of 200 scans collected at 2  $\text{cm}^{-1}$  resolution by means a SPECAC variable-angle attachment. Samples were in the form of KBr pellets containing *ca.* 2 wt % of the sample.

### A.2 Raman spectroscopy

Raman spectra of thin films deposited on Si-wafer and of powder samples of C-dots, reported in Chapters 3, 4 and 5 were collected with a Micro-Raman system RM 1000 RENISHAW using a laser excitation line at 532 nm (laser diode). A 0.5-1 mW laser power was used with a 1  $\mu\text{m}$  focus spot in order to avoid photodecomposition of the films. Powder samples of fullerene derivatives ( $\text{C}_{60}(\text{OH})_{24}$  and  $\text{C}_{60}\text{Br}_{24}$ ) and GeH, reported in Chapter 4 and 6 respectively, were measured using a Labram Horiba HR spectrometer integrated with a laser line at 514 nm. A 1.5 mW laser power was used with a 2  $\mu\text{m}$  focus spot. The measurements were performed by Dr. Konstantinos Dimos (University of Ioannina, Greece) and Dr. Vasilios Kostas (University of Ioannina, Greece).

### A.3 X-ray photoelectron spectroscopy

X-ray photoelectron spectroscopy (XPS) measurements of thin films and of aqueous dispersion of GO deposited on Si-wafer reported in Chapters 3 and 5 were performed in ultrahigh vacuum at a base pressure of  $2 \times 10^{-10}$  mbar with a SPECS GmbH spectrometer equipped with a monochromatic Mg K $\alpha$  source ( $h\nu=1253.6$  eV) and a Phoibos-100 hemispherical analyzer. The spectra were collected in normal emission and energy resolution was set to 1.16 eV to minimize measuring time. The

measurements were performed by Dr. Konstantinos Dimos (University of Ioannina, Greece) and Dr. Konstantinos Spyrou (University of Ioannina, Greece).

X-ray photoelectron spectroscopy (XPS) data of the hybrid films deposited on Si-wafer, reported in Chapter 4 were collected at a base pressure of  $5 \times 10^{-10}$  mbar in a SPECS GmbH spectrometer equipped with a monochromatic Mg  $K_{\alpha}$  source ( $h\nu=1253.6$  eV) and a Phoibos-100 hemispherical analyser. The energy resolution was set to 1.16 eV and the photoelectron take-off angle was  $37^{\circ}$  with respect to the surface normal. All binding energies were referenced to the C1s core level photoemission line at 284.6 eV. Spectral analysis included a Shirley background subtraction and a peak deconvolution employing mixed Gaussian-Lorentzian functions,<sup>1</sup> in a least squares curve-fitting program (WinSpec) developed at the Laboratoire Interdisciplinaire de Spectroscopie Electronique, University of Namur, Belgium. The measurements were performed by Dr. Georgia Potsi (University of Groningen, The Netherlands).

#### **A.4 X-ray diffraction**

The X-ray diffraction (XRD) patterns of thin films deposited on Si-wafer substrates reported in Chapters 3, 4 and 5 and of powder samples of C-dots reported in Chapter 5, (Appendix B) were collected on a D8 Advance Bruker diffractometer by using a Cu  $K_{\alpha}$  ( $\lambda=1.5418 \text{ \AA}$ ) radiation source (40 kV, 40 mA) and a secondary beam graphite monochromator. The patterns were recorded in the 2-theta ( $2\theta$ ) range from 2 to  $80^{\circ}$ , in steps of  $0.02^{\circ}$  and with a counting time of 2 s per step.

#### **A.5 Thermal analysis**

The thermogravimetric (TGA) and differential thermal (DTA) analyses reported in Chapter 4 were performed using a Perkin Elmer Pyris Diamond TG/DTA. Powder samples of approximately 5 mg were heated in air from  $25^{\circ}\text{C}$  to  $850^{\circ}\text{C}$ , at a rate of  $5^{\circ}\text{C}/\text{min}$ .

## **A.6 UV-Vis spectroscopy**

The UV-Vis spectra reported in Chapter 5 were collected on a Shimadzu UV-2401PC two beam spectrophotometer in the range of 200-800 nm, at a step of 0.5 nm, using combination of deuterium and halogen lamps as sources. UV-Vis spectra were recorded at room temperature either from thin film deposited on quartz substrates or using 10 mm path-length quartz cuvettes in the case of dispersions.

The diffuse reflectance measurements of powder samples reported in Chapter 6, were performed using a Shimadzu UV-VIS-NIR Spectrophotometer (UV-3600) equipped with an integrating sphere attachment on barium sulfate coatings. The measurements were performed by Dr. Georgia Potsi (University of Groningen, The Netherlands).

## **A.7 Photoluminescence spectroscopy**

The photoluminescence spectra reported in Chapter 5 were recorded on a Jobin Yvon Fluorolog 3 spectrofluorometer FL-11 employing xenon 450 W lamp and a P928P photodetector. The slits were set at 5 nm. The photoluminescence spectra were corrected through the instrument-supplied files, created from compounds with known quantum yields and an included Si photodetector. The detector-source geometry was at 90° with respect to the sample and for the film photoluminescence measurements the quartz substrate was set in a reflective geometry. PL spectra were collected at room temperature either from thin films deposited on quartz substrates or using 10 mm path-length quartz cuvettes in the case of suspensions. The measurements were performed by Dr. Konstantinos Dimos (University of Ioannina, Greece) and Prof. Ioannis Koutselas (University of Patras, Greece).

## **A.8 Nuclear magnetic resonance**

<sup>1</sup>H Magic Angle Spinning (MAS) NMR experiments in powder samples reported in Chapter 6, were conducted on a BRUKER AVANCE NMR spectrometer, operating at 400 MHz (9.4 Tesla) at room temperature, by using 4 mm zirconia rotors. The MAS frequency was set to 12 kHz and one-dimensional <sup>1</sup>H NMR spectra were acquired with 16 scans. <sup>1</sup>H chemical shifts were referenced to adamantane and NMR data

were further processed using TopSpin 3.1. The measurements were performed by Dr. Georgios Papavassiliou (NCSR Demokritos, Greece).

### **A.9 Contact angle measurements**

The water contact angle (CA) measurements of thin films deposited on Si-wafer substrates reported in Chapter 4, were performed on a SL200 KS contact angle meter from Kino at ambient atmospheric conditions. 5  $\mu$ L distilled water droplets were used for all CA measurements. CA was recorded from the time the droplet touched the surface of the film (CA  $t=0$ ) until CA reached a plateau value, approximately 1 min after the first touch (CA  $t=1$  min). After this first static measurement and at the same point, dynamic WCA measurements were performed. Advancing and receding WCA were measured on a water droplet of decreasing/increasing volume.<sup>2</sup> The measurements were performed by Dr. Nikolaos Vourdas (Technological Educational Institute of Sterea Ellada, Greece).

### **A.10 Scanning electron microscopy**

Scanning electron microscopy (SEM) images of thin films deposited into Si-wafer substrates and of ethanol dispersion of GeH deposited by drop-casting into Si-wafers reported in Chapter 3 and Chapter 6 respectively, were recorded using a JEOL SEM-6510LV scanning electron microscope equipped with an EDX analysis system xx-Act from Oxford Instruments. The measurements were performed by Dr. Konstantinos Dimos (University of Ioannina, Greece).

### **A.11 Electrical conductivity measurements**

For the electrical conductivity reported in Chapter 3, four-probe measurements on thin films deposited on Si-wafer substrates, were performed using an AFX DC 9660SB power supply and a Keithley 2000 multimeter. The measurements were performed by Prof. Vassilleios Georgakilas (University of Patras, Greece).



### **A.12 Atomic force microscopy**

The topographic atomic force microscopy (AFM) images reported in Chapters 3, 4, 5 and 6 were recorded in tapping mode with a Bruker Multimode 3D Nanoscope, using a silicon microfabricated cantilever type TAP-300G, with a tip radius <10 nm and a force constant range of  $\sim 20-75 \text{ N m}^{-1}$ . Monolayer and multilayer thin films were deposited on Si-wafer substrates, while C-dots (Chapter 5) and germanane (Chapter 6) were deposited into Si-wafers by drop-casting from aqueous and ethanol dispersions respectively.

### **A.13 References of Appendix A**

1. Shirley, D. A. *Physical Review B* **1972**, 5, (12), 4709-&.
2. Vourdas, N.; Pashos, G.; Kokkoris, G.; Boudouvis, A. G.; Stathopoulos, V. N. *Langmuir* **2016**, 32, (21), 5250-5258.



## Chapter 2

# Graphene-based hybrids through the Langmuir-Blodgett approach

Layer-by-layer assembly is an easy and inexpensive technique for the development of multilayer films. Nevertheless, simplicity and low cost are not the only reasons why layer-by-layer deposition has attracted so much of attention over the past two decades. The versatility of the process, the capability of using diverse types of materials, the tailoring of the final nanostructures with controlled architecture, thickness and functionality and lastly the potential of tuned, well defined and desired properties determined by the number of layers in the films are briefly the main advantages of layer-by-layer methods. Consequently, layer-by-layer assembly is considered to be an important bottom-up nanofabrication technique today which has very few limitations. The Langmuir-Blodgett technique is one of the most promising layer-by-layer methods for preparing monolayer and multilayer of graphene-based thin films. This bottom-up approach enables the precise control of the single layer thickness and allows homogeneous deposition over large areas on almost any kind of solid substrate. Although this emerging field of graphene nanoscience remains largely unexplored, several studies have demonstrated either the successful preparation of high-quality graphene monolayer films or of multilayer films of novel graphene hybrids created by integrating a variety of guest species with the graphene matrix.

---

This chapter is based on the book chapter: "Layer-by-Layer assembly of graphene-based hybrid materials", by A. Kouloumpis, P. Zygouri, K. Dimos and D. Gournis, which appeared on pp. 359-399 of "Functionalization of Graphene", 1<sup>st</sup> ed., edited by Vasilios Georgakilas, 2014, Wiley-VCH GmbH & Co. KGaA, Weinheim, Germany).

## **2.1 Introduction**

Graphene, being a single-layered material is an amazing and promising candidate for layer-by-layer (LbL) assembly. Its superior electronic and mechanical properties can be modified, tuned, or enhanced by LbL assembly as many studies have reported over the last 3-4 years. The resulting LbL graphene-based hybrid films commonly attain varied and complex properties as various substances can be used for the intermediate layer and may become elements of electronic circuits, supercapacitors, sensors *etc.*

Thin films of a thickness of a few nanometers (composed of single layer graphene) are the source of high expectations as useful components in many practical and commercial applications. The possibility to synthesize hybrid materials, almost without limitations, with desired structure and functionality in conjunction with a sophisticated thin film deposition technology enables the production of electrically, optically and biologically active components on the nanometer scale. The Langmuir-Blodgett (LB) technique is one of the most promising techniques for preparing such thin films as it enables:

- the precise control of the monolayer thickness,
- homogeneous deposition of the monolayer over large areas and
- the possibility to make multilayer structures with varying layer composition. An additional advantage of the LB technique is that monolayers can be deposited on almost any kind of solid substrate.

Many possible applications (optical, electrical and biological) have been suggested over the years for Langmuir Blodgett films.<sup>1</sup> Next to other layered materials, like aluminosilicate nanoclays or layered double hydroxides, graphene has been widely used in the LB approach. High quality graphene monolayers have been placed on surfaces where direct graphene growth is not possible or multilayer films of novel graphene hybrids have been developed by integrating graphene matrices with a variety of guest species.

## 2.2 Monolayers of Graphene Oxide

With the Langmuir-Blodgett technique, water supported single layers of graphene oxide (GO) can be compressed and transferred without any surfactant or stabilizing agent as demonstrated by Laura Cote *et al.*<sup>2</sup> in 2008. The single layers formed a dispersion, which was stable against flocculation or coagulation when confined in 2D at the air-water interface. The edge-to-edge repulsion between the single layers prevented them from overlapping during compression. The layers folded and wrinkled at their interacting edges at high surface pressure, leaving the interior flat. GO single layer Langmuir films can be readily transferred to a solid substrate and their density is continuously tunable from dilute, to close packed and to over packed monolayers of interlocking sheets. When single layers of very different sizes are brought together face to face, they can irreversibly stack to form double layers.<sup>2</sup> The geometry-dependent GO single layer interaction revealed here should provide insight into the thin film processing of GO materials since the packing of GO single layers affects surface roughness, film porosity, packing density, *etc.* In addition, LB assembly readily creates large-area films of single layer GO, which is a starting material for graphene-based electronic applications.<sup>2</sup>

The insight that graphene oxide has hydrophilic functional groups and parts of the basal plane that are hydrophobic, should lead to a better understanding of the processing and assembly of GO sheets. GO can be solution processed to form thin films by many techniques such as spin coating, drop casting, spraying and dip coating, *etc.* Laura Cote *et al.*<sup>3</sup> also deposited GO on various surfaces by means of the classical Langmuir-Blodgett technique, where a surfactant is spread on the water surface and confined between two movable barriers (Figure 2.1a). As the barriers are closed, the surface density of molecules increases, leading to an increase in surface pressure, or reduction in surface tension that can be continuously monitored by a tensiometer. The floating Langmuir films can then be transferred to a solid support by vertical dip-coating. GO can be spread from alcohols that are even miscible with water, such as methanol. When methanol droplets are gently dropped on water surface, they can first spread rapidly on the surface before mixing with water.

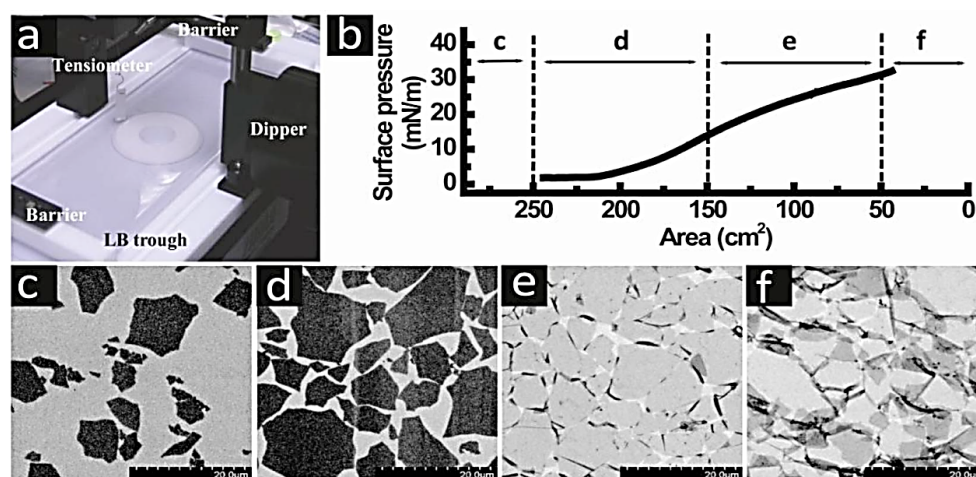


**Figure 2.1.** LB assembly of GO sheets. (a) With an LB trough, the surface density of GO sheets can be continuously manipulated by the barriers and the surface pressure can be monitored by the tensiometer. Monolayers can be transferred to a solid substrate by dip-coating. (b) Surface pressure-area isotherm of a GO Langmuir film showing a continuously increasing surface pressure with decreasing area. (c–f) SEM images of monolayers transferred at surface pressures in the corresponding regions in the isotherm plot, showing continuously tunable surface coverage from (c) isolated flat sheets, (d) close-packed sheets, (e) overpacked sheets with folded edges to (f) overpacked sheets interlocked with each other. (Reproduced with permission from <sup>3</sup>)

In this way, the GO surfactant sheets can be effectively trapped at the air–water interface<sup>3</sup> and their density in the Langmuir film continuously tuned by moving the barriers. Upon compression, the Langmuir film exhibits a gradual increase in surface pressure, as shown in the surface-pressure–area isotherm plot (Figure 2.1b). If the film is transferred at the initial stage where the surface pressure is near zero, it consists of dilute, well-isolated flat sheets (Figure 2.1c). As compression continues and the surface pressure increases, the sheets start to close pack into a broken tile mosaic pattern over the entire surface (Figure 2.1d). Upon further compression, the soft sheets are forced to fold and wrinkle at their touching points in order to accommodate the increased pressure (Figure 2.1e). This is in stark contrast to traditional molecular or colloidal monolayers, which would collapse into double layers giving rise to a constant or decreasing surface pressure when compressed beyond the close-packed regime. Even further compression results in interlocked sheets with

nearly complete surface coverage (Figure 2.1f).<sup>3</sup> The LB assembly produces flat GO thin films with uniform and continuously tunable coverage.

The Langmuir–Blodgett technique was used by Xi Ling and Jin Zhang<sup>4</sup> in the same year, to build up ordered mono- and multilayer assemblies of protoporphyrin IX (PPP) on top and on bottom sides of graphene as shown in Figure 2.2. The Raman enhancement was dependent on the molecular configuration in contact with graphene; the functional group of PPP in direct contact with graphene caused a stronger enhancement than other groups.<sup>4</sup> These results reveal that graphene-enhanced Raman scattering (GERS) is strongly dependent on the distance between graphene and the molecule, which is convincing evidence that the Raman enhancement based on graphene is due to a chemically enhanced mechanism. This discovery provides a convenient system for the study of the chemical-enhanced mechanism and will benefit further understanding of surface-enhanced Raman scattering (SERS).

Tamás Szabo *et al.*<sup>5</sup> observed a negligible amount of imperfections in LB films of GO sheets deposited in a hydrophilic substrate: folded back at interconnecting edges or face-to-face aggregates were extremely scarce. These highly ordered single layers are very promising for advanced electronic applications because very large areas can be covered by densely tiled graphene oxide nanosheets, which can provide continuous electrical pathways after reduction to increase their conductivity.<sup>5</sup> LB films of chemically reduced graphene oxide may be especially beneficial for the fabrication of optically transparent flexible circuits, where the use of indium tin oxide (ITO) is limited due to its rigidity and fragility.

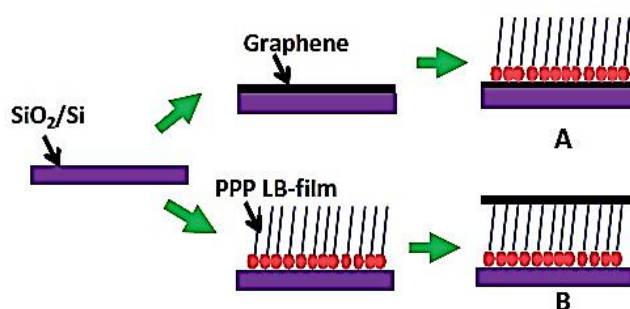


**Figure 2.2.** Schematic representation of the preparation of protoporphyrin IX (PPP) and graphene. (Reproduced with permission from <sup>4</sup>)

Xiluan Wang, Hua Bai and Gaoquan Shi<sup>6</sup> in 2011 developed a universal technique for size fractionation of GO sheets by just adjusting the pH value of GO dispersion. The hydrazine reduced Langmuir-Blodgett films of GO flakes with large lateral dimensions showed much higher conductivities than those of GO flakes with small lateral dimensions. Furthermore, the thin film of large GO flakes prepared by filtration exhibited a smaller d-spacing as well as much higher tensile strength and modulus than those of films built up from small flakes. The LB films of larger GO sheets also showed higher conductivities after chemical reduction because of their more compact morphology, fewer structural defects and lower contact resistances.<sup>6</sup> The lateral dimensions of GO sheets also have a strong effect on the structure and properties of the self-assembled GO films: larger GO sheets favor the formation of paper-like films with more tight and perfect structures, which greatly improved their mechanical properties.

A year later Luna Imperiali *et al.*<sup>7</sup> investigated the structure and properties of the graphene oxide interfacial layer and evaluated the conditions for the formation of freestanding films. The rheological properties were shown to be responsible for the efficiency of such layers in stabilizing water-oil emulsions. Moreover, because of the mechanical integrity, large-area monolayers deposited by the Langmuir-Blodgett technique can be turned into transparent conductive films upon subsequent chemical reduction.

Régis Y. N. Gengler and co-workers<sup>8</sup> developed a straight forward method to deposit uniform single-layer graphene films on arbitrary substrates without size limitation and under ambient conditions. The fast high-yield method allowed control of graphene coverage by simple adjustment of the applied surface pressure in a LB trough. The prepared films could sustain all physical and chemical treatments associated with the lithography process without any loss of material. Additionally, among all chemically exfoliated graphite, the flakes obtained show one of the lowest resistivities at the Dirac charge neutrality point ( $\approx 65$  kV) and gave evidence for switching from a hole-conduction regime to an electron-conduction regime.

In 2012 spectroscopic studies of large sheets of graphene oxide and reduced graphene oxide monolayers prepared by the Langmuir-Blodgett technique were reported by D. S. Sutar *et al.*<sup>9</sup> Moreover, photoelectron spectroscopy was used to



investigate the electronic structure of the monolayers.<sup>10</sup> The GO monolayers obtained by Langmuir-Blodgett route and suitably treated to obtain rGO monolayers. In comparison with GO, rGO monolayers showed steeper Fermi edge, decrease in work function (WF) and increase in p electron density of states (DOS) due to removal of oxygen functional groups or increase in graphitic carbon species. The rGO as compared to GO, also exhibited Auger features attributable to the increase in p electron DOS. The effective number of valence electrons as obtained from plasmon loss features showed 28% increase upon reduction, associated with the increase in graphitic carbon content. Thus, by controlled reduction of GO, it should be possible to tune its electronic structure and hence electronic/optoelectronic properties.

## 2.3 Nanocomposite films

A Langmuir-Blodgett approach for the highly-efficient fabrication of nanoscrolls was reported by Yan Gao *et al.*<sup>11</sup> The scrolls consisting of rolled up functionalized graphene oxide single sheets have a tubular structure without caps at their ends as revealed by transmission electron microscope. The scrolls align parallel to the moving barriers of the LB equipment and exhibit a loose-dense pattern during the LB compression process. The authors also realized that specific solvents could unwind the scroll structures.

Transparent conductive films were produced by Qing-bin Zheng *et al.*<sup>12</sup> in 2011 using the ultra-large graphene oxide sheets that were deposited layer-by-layer on a substrate using the Langmuir-Blodgett (LB) assembly technique. The density and degree of wrinkling of the ultra large GO monolayers are turned from dilute, close-packed flat GO to graphene oxide wrinkles and concentrated graphene oxide wrinkles by varying the LB processing conditions.<sup>12</sup> The method opens the way for high-yield fabrication of GO wrinkles or concentrated GO wrinkles that are considered promising materials for hydrogen storage, supercapacitors and nanomechanical devices. The films produced from ultra large GO sheets with a close-packed, flat structure exhibit exceptionally high electrical conductivity and transparency after thermal reduction and chemical doping treatments. A remarkable sheet resistance of  $\sim 500 \Omega/\text{sq}$  at 90% transparency were obtained, which

outperformed the graphene films grown on a Ni substrate by chemical vapour deposition.<sup>12</sup> In another similar work of Zheng Qing-bin and co-workers<sup>13</sup> a sheet resistance of 605  $\Omega/\text{sq}$  at 86% transparency was obtained. This technique for the production of transparent conductive thin films of ultra large GO flakes is not only facile and inexpensive; it can also be upscaled for mass production.

A year later, Ganganahalli K. Ramesha *et al.*<sup>14</sup> demonstrated the possibility of 2-D *in-situ* electrochemical polymerization in a Langmuir trough. They spread exfoliated graphene oxide on the water surface to bring anilinium cations present in the subphase to air–water interface through electrostatic interactions (Figure 2.3). Subsequent electrochemical polymerization of aniline under applied surface pressure results in a GO/polyaniline composite with polyaniline in planar polaronic form. For the deposition in a glassy carbon substrate the Langmuir-Schaefer mode (horizontal dipping of the substrate) was applied.

The same year Pavan Narayanam and his co-workers<sup>15</sup> prepared a GO-Cd composite Langmuir-Blodgett film by introducing  $\text{Cd}^{2+}$  ions into the subphase. The changes in the behaviour of the Langmuir film isotherm in the presence of  $\text{Cd}^{2+}$  ions are attributed to changes in the microstructure and density of the GO sheets on the subphase surface.

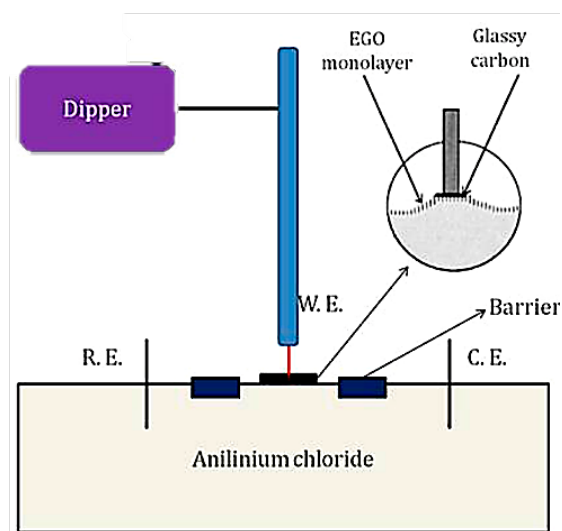


**Figure 2.3.** Experimental LB setup for *in-situ* polymerization. (Reproduced with permission from <sup>14</sup>)

The attachment of Cd ions onto the GO single layers causes some overlapping of the sheets and extensive formation of wrinkles. Sulphidation of the GO-Cd sheets results in the formation of uniformly distributed CdS nanocrystallites on the entire basal plane of the GO flakes.<sup>15</sup> The de-bonding of Cd with oxygen functional groups reduces the number of wrinkles. The GO sheets act primarily as a platform for the interaction of metal ions with oxygen functionalities and their structure and characteristic features are not affected by either the uptake of Cd or the formation of CdS.

## 2.4 Applications and properties of LB thin films

Xiaolin Li and his co-workers<sup>16</sup> in 2008 reported that the exfoliation-reintercalation-expansion of graphite can produce high quality single-layer graphene sheets stably suspended in organic solvents. The graphene sheets exhibit high electrical conductance at room and cryogenic temperatures. Moreover the Langmuir-Blodgett technique can assemble graphene sheets into large transparent conducting films in a layer-by-layer manner. The chemically derived, high-quality graphene sheets could lead to future scalable graphene devices.

Yang Cao and his co-workers<sup>17</sup> in 2010, present a new class of high performance photoresponsive molecular field-effect transistors prepared from Langmuir-Blodgett films of copper phthalocyanine (CuPc) monolayer, where two-dimensional (2D) ballistically-conductive single-layer graphene is employed as planar contacts (Figure 2.4). The unique feature is the integration of the LB technique with the fabrication of nanogap electrodes to build functional molecular electronic devices. The integration of the LB technique with sophisticated micro/nanofabrication affords efficient molecular field-effect transistors with bulk-like carrier mobility (as high as  $0.04 \text{ cm}^2 \text{ V}^{-1} \text{ s}^{-1}$ ), high on/off current ratios (over  $10^6$ ), high yields (almost 100%) and high reproducibility. Another important result is that these transistors are ultrasensitive to light, although their active channel consists of a single, only 1.3 nm-thick layer; such devices could form the basis for new types of environmental sensors and tunable photodetectors.

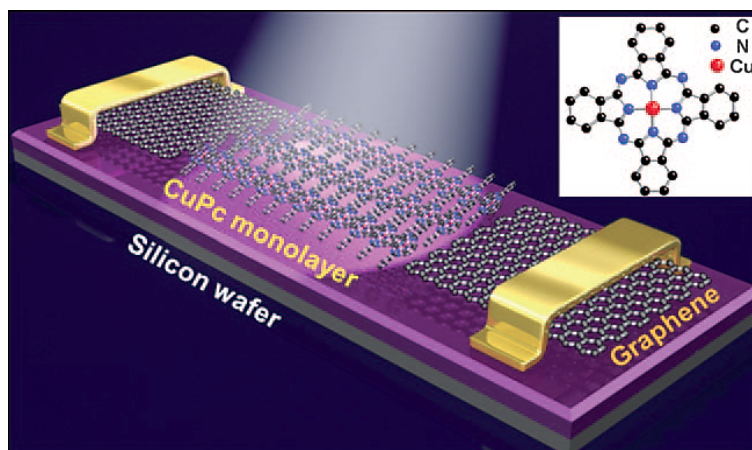


**Figure 2.4.** The structure of the CuPc monolayer transistor device with metal electrodes protected by a 50 nm layer of silicon dioxide. Inset: the molecular structure of copper phthalocyanine (CuPc). (Reproduced with permission from <sup>17</sup>)

This method of incorporating molecular functionalities into molecular electronic devices by combining bottom-up assembly and top-down device fabrication should speed the development of nanometer/molecular electronics in the future.

Negatively charged functionalized graphene oxide layers were incorporated into polyelectrolyte multilayers (PEMs) fabricated *via* Langmuir Blodgett deposition by Dhaval Kulkarni *et al.*<sup>18</sup> (Figure 2.5) in the same year. These LbL-LB graphene oxide nanocomposite films were released as robust freely standing membranes with large lateral dimensions (centimeters) and a thickness of around 50 nm.

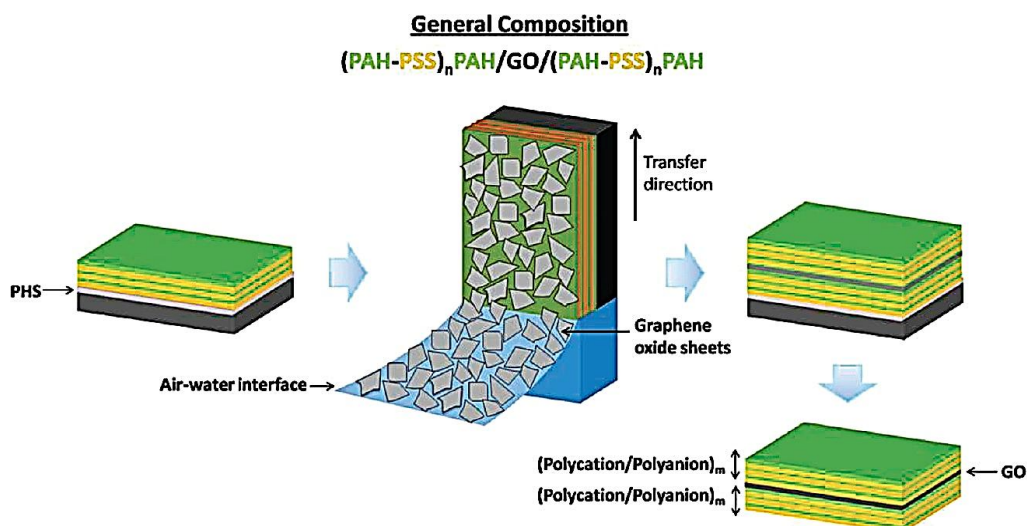


**Figure 2.5.** Schematic representation of fabrication and assembly of free-standing GO-LbL membrane. (Reproduced with permission from <sup>18</sup>)

Micromechanical measurements showed an elastic modulus enhancement by an order of magnitude, from 1.5 GPa for pure LbL membranes to about 20 GPa for membranes with only 8.0 vol % encapsulated graphene oxide.

A few-layer reduced graphene oxide (rGO) thin film on a Si/SiO<sub>2</sub> wafer using the Langmuir-Blodgett method, followed by thermal reduction, was fabricated by Zongyou Yin *et al.*<sup>19</sup> in 2012 (Figure 2.6). After photochemical reduction of Pt nanoparticles (PtNPs) on rGO, the obtained PtNPs/rGO composite was employed as the conductive channel in a solution-gated field effect transistor (FET), which was then used for real-time detection of hybridization of single-stranded DNA (ssDNA) with high sensitivity (2.4 nM). Such a simple, but effective method for fabrication of rGO-based transistors shows great potential for mass-production of graphene-based electronic biosensors.

A study on composite electrode materials based on GO and transition metal oxide nanostructures for supercapacitor applications was presented by John Lake *et al.*<sup>20</sup>. Electrophoretic deposition of GO on a conductive substrate was used to form reduced graphene oxide (rGO) films through chemical reduction. The strong interaction of GO with Co<sub>3</sub>O<sub>4</sub> and MnO<sub>2</sub> nanostructures was demonstrated in the self-assembled Langmuir–Blodgett monolayer composite, showing the potential to fabricate thin film supercapacitor electrodes without using binder materials.

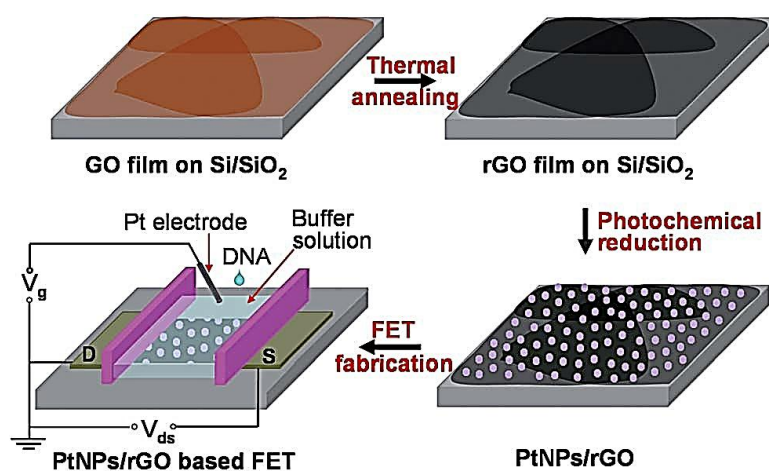


**Figure 2.6.** Schematic illustration of fabrication of a solution-gated FET device for DNA detection, based on LB films which combine Pt nanoparticles and reduced GO.

(Reproduced with permission from <sup>19</sup>)

They demonstrated a facile, two-step process of metal oxide and graphene nanocomposite to fabricate binder-free supercapacitor electrodes.<sup>20</sup> The initial hybrid electrode comprising a  $\text{Co}_3\text{O}_4$  and  $\text{MnO}_2$  nanocomposite with a top rGO layer provides more efficient contact of electrolyte ions, electroactive sites and shorter transport and diffusion path lengths, leading to higher specific capacitances than those of traditional double layer supercapacitors.<sup>20</sup> Particular advantages of this two-step composite nanostructure thin film process are that it is nontoxic and scalable for binder-free supercapacitor processing.

A compressed Langmuir film of GO flakes deposited on top of a fragile organic Langmuir-Blodgett film of  $\text{C}_{22}$  fatty acid cadmium salts (cadmium (II) behenate) can serve as an efficient protection as demonstrated by Søren Petersen *et al.*<sup>21</sup> The structure of the GO-protected LB film was found to be perfectly preserved. While metal deposition completely destroys the first two LB layers of unprotected films, the protected film showed to act as atomically thin barrier toward metal penetration and totally preventing the structural reorganization.

Continuing their research Qing-bin Zheng *et al.*<sup>22</sup> assembled large-area hybrid transparent films of ultra large graphene oxide and functionalized single walled carbon nanotubes *via* a layer-by-layer LB deposition (Figure 2.7).

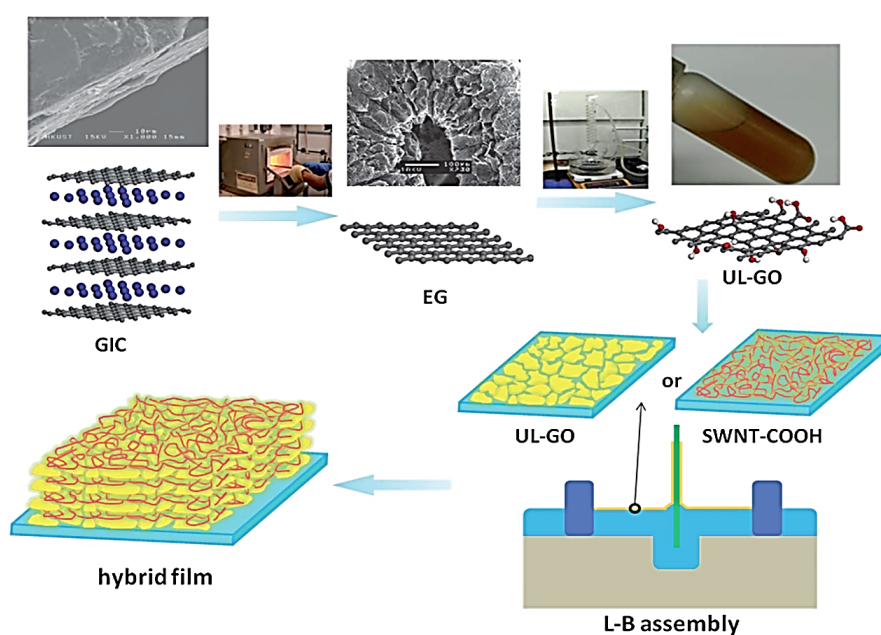


**Figure 2.7.** Flow chart for the synthesis of hybrid films of ultra large GO flakes and single walled carbon nanotubes. (Reproduced with permission from <sup>22</sup>)

The optoelectrical properties are much better than the corresponding of GO films prepared by the same technique and the highest among all graphene, GO and/or carbon nanotube thin films reported in the literature. The LB assembly technique, which, was developed, is capable of controlling the film composition, structure and thickness, while is highly suitable for fabrication of transparent conducting optoelectronic devices on a large scale without extra post-transfer processes. With further refinement of the synthesis technique, this versatile material could offer the properties required for next generation optoelectronic devices.

A novel simple and relatively cheap method for the fabrication of graphene flakes based on the intercalation of graphite with a KCl–NaCl–ZnCl<sub>2</sub> eutectic liquid was introduced by Kwang Hyun Park *et al.*<sup>23</sup> The authors confirmed that the alkali metal (potassium) was successfully inserted between graphite layers is at the optimized operation condition and showed that exfoliation also occurs in the process. The resulting graphene flakes preserve the unique properties of graphene and could be stably dispersed (>6 months) in pyridine solution without additional functionalization and surfactant stabilization. Transparent conducting graphene films from well-dispersed graphene flakes with high yield (~60%) were produced by a modified Langmuir-Blodgett assembly.<sup>23</sup> The resulting graphene film exhibited a sheet resistance of ~930 Ω/sq at a transparency of ~75% and a high conductivity (~91.000 Sm<sup>-1</sup>). The overall results suggest that the eutectic-based method to graphene production is a scalable and low-cost route that brings graphene-based electronics and composite fields closer to practical applications.

Other applications of graphene-based films were reported by Sohyeon Seo *et al.*<sup>24</sup> The authors fabricated a p-n diode junction of p-type rGO/n-doping Si substrate. Electric field-induced reduction of graphene oxide was performed by conductive atomic force microscopy in order to create a reduced GO p-n nanopatterned diode in a dry and non-destructive process directly on the surface where single GO sheets were deposited by the LB method. The authors chose n- and p-doped Si substrates that control charge transfer at the rGO interface (Figure 2.8).

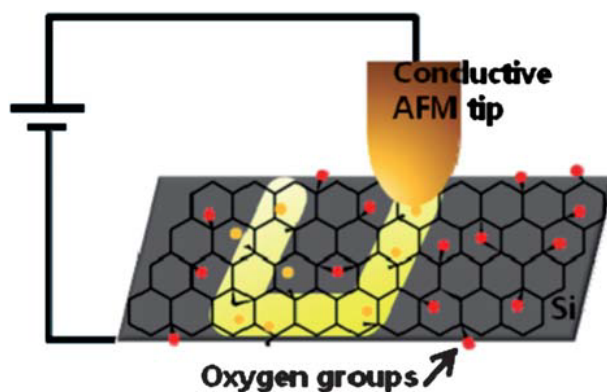


**Figure 2.8.** Electric field induced reduction to nanopattern the formation of rGO p-n diode junctions. (Reproduced with permission from <sup>24</sup>)

Electric field induced nanolithography resulted in locally reduced GO nanopatterns on GO sheets corresponding to the application of a negative bias voltage on an n-doping Si substrate. Electric field induced nanolithography was performed as a function of applied voltage and the rGO nanopatterned when -10.0 V were applied to the substrate showed high conductivity, comparable with that of the chemically reduced GO.<sup>24</sup> In addition, transport of rGO sheets, which were efficiently reduced under a local electric field, showed a uniform conductivity at sheet edges and the basal plane. Current-voltage (I-V) characteristics of rGO on n- and p-doping Si substrates indicated that electric field induced reduction nanolithography produced p-type rGO nanopatterns on the Si substrates. This junction is an indispensable electronic component that rectifies charge transport and prevents interference between neighboring electronic components in high density integrated crossbar devices.

Hai Li and his co-workers<sup>25</sup> used graphene oxide as a novel substrate for dip-pen nanolithography. After GO was transferred onto a SiO<sub>2</sub> substrate using the Langmuir-Blodgett technique, CoCl<sub>2</sub> was patterned on both GO and exposed SiO<sub>2</sub> substrates simultaneously by dip-pen nanolithography and then used for the growth of differently structured carbon nanotubes as presented in Figure 2.9. This novel graphene oxide/CNT composite might have potential applications in sensing, solar cells, electrode materials, *etc.*



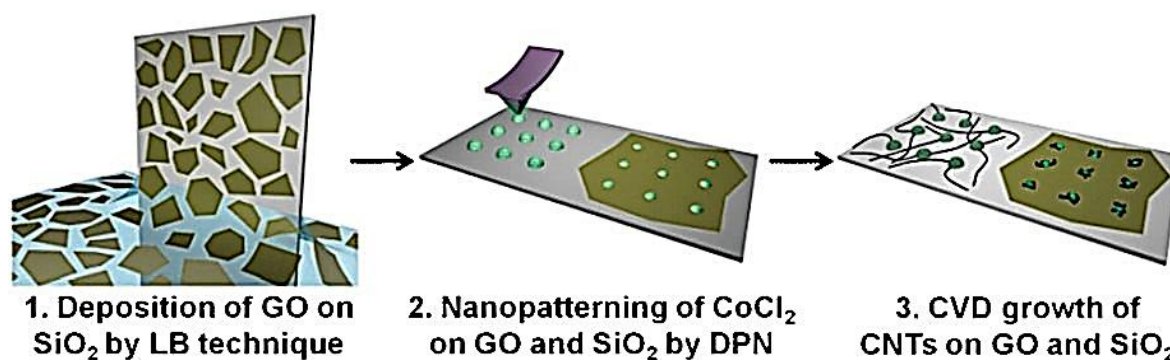


**Figure 2.9.** Schematic illustration of the experimental procedure. (1) Single layer GO sheets were transferred onto SiO<sub>2</sub> by using the LB technique. (2) CoCl<sub>2</sub> was simultaneously patterned on GO and SiO<sub>2</sub> by dip-pen nanolithography. (3) CNTs were grown on the patterned catalyst dots on GO and SiO<sub>2</sub> after CVD. (Reproduced with permission from <sup>25</sup>)

## 2.5 Conclusions

The Langmuir Blodgett technique is one of the most promising LbL processes as it enables the precise control of the monolayer thickness while allowing for homogeneous deposition over large areas and on almost any kind of solid substrate. On the other hand, graphene being a 2D single-layered material exhibits great optoelectronic and mechanical properties, which could be further tailored or enhanced with LbL assembling. In this direction, numerous studies have been reported during the past years concerning the modification of graphene sheets by LbL assembly to produce hybrid films. Owing to their exceptional properties, these multilayered systems are employed in a variety of different application areas from electronics to (bio)sensors. Despite these achievements there are still many challenges in designing and fabricating even better and higher quality graphene-based hybrid films.

## 2.6 References

1. KSV instruments, L., Langmuir and Langmuir-Blodgett films: what and how ? KSV instruments LTD: Vol. application note 107.
2. Cote, L. J.; Kim, J.; Tung, V. C.; Luo, J. Y.; Kim, F.; Huang, J. X. *Pure and Applied Chemistry* **2011**, 83, (1), 95-110.
3. Cote, L. J.; Kim, F.; Huang, J. X. *Journal of the American Chemical Society* **2009**, 131, (3), 1043-1049.
4. Ling, X.; Zhang, J. *Small* **2010**, 6, (18), 2020-2025.
5. Szabo, T.; Hornok, V.; Schoonheydt, R. A.; Dekany, I. *Carbon* **2010**, 48, (5), 1676-1680.
6. Wang, X. L.; Bai, H.; Shi, G. Q. *Journal of the American Chemical Society* **2011**, 133, (16), 6338-6342.
7. Imperiali, L.; Liao, K. H.; Clasen, C.; Fransaer, J.; Macosko, C. W.; Vermant, J. *Langmuir* **2012**, 28, (21), 7990-8000.
8. Gengler, R. Y. N.; Veligura, A.; Enotiadis, A.; Diamanti, E. K.; Gournis, D.; Jozsa, C.; van Wees, B. J.; Rudolf, P. *Small* **2010**, 6, (1), 35-39.
9. Sutar, D. S.; Narayanam, P. K.; Singh, G.; Botcha, V. D.; Talwar, S. S.; Srinivasa, R. S.; Major, S. S. *Thin Solid Films* **2012**, 520, (18), 5991-5996.
10. Sutar, D. S.; Singh, G.; Botcha, V. D. *Applied Physics Letters* **2012**, 101, (10).
11. Gao, Y.; Chen, X. Q.; Xu, H.; Zou, Y. L.; Gu, R. P.; Xu, M. S.; Jen, A. K. Y.; Chen, H. Z. *Carbon* **2010**, 48, (15), 4475-4482.
12. Zheng, Q. B.; Ip, W. H.; Lin, X. Y.; Yousefi, N.; Yeung, K. K.; Li, Z. G.; Kim, J. K. *Acs Nano* **2011**, 5, (7), 6039-6051.
13. Zheng, Q. B.; Shi, F.; Yang, J. H. *Transactions of Nonferrous Metals Society of China* **2012**, 22, (10), 2504-2511.
14. Ramesha, G. K.; Kumara, A. V.; Sampath, S. *The Journal of Physical Chemistry C* **2012**, 116, (26), 13997-14004.
15. Narayanam, P. K.; Singh, G.; Botcha, V. D.; Sutar, D. S.; Talwar, S. S.; Srinivasa, R. S.; Major, S. S. *Nanotechnology* **2012**, 23, (32).
16. Li, X. L.; Zhang, G. Y.; Bai, X. D.; Sun, X. M.; Wang, X. R.; Wang, E.; Dai, H. J. *Nature Nanotechnology* **2008**, 3, (9), 538-542.

17. Cao, Y.; Wei, Z. M.; Liu, S.; Gan, L.; Guo, X. F.; Xu, W.; Steigerwald, M. L.; Liu, Z. F.; Zhu, D. B. *Angewandte Chemie-International Edition* **2010**, 49, (36), 6319-6323.
18. Kulkarni, D. D.; Choi, I.; Singamaneni, S.; Tsukruk, V. V. *Acs Nano* **2010**, 4, (8), 4667-4676.
19. Yin, Z. Y.; He, Q. Y.; Huang, X.; Zhang, J.; Wu, S. X.; Chen, P.; Lu, G.; Zhang, Q. C.; Yan, Q. Y.; Zhang, H. *Nanoscale* **2012**, 4, (1), 293-297.
20. Lake, J. R.; Cheng, A.; Selverston, S.; Tanaka, Z.; Koehne, J.; Meyyappan, M.; Chen, B. *Journal of Vacuum Science & Technology B* **2012**, 30, (3).
21. Petersen, S.; Glyvradal, M.; Boggild, P.; Hu, W. P.; Feidenhans'l, R.; Laursen, B. W. *Acs Nano* **2012**, 6, (9), 8022-8029.
22. Zheng, Q. B.; Zhang, B.; Lin, X. Y.; Shen, X.; Yousefi, N.; Huang, Z. D.; Li, Z. G.; Kim, J. K. *Journal of Materials Chemistry* **2012**, 22, (48), 25072-25082.
23. Park, K. H.; Kim, B. H.; Song, S. H.; Kwon, J.; Kong, B. S.; Kang, K.; Jeon, S. *Nano Letters* **2012**, 12, (6), 2871-2876.
24. Seo, S.; Jin, C.; Jang, Y. R.; Lee, J.; Kim, S. K.; Lee, H. *Journal of Materials Chemistry* **2011**, 21, (15), 5805-5811.
25. Li, H.; Cao, X. H.; Li, B.; Zhou, X. Z.; Lu, G.; Liusman, C.; He, Q. Y.; Boey, F.; Venkatraman, S. S.; Zhang, H. *Chemical Communications* **2011**, 47, (36), 10070-10072.



## Chapter 3

# A bottom-up approach for the synthesis of highly ordered fullerene-intercalated graphene hybrids

Much of the research effort on graphene focuses on its use as a building block for the development of new hybrid nanostructures with well-defined dimensions and properties suitable for applications such as gas storage, heterogeneous catalysis, gas/liquid separations, nanosensing and biomedicine. Toward this aim, here we describe a new bottom-up approach, which combines self-assembly with the Langmuir-Schaefer deposition technique to synthesize graphene-based layered hybrid materials hosting pristine fullerene molecules within the interlayer space. Our film preparation consists in a bottom-up layer-by-layer process that proceeds via the formation of a hybrid organo-graphene oxide Langmuir film. The structure and composition of these hybrid fullerene-containing thin multilayers deposited on hydrophobic substrates were characterized by a combination of X-ray diffraction, Raman and X-ray photoelectron spectroscopies, atomic force and scanning electron microscopies and conductivity measurements. The latter revealed that the presence of C<sub>60</sub> within the interlayer spacing leads to an increase in electrical conductivity of the hybrid material as compared to the organo-graphene matrix alone.

---

This chapter is based on the article: "A bottom-up approach for the synthesis of highly ordered fullerene-intercalated graphene hybrids", by A. Kouloumpis, K. Dimos, K. Spyrou, V. Georgakilas, P. Rudolf and D. Gournis. *Frontiers in Materials* 2015, 2, 10

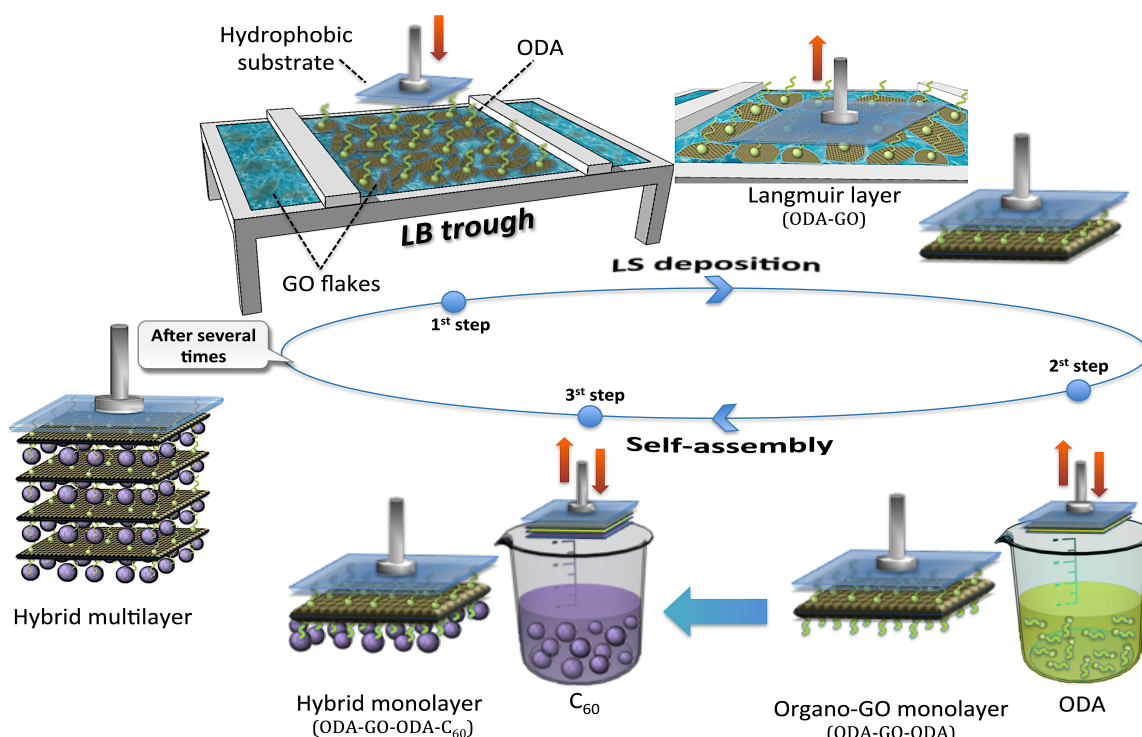
### **3.1 Introduction**

The outstanding mechanical, thermal and electrical properties of graphene have attracted a lot of scientific effort aimed at exploiting them in the development of new hybrid nanostructures with well-defined dimensions and behaviour, which contain graphene as building block.<sup>1,2</sup> In fact, graphene sheets can be used as templates for the synthesis of novel intercalated carbon-based materials suitable for various applications in gas storage, gas/liquid separation, heterogeneous catalysis, energy storage, Li-ion batteries, supercapacitors, nanosensing and biomedicine.<sup>1, 3-7</sup> Combining graphene's properties with the extraordinary properties of fullerenes<sup>8,9</sup> by incorporating the latter into well-defined graphene-based hybrid thin multilayers continues to be a challenging new field for developing novel hybrid nanocomposites.

Here we describe a new bottom-up layer-by-layer approach for the production of graphene hybrid materials where graphene acts as the structure directing interface and reaction media. This method, based on combining self-assembly with the Langmuir-Schaefer (LS) deposition technique, uses the graphene nanosheets as a template for incorporating C<sub>60</sub> molecules in a bi-dimensional array and allows for perfect layer-by-layer growth with control at the molecular level.<sup>10</sup> Similar synthetic protocols have been reported during the last decade for the development of hybrid multilayers and monolayers using the Langmuir Blodgett (LB) technique. Layered materials like clay minerals,<sup>10-20</sup> graphene and/or graphene oxide,<sup>13, 21-23</sup> or other carbon-based nanostructures<sup>24-26</sup> have been used to produce hybrid thin multilayers with unique properties. Clay minerals with amphiphilic species and other complexes were combined to fabricate monolayers and multilayers used as photoprobes,<sup>27</sup> sensors,<sup>18</sup> catalysts<sup>20</sup> and photomagnetic films.<sup>17, 28</sup> Moreover, the optoelectronic and mechanical properties of graphene can be modified, tuned, or enhanced by layer-by-layer assembly techniques such as the LB method, as has been reported in various studies over the last 3-4 years (for a review see<sup>29</sup>). High performance dye-sensitized solar cells,<sup>30</sup> and transparent conductive films<sup>31</sup> are some examples of the uses of hybrid graphene-based thin multilayers. Finally, the advantages of the precise control and the homogeneous deposition over large areas makes the LB technique

promising for preventing carbon-based nanostructures from agglomerating during the film synthesis, as demonstrated for fullerene derivatives or carbon dots.<sup>24-26</sup>

Our film preparation approach involves a bottom-up layer-by-layer process that starts with the formation of a hybrid organo-graphene Langmuir film and proceeds via two self-assembly steps to create a layered structure hosting fullerene molecules within its interlayer space (a schematic representation of the synthetic procedure is illustrated in Scheme 3.1). The composition, structure and transport properties of the fullerene-containing hybrid thin multilayers deposited on hydrophobic substrates were characterized by X-ray diffraction, Raman and X-ray photoelectron spectroscopies, atomic force and scanning electron microscopies and electrical conductivity measurements.



**Scheme 3.1.** Schematic representation of the synthetic procedure followed for the synthesis of the hybrid GO/C<sub>60</sub> multilayer film consisting in a Langmuir Schaefer deposition (1<sup>st</sup> step) combined with two self-assembly steps (2<sup>nd</sup> and 3<sup>rd</sup> step).

## **3.2 Experimental Section**

### **3.2.1 Materials**

Sulfuric acid (95-97%), nitric acid (65%), potassium chlorate ( $\geq 99\%$ ) and powder graphite (pulum,  $\leq 0.2$  mm) were supplied from Fluka. Octadecylamine (ODA,  $\geq 99\%$ ), acetone, methanol and ethanol were purchased from Sigma-Aldrich while fullerene ( $C_{60}$ , powder, 99% C) was obtained from Alfa Aesar. Ultrapure deionized water (18.2 M $\Omega$ ) produced by a Millipore Simplicity® system was used throughout. The Si-wafer (P/Bor, single side polished, purchased from Si-Mat) substrates were cleaned prior to use by 15 min ultrasonication in water, acetone and ethanol. All reagents were of analytical grade and were used without further purification.

### **3.2.2 Synthesis of graphene oxide**

Graphene oxide (GO) was synthesized using a modified Staudenmaier method:<sup>13, 32, 33</sup> 10 g of powdered graphite were added to a mixture of 400 mL of 95-97%  $H_2SO_4$  and 200 mL of 65%  $HNO_3$ , while cooling in an ice-water bath. 200 g of powdered  $KClO_3$  were added to the mixture in small portions under vigorous stirring while cooling in the ice-water bath. The reaction was quenched after 18 h by pouring the mixture into ultrapure water; the oxidation product was washed until the pH reached 6.0 and finally dried at room temperature.

### **3.2.3 Preparation of hybrid graphene/fullerene multilayers**

A KSV 2000 Nima Technology Langmuir Blodgett trough was used for the preparation and deposition of multilayers at a temperature of  $21 \pm 0.5^\circ C$ . The surface pressure in the LB trough was monitored with a Pt Wilhelmy plate. The deposition protocol is schematically illustrated in Scheme 1. A GO suspension in ultrapure water (0.02 mg mL<sup>-1</sup>) was used as subphase. 200  $\mu L$  of a 0.2 mg mL<sup>-1</sup> ODA solution in chloroform/methanol 9/1 (v/v) were spread onto the water surface using a microsyringe to achieve the hybridization of GO sheets by covalent bonding via the amide functionality. After a waiting time of 20 min to allow for solvent evaporation and GO-surfactant functionalization to occur, the hybrid ODA-GO layer was



compressed at a rate of  $5 \text{ mm min}^{-1}$  until the chosen stabilization pressure of  $20 \text{ mN m}^{-1}$  was reached. As in any classical Langmuir Blodgett experiment, the applied pressure pushes the surfactant molecules along the water surface; the grafted graphene oxide sheets will simply follow that movement and therefore become packed, depending on the surface tension established in the trough.<sup>13</sup> This pressure was maintained throughout the deposition process. Layers were transferred onto the hydrophobic Si-wafer substrates by horizontal dipping (this way of transferring is known as Langmuir-Schaefer technique), with downward and lifting speeds of  $10$  and  $5 \text{ mm min}^{-1}$ , respectively<sup>23</sup> - 1<sup>st</sup> step in Scheme 3.1. After the horizontal lift of the substrate, the 2<sup>nd</sup> step of the deposition protocol consisted in a surface modification of the GO nanosheets, induced by bringing the surface of the transferred Langmuir film (ODA-GO) in contact with a solution of ODA surfactant (self-assembly) dissolved in methanol ( $0.2 \text{ mg mL}^{-1}$ )<sup>13</sup> as illustrated in Scheme 3.1. In the 3<sup>rd</sup> and final step, the hybrid organo-GO film was lowered into a solution of  $\text{C}_{60}$  in toluene ( $0.2 \text{ mg mL}^{-1}$ ) for the formation of a hybrid graphene/fullerene monolayer by self-assembly. A hybrid multilayer film was constructed by repeating this 3-step-dipping cycle 40 times, as shown in Scheme 3.1 (sample denoted as **ODA-GO-ODA-C<sub>60</sub>**). Each time when the substrate was lowered towards the liquid surface, it was allowed to touch the air-water interface or the solution surface in a very gentle dip of max  $0.5 \text{ mm}$  below the surface for  $90 \text{ s}$ . After each deposition step the sample was rinsed several times by dipping into ultrapure water to eliminate any weakly attached molecules that remained from the deposition step and dried with nitrogen flow to avoid contaminating the Langmuir film air-water interface or the solution employed in the following step.<sup>10, 21</sup> For comparison an organo-GO hybrid multilayer (40 layers) was also fabricated under the same experimental conditions without the 3<sup>rd</sup> step of  $\text{C}_{60}$  incorporation (sample denoted as **ODA-GO-ODA**). Moreover, a reduction and an annealing step (4<sup>th</sup> step) were also performed in both multilayers in order to convert the deposited GO to graphene and thus to increase the conductivity. For this, the deposited multilayers were immersed into an aqueous solution of  $\text{NaBH}_4$  ( $1 \text{ mg mL}^{-1}$ ) for  $10 \text{ min}$  and annealed at  $700 \text{ }^\circ\text{C}$  for  $1 \text{ h}$  under argon (samples denoted as **ODA-rGO-ODA-C<sub>60</sub>** and **ODA-rGO-ODA**). This treatment results in a partial reconstruction of the graphene mesh and consequently causes a drastic increase in conductivity.<sup>13</sup>

### 3.3 Results and Discussion

#### 3.3.1 Structure control of hybrid ODA-GO layer

The surface pressure versus molecular area ( $\pi$ -A) isotherms of ODA monolayers in pure water and on GO dispersion are shown in Figure 3.1 (right). The curves show the change in the slope corresponding to the phase transitions of ODA-GO sheets from gas to condensed-liquid and then to solid state during the compression process.<sup>21</sup> In the absence of GO, the  $\pi$ -A isotherm is a smoothly increasing curve with a lift off area of  $32.8 \text{ \AA}^2$ . When adding a small amount of GO ( $0.02 \text{ mg mL}^{-1}$ ) to the aqueous subphase, the lift-off area increased to  $52 \text{ \AA}^2$ , verifying that GO flakes cause a stabilization effect on the ODA layer<sup>21</sup> through chemical grafting (covalent bonding) of the terminal amine groups of ODA to the epoxide groups on the top side of the GO sheets. The amine end groups interact via a ring opening reaction (nucleophilic substitution reactions) of the epoxide groups of GO.<sup>13, 34, 35</sup> At surface pressures above  $40 \text{ mN m}^{-1}$  the monolayer collapses due to the formation of bilayers at approximately  $26 \text{ \AA}^2$ .<sup>21</sup>

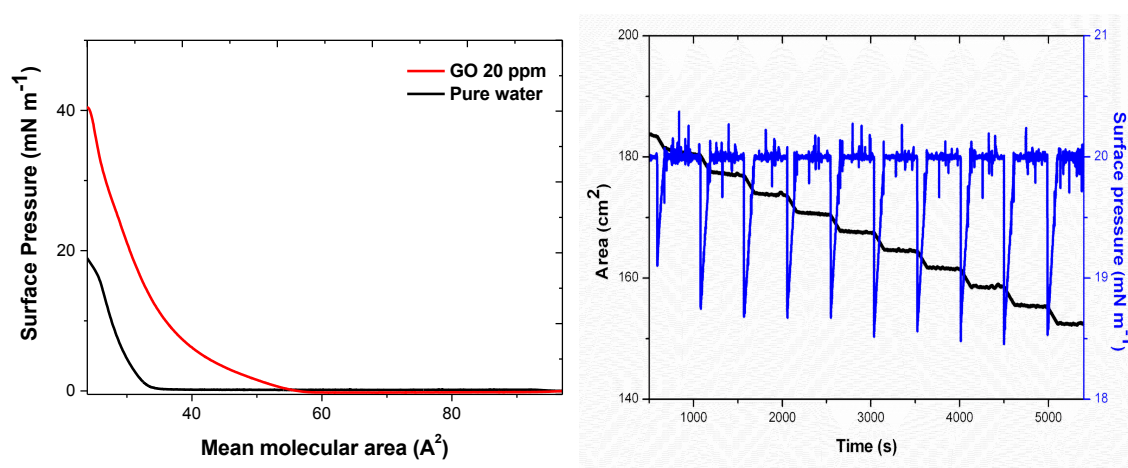


**Figure 3.1.** (Left panel)  $\pi$ -A isotherms of ODA monolayers in pure water and on an aqueous dispersion of  $0.02 \text{ mg mL}^{-1}$  GO. (Right panel) The black curve corresponds to the trough area covered by the hybrid ODA-GO Langmuir film at the air-water surface and the blue curve shows the surface pressure throughout (around  $20 \text{ mN m}^{-1}$ ) the deposition of a 10-layer ODA-GO-ODA-C<sub>60</sub> hybrid film.

The successful transfer of the hybrid Langmuir films onto the Si-wafer substrate can be deduced from the plot of the pressure measured at the surface of the subphase in the LB trough versus time.<sup>10</sup> Figure 3.1 (right) shows the time dependence of the total trough area of the hybrid Langmuir film. As the substrate is dipped into the subphase, this area reduces due to the transfer of one hybrid layer from the air-water interface to the substrate during each dip. This transfer is visible as a sharp step in the curve.<sup>10, 11</sup> If the step height (which gives an area value) is equal to the substrate surface area, the transfer ratio is 1 and the substrate surface is 100% covered by the hybrid layer each time it is lowered into the subphase. A different transfer ratio suggests a multilayer transfer or an incomplete coverage of the substrate.<sup>10</sup> The curve shown in Figure 3.1 is a typical one recorded during the deposition of a 10-layer hybrid ODA-GO-ODA-C<sub>60</sub> film. The transfer ratio was very close to 1 throughout the deposition, testifying to the successful transfer of the hybrid Langmuir film at each dip of substrate into the LB trough.

Representative AFM images of hybrid graphene oxide sheets (ODA-GO) deposited on Si-wafer with the LS method (at surface pressure 20 mN m<sup>-1</sup>) during the first dip into the LB trough (1<sup>st</sup> step in Scheme 3.1) are shown in Figure 3.2. In these images one recognizes high quality graphene oxide flakes with well-defined edges and a relatively low amount of cracks and wrinkles. The surface coverage is quite high; the GO platelets in the transferred layer are contacting each other, with hardly any overlap but only small voids between them, forming a nearly continuous, close-packed array. The average height of the flakes is 0.9-1.5 nm as derived from topographical height profile is larger than the value of 0.61 nm predicted for a single graphene oxide layer,<sup>36</sup> as expected due to the ODA layer below the GO sheet. However, it is difficult to conclude anything on the orientation of the ODA molecules (straight or inclined) from these images because the height of single GO layers without ODA has also been found in the literature to be of the order of 1.1±0.2 nm (see for example<sup>37, 38</sup>) probably due to presence of adsorbed water molecules.

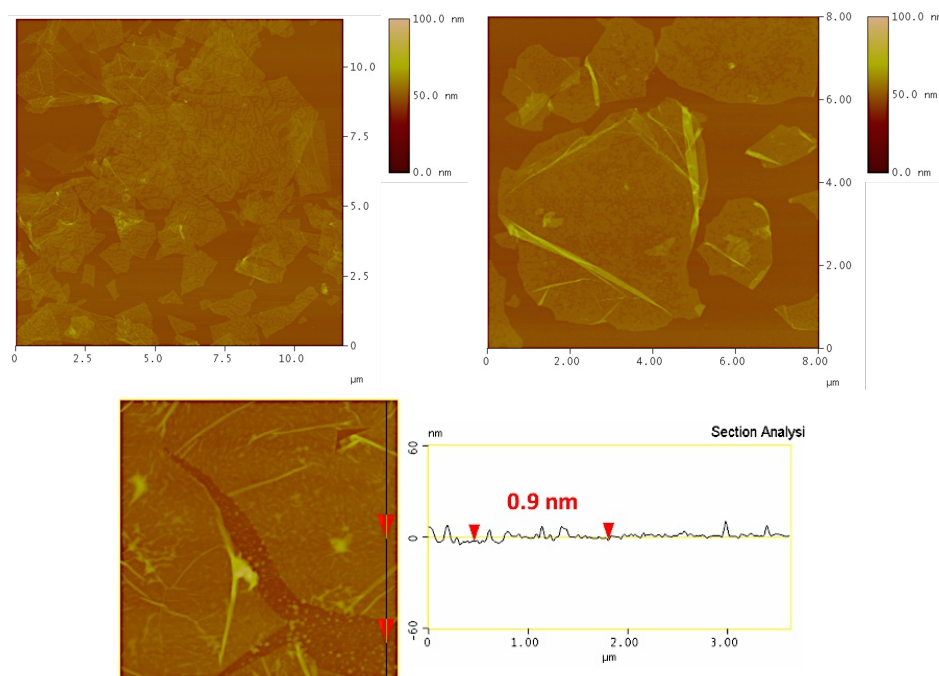


**Figure 3.2.** Tapping mode AFM micrographs (and line profile) of an ODA-GO monolayer deposited with the Langmuir-Schaefer technique at a surface pressure of  $20 \text{ mN m}^{-1}$ .

### 3.3.2 Characterization of hybrid graphene/fullerene multilayers

The X-ray diffraction pattern of a ODA-GO-ODA- $C_{60}$  hybrid multilayer (40 layers) is shown in Figure 3.3 in comparison with a ODA-GO-ODA hybrid multilayer (40 layers) that was synthesized under the same experimental conditions. The ODA-GO-ODA- $C_{60}$  hybrid multilayer shows a 001 diffraction peak at  $2\theta=2.2^\circ$  which corresponds to a  $d_{001}$ -spacing of  $40 \text{ \AA}$ . This value is higher compared with the corresponding value of the ODA-GO-ODA multilayer ( $d_{001}=37.6 \text{ \AA}$ ) testifying to the successful intercalation of the fullerene between the organo-graphene nanosheets. This increment does not correspond to the size of  $C_{60}$  ( $\sim 7 \text{ \AA}$ ) implying that the fullerene molecules are accommodated between the double alkyl chains of the surfactant (see inset sketch) and not on top of it. Moreover, the absence of higher order (001) reflections in the XRD pattern of ODA-GO-ODA- $C_{60}$  suggests that the graphene oxide layers are not stacked in perfect registry but have slipped sideways and are turbostratically disordered.

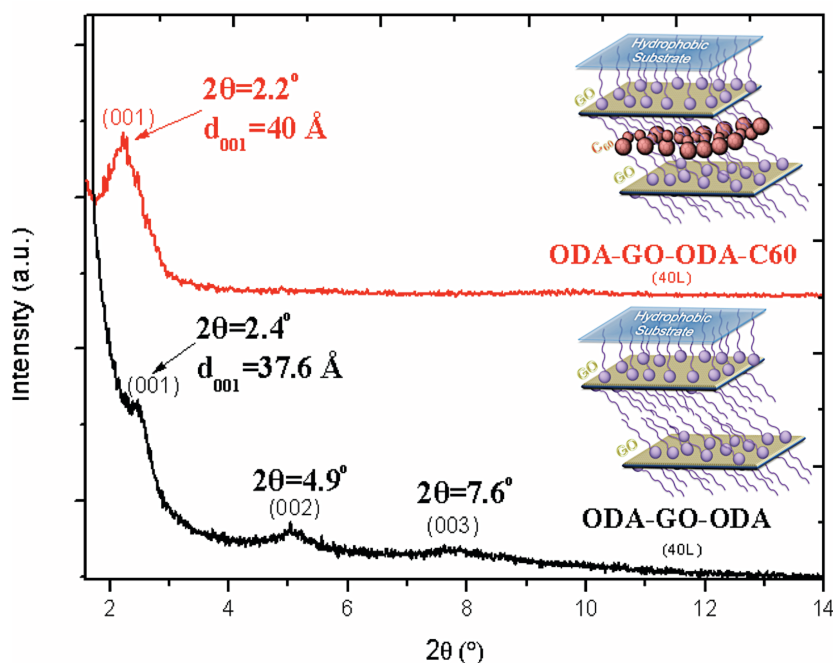


**Figure 3.3.** XRD patterns of ODA-GO-ODA-C<sub>60</sub> and ODA-GO-ODA hybrid multilayers (40 layers).

A similar behaviour has been observed upon intercalation of fullerene derivatives in aluminosilicate clay minerals.<sup>39</sup> This hypothesis is further supported by calculating the size of the coherently diffracting domains along the *c* axis (also called mean crystalline thickness, *t*) that give rise to the 001 diffraction peak, given by the Debye-Scherrer equation,  $t = K\lambda/\beta\cos\theta$ , where *K* is a constant near unity ( $K = 0.91$ ),  $\lambda$  the X-ray wavelength ( $\lambda = 1.5418 \text{ \AA}$ ),  $\theta$  the angular position of the first diffraction peak, and  $\beta$  the full width at half maximum of the 001 peak expressed in radians. The crystalline thickness (*t*) along *c* axis of the ODA-GO-ODA-C<sub>60</sub> and ODA-GO-ODA multilayers is found to be 114 and 153  $\text{\AA}$ , respectively. Dividing these values with the corresponding  $d_{001}$ -spacings, the number of stacked layers can be calculated to be  $\sim 3$  for ODA-GO-ODA-C<sub>60</sub> and  $\sim 4$  for ODA-GO-ODA, confirming the high degree of ordering of the produced multilayers.

Raman spectra of the hybrid ODA-GO-ODA-C<sub>60</sub> and the ODA-GO-ODA multilayer samples are shown in Figure 3.4. Spectra are typical of GO materials, in that both exhibit the characteristic first-ordered G- and D-bands at around 1600 and 1350  $\text{cm}^{-1}$ , respectively. The G-band is associated with  $sp^2$  hybridized carbon atoms and originates from the doubly degenerate zone center  $E_{2g}$  mode. The D-band is

correlated with  $sp^3$  hybridized carbon atoms, as it requires a defect for its activation by double resonance, thus indicating the presence of lattice defects and distortions.<sup>40, 41</sup> The ratio of the D- to G-band intensities ( $I_D/I_G$ ) is indicative of the quality of the graphitic lattice. This ratio is equal to 1.06 for the ODA-GO-ODA- $C_{60}$  multilayer and 1.04 for the ODA-GO-ODA multilayer, implying that fullerene intercalation into the interlayer space of the organo-graphene nanosheets does not influence the GO structure. In addition, the shape of the two spectra in the 2D region is alike; both exhibit two broad peaks at  $\sim 2700$  and  $\sim 2930$   $cm^{-1}$ . The low intensity  $2700$   $cm^{-1}$  peak is attributed to the 2D (or else  $G'$ ) vibrational mode, which is an overtone (second order) of the D peak. The second peak at  $\sim 2930$   $cm^{-1}$  is assigned to the mode  $D+D'$ , originating from the combination of phonons with different momenta, thus requiring defects for its activation; its intensity agrees with the defective nature of the GO lattice revealed by the high  $I_D/I_G$  ratios of both samples.<sup>40-</sup>  
<sup>43</sup> The typical pentagonal pinch mode ( $A_g(2)$ ) of  $C_{60}$  that is expected between  $1440$  and  $1470$   $cm^{-1}$ <sup>44</sup> is not visible since it is superimposed on the broad D band of graphene oxide. Moreover, upon reduction and annealing (see Figure 3.4 inset), the GO sheets show a noticeable decrease in the D/G ratio from 1.06 to 0.76.

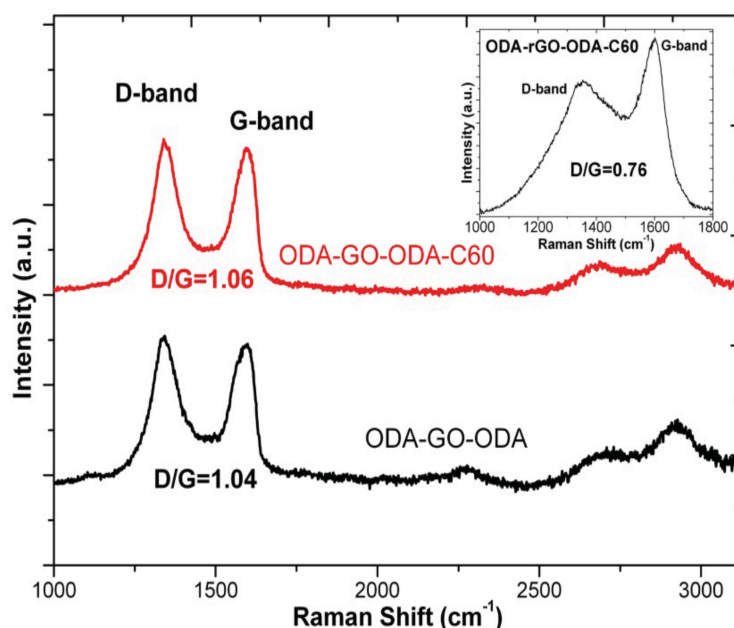


**Figure 3.4.** Raman spectra of ODA-GO-ODA- $C_{60}$  and ODA-GO-ODA hybrid multilayers (40 layers), Inset: Raman spectrum of the ODA-rGO-ODA- $C_{60}$  hybrid multilayer after reduction and annealing.

This observation suggests that while most of the oxygenated groups are removed (in the form of CO or CO<sub>2</sub>), the relative amount of disordered sp<sup>2</sup>-hybridized atoms is still high. The later could be explained either by the fact that amine molecules covalently bound to graphene survive the reduction and annealing procedures (contributing to an enhanced sp<sup>3</sup> hybridization) or that vacancies created during production of GO remain unchanged by the reduction process and ultimately define the intact graphene regions.<sup>13, 37, 45</sup>

The C1s core level X-ray photoelectron spectra of the graphene/fullerene hybrid multilayers before (ODA-GO-ODA-C<sub>60</sub>) and after reduction and annealing (ODA-rGO-ODA-C<sub>60</sub>) in comparison with pristine GO and the organo-GO multilayers (ODA-GO-ODA) are shown in Figure 3.5. The spectrum of ODA-GO-ODA displays four main contributions at 285.0 eV, 286.1 eV, 287.5 eV and 289.3 eV corresponding to different carbon environments while for ODA-GO-ODA-C<sub>60</sub> an additional contribution appear at 290.5 eV. The peak at 285.0 eV is attributed to the C-C bonds of the aromatic ring of GO as well the organic carbon-carbon groups of ODA attached to graphene and represents 53.7% of the total carbon 1s intensity of ODA-GO-ODA (Figure 3.5 top-right). This contribution is more intense in the case of ODA-GO-ODA-C<sub>60</sub> (Figure 3.5 bottom-left) because in addition to photoemission signal due to the C-C bonds of ODA and GO as also that from the C<sub>60</sub> cage appears at this binding energy. The increased intensity of this peak to 57.9% of the total C1s signal testifies therefore to the successful incorporation of C<sub>60</sub> into the layered structure. C-O and C-N both contribute to the photoelectron peak centred at 286.1 eV for ODA-GO-ODA and 286.5 eV for ODA-GO-ODA-C<sub>60</sub>; in both spectra its intensity is higher than in the corresponding spectrum of the GO starting material due to the chemical grafting of the amino groups of ODA with the epoxy groups of GO. Similarly, the contribution at 287.5 eV in the ODA-GO-ODA spectrum (at 288.0 eV for ODA-GO-ODA-C<sub>60</sub>), assigned to the epoxy groups of GO, is smaller than for the GO starting material, attesting that the epoxy groups have reacted with the amines via chemical grafting. The peak at 289.3 eV in the ODA-GO-ODA spectrum (at 289.1 eV for ODA-GO-ODA-C<sub>60</sub>) is attributed to carboxyl groups created during the oxidation of GO. The additional peak at 290.5 eV in the ODA-GO-ODA-C<sub>60</sub> spectrum is due to the C1s shake up features of C<sub>60</sub>,<sup>46</sup> which result from π-π\* transitions excited in the

photoemission process; this peak therefore gives additional support to the presence of fullerenes in the hybrid multilayer.<sup>10, 47</sup> Finally, upon reduction and subsequent annealing at 700°C the C1s spectral intensity due to oxygen-containing functional groups of graphene oxide (Figure 3.5 bottom-right) is significantly lower as compared to before the treatment, indicating a partial reconstruction of the graphene network expected to result in a better electrical conductivity (see below). It is noteworthy to mention that a new photoemission peak appears in the same spectrum at 282.9 eV; we attribute this peak to C-Si bonds formed as a result of the annealing procedure. Finally, no contribution in N1s photoelectron peak was observed in both ODA-rGO-ODA and ODA-rGO-ODA-C<sub>60</sub> samples indicating that annealing didn't cause any nitrogen doping in the graphene layers.

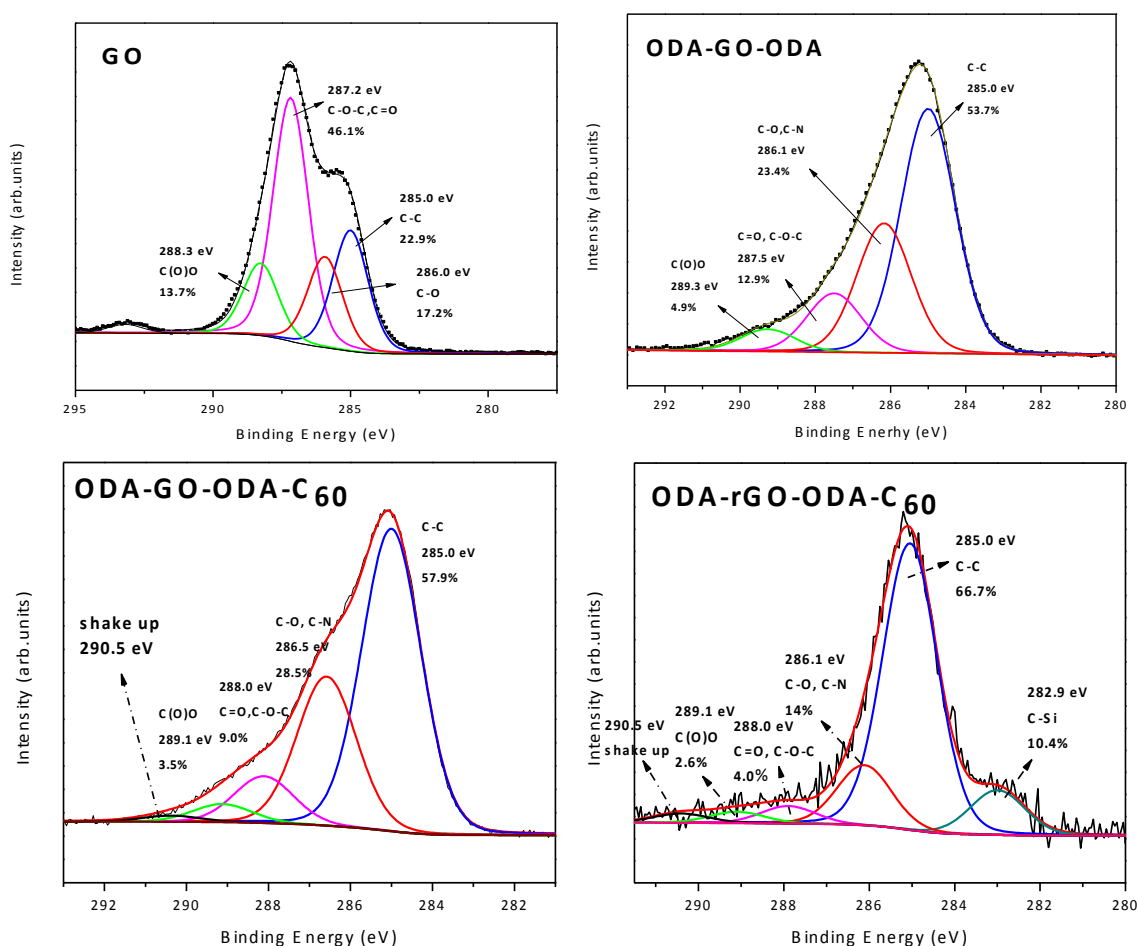


**Figure 3.5.** X-ray photoelectron spectra of the C1s core level region of GO, ODA-GO-ODA and graphene/fullerene hybrid multilayers (40 layers) before (ODA-GO-ODA-C<sub>60</sub>) and after reduction and annealing (ODA-rGO-ODA-C<sub>60</sub>).



The sheet resistance measurements of the ODA-GO-ODA and ODA-GO-ODA-C<sub>60</sub> multilayers gave values of about 15-20 MΩ and 10 MΩ, respectively. These values were remarkably reduced to 20 kΩ and 4 kΩ, respectively, after the reduction and annealing treatment was applied in order to convert the deposited GO to graphene.

These values are mean values of all measurements performed in different spots on both samples. By taking into account the thickness (as estimated from AFM section analysis) of the produced films (70 nm for ODA-rGO-ODA and 90 nm for ODA-rGO-ODA-C<sub>60</sub>) the electrical conductivity of the produced films was estimated 714 S·m<sup>-1</sup> and 2800 S·m<sup>-1</sup> for the reduced and annealed samples without and with the C<sub>60</sub> respectively. It is worth to notice that the produced multilayer films have a quite uniform and smooth surface as revealed by SEM measurements (Figure 3.6). According to the roughness analysis of the surface shown in the inset of Figure 3.6, the mean roughness (RMS) is estimated around 3 nm. The poor electrical conductivity of both the ODA-GO-ODA and the ODA-GO-ODA-C<sub>60</sub> multilayer is due to the presence of ODA and of the oxygen-containing groups decorating the graphene oxide sheets. However, the reduction and annealing steps substantially improved the electrical conductivity by removing effectively these moieties. The difference in sheet resistance between the two multilayers indicates a strong influence of the presence of C<sub>60</sub>. It is clear that the presence of C<sub>60</sub> inserted between graphene layers increases the electrical conductivity by an order of magnitude.

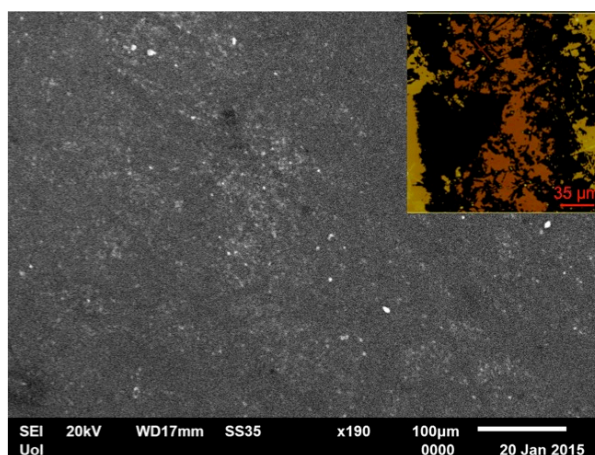


**Figure 3.6.** Representative SEM image of ODA-rGO-ODA-C<sub>60</sub>. Inset: surface roughness analysis of the same sample as shown by AFM micrograph.

### **3.4 Conclusions**

In conclusion, a highly controllable layer-by-layer synthetic approach for the production of a new class of hybrid carbonaceous structures was discussed. A 40-layer thick film consisting of organo-modified graphene oxide layers accommodating pure fullerene molecules ( $C_{60}$ ) in the interlayer space was successfully fabricated by using a combination of the Langmuir-Schaefer deposition method with two self-assembly steps from solution. Initially, the effectiveness of this method in terms of coverage, uniformity and single-layer-level control of the assembly of the first organo-modified graphene oxide layer was confirmed by  $\pi$ -A isotherm measurements and AFM microscopy. For the hybrid multilayer sample X-ray diffraction measurements revealed the presence of the fullerene molecules within the interlayer space between the turbostratically layered organo-graphene oxide nanosheets and confirmed the high degree of ordering of the produced structure. The existence of fullerenes in the hybrid multilayer system was confirmed by X-ray photoelectron spectroscopy while Raman spectroscopy showed that the intercalation of the fullerene within the interlayer space of the organo-graphene oxide nanosheets did not affect the structure of GO itself. Finally, a considerable improvement (an order of magnitude) of the electrical conductivity of the hybrid multilayer with respect to the organo-graphene analogue was observed due to the presence of  $C_{60}$  inserted between graphene oxide layers. This graphene/fullerene hybrid material constitutes a novel hybrid system that could ideally be used in diverse applications such as transparent electrodes, thin film transistors, supercapacitors or lubricants.

### 3.5 References

1. Wang, D.; Kou, R.; Choi, D.; Yang, Z.; Nie, Z.; Li, J.; Saraf, L. V.; Hu, D.; Zhang, J.; Graff, G. L.; Liu, J.; Pope, M. A.; Aksay, I. A. *ACS Nano* **2010**, 4, (3), 1587-1595.
2. Yin, S.; Niu, Z.; Chen, X. *Small* **2012**, 8, (16), 2458-2463.
3. Lei, Z.; Christov, N.; Zhao, X. S. *Energy Environ. Sci.* **2011**, 4, (5), 1866-1873.
4. Yu, D.; Dai, L. *The Journal of Physical Chemistry Letters* **2009**, 1, (2), 467-470.
5. Patil, A. J.; Vickery, J. L.; Scott, T. B.; Mann, S. *Adv. Mater.* **2009**, 21, (31), 3159-3164.
6. Chen, W.; Li, S.; Chen, C.; Yan, L. *Adv. Mater.* **2011**, 23, (47), 5679-5683.
7. Choi, B. G.; Park, H.; Park, T. J.; Yang, M. H.; Kim, J. S.; Jang, S.-Y.; Heo, N. S.; Lee, S. Y.; Kong, J.; Hong, W. H. *ACS Nano* **2010**, 4, (5), 2910-2918.
8. Iijima, S. *Nature* **1991**, 354, (6348), 56-58.
9. Guldi, D. M.; Prato, M. *Acc. Chem. Res.* **2000**, 33, (10), 695-703.
10. Gengler, R. Y. N.; Gournis, D.; Aimon, A. H.; Toma, L. M.; Rudolf, P. *Chemistry-a European Journal* **2012**, 18, (24), 7594-7600.
11. Toma, L. M.; Gengler, R. Y. N.; Prinsen, E. B.; Gournis, D.; Rudolf, P. *Physical Chemistry Chemical Physics* **2010**, 12, (38), 12188-12197.
12. Gengler, R. Y. N. A Modified Langmuir-Schaefer Method For the Creation of Functional Thin Films. PhD Thesis, University of Groningen, Groningen, 2010.
13. Gengler, R. Y. N.; Veligura, A.; Enotiadis, A.; Diamanti, E. K.; Gournis, D.; Jozsa, C.; van Wees, B. J.; Rudolf, P. *Small* **2010**, 6, (1), 35-39.
14. Gengler, R. Y. N.; Toma, L. M.; Pardo, E.; Lloret, F.; Ke, X. X.; Van Tendeloo, G.; Gournis, D.; Rudolf, P. *Small* **2012**, 8, (16), 2532-2540.
15. Umemura, Y.; Yamagishi, A.; Schoonheydt, R.; Persoons, A.; De Schryver, F. *Langmuir* **2001**, 17, (2), 449-455.
16. Umemura, Y.; Yamagishi, A.; Schoonheydt, R.; Persoons, A.; De Schryver, F. *J. Am. Chem. Soc.* **2002**, 124, (6), 992-997.
17. Yamamoto, T.; Umemura, Y.; Sato, O.; Einaga, Y. *Chemistry of Materials* **2004**, 16, (7), 1195-1201.

18. Junxiang, H.; Sato, H.; Umemura, Y.; Yamagishi, A. *The Journal of Physical Chemistry B* **2005**, 109, (10), 4679-4683.
19. Umemura, Y.; Shinohara, E.; Schoonheydt, R. A. *Phys. Chem. Chem. Phys.* **2009**, 11, (42), 9804-9810.
20. Yoshida, J.; Saruwatari, K.; Kameda, J.; Sato, H.; Yamagishi, A.; Sun, L.; Corriea, M.; Villemure, G. *Langmuir* **2006**, 22, (23), 9591-9597.
21. Michopoulos, A.; Kouloumpis, A.; Gournis, D.; Prodromidis, M. I. *Electrochimica Acta* **2014**, 146, (0), 477-484.
22. Zheng, Q. B.; Ip, W. H.; Lin, X. Y.; Yousefi, N.; Yeung, K. K.; Li, Z. G.; Kim, J. K. *Acs Nano* **2011**, 5, (7), 6039-6051.
23. Cote, L. J.; Kim, F.; Huang, J. X. *Journal of the American Chemical Society* **2009**, 131, (3), 1043-1049.
24. Bourlinos, A. B.; Karakassides, M. A.; Kouloumpis, A.; Gournis, D.; Bakandritsos, A.; Papagiannouli, I.; Aloukos, P.; Couris, S.; Hola, K.; Zboril, R.; Krysmann, M.; Giannelis, E. P. *Carbon* **2013**, 61, 640-643.
25. Bourlinos, A. B.; Georgakilas, V.; Bakandritsos, A.; Kouloumpis, A.; Gournis, D.; Zboril, R. *Materials Letters* **2012**, 82, 48-50.
26. Bourlinos, A. B.; Bakandritsos, A.; Kouloumpis, A.; Gournis, D.; Krysmann, M.; Giannelis, E. P.; Polakova, K.; Safarova, K.; Hola, K.; Zboril, R. *Journal of Materials Chemistry* **2012**, 22, (44), 23327-23330.
27. Hagerman, M. E.; Salamone, S. J.; Herbst, R. W.; Payeur, A. L. *Chemistry of Materials* **2002**, 15, (2), 443-450.
28. Yamamoto, T.; Umemura, Y.; Sato, O.; Einaga, Y. *Chemistry Letters* **2004**, 33, (5), 500-501.
29. Kouloumpis, A.; Zygouri, P.; Dimos, K.; Gournis, D., Layer-by-Layer Assembly of Graphene-Based Hybrid Materials. In *Functionalization of Graphene*, Wiley-VCH Verlag GmbH & Co. KGaA: 2014; pp 359-400.
30. Roh, K.-M.; Jo, E.-H.; Chang, H.; Han, T. H.; Jang, H. D. *J. Solid State Chem.* **2014**, (0), DOI: 10.1016/j.jssc.2014.04.022.
31. Zheng, Q.; Ip, W. H.; Lin, X.; Yousefi, N.; Yeung, K. K.; Li, Z.; Kim, J.-K. *ACS Nano* **2011**, 5, (7), 6039-6051.

32. Stergiou, D. V.; Diamanti, E. K.; Gournis, D.; Prodromidis, M. I. *Electrochemistry Communications* **2010**, 12, (10), 1307-1309.
33. Staudenmaier, L. *Ber. Deut. Chem. Ges.* **1898**, 31, 1481.
34. Bourlinos, A. B.; Gournis, D.; Petridis, D.; Szabo, T.; Szeri, A.; Dekany, I. *Langmuir* **2003**, 19, (15), 6050-6055.
35. Dreyer, D. R.; Park, S.; Bielawski, C. W.; Ruoff, R. S. *Chemical Society Reviews* **2010**, 39, (1), 228-240.
36. Dekany, I.; Kruger-Grasser, R.; Weiss, A. *Colloid and Polymer Science* **1998**, 276, (7), 570-576.
37. Gomez-Navarro, C.; Weitz, R. T.; Bittner, A. M.; Scolari, M.; Mews, A.; Burghard, M.; Kern, K. *Nano Letters* **2007**, 7, (11), 3499-3503.
38. Schniepp, H. C.; Li, J. L.; McAllister, M. J.; Sai, H.; Herrera-Alonso, M.; Adamson, D. H.; Prud'homme, R. K.; Car, R.; Saville, D. A.; Aksay, I. A. *J. Phys. Chem. B* **2006**, 110, (17), 8535-8539.
39. Gournis, D.; Jankovic, L.; Maccallini, E.; Benne, D.; Rudolf, P.; Colomer, J. F.; Sooambar, C.; Georgakilas, V.; Prato, M.; Fanti, M.; Zerbetto, F.; Sarova, G. H.; Guldi, D. M. *Journal of the American Chemical Society* **2006**, 128, (18), 6154-6163.
40. Ferrari, A. C.; Meyer, J. C.; Scardaci, V.; Casiraghi, C.; Lazzeri, M.; Mauri, F.; Piscanec, S.; Jiang, D.; Novoselov, K. S.; Roth, S.; Geim, A. K. *Physical Review Letters* **2006**, 97, (18), 187401.
41. Torrisi, F.; Hasan, T.; Wu, W.; Sun, Z.; Lombardo, A.; Kulmala, T. S.; Hsieh, G.-W.; Jung, S.; Bonaccorso, F.; Paul, P. J.; Chu, D.; Ferrari, A. C. *ACS Nano* **2012**, 6, (4), 2992-3006.
42. Cançado, L. G.; Jorio, A.; Ferreira, E. H. M.; Stavale, F.; Achete, C. A.; Capaz, R. B.; Moutinho, M. V. O.; Lombardo, A.; Kulmala, T. S.; Ferrari, A. C. *Nano Letters* **2011**, 11, (8), 3190-3196.
43. Martins Ferreira, E. H.; Moutinho, M. V. O.; Stavale, F.; Lucchese, M. M.; Capaz, R. B.; Achete, C. A.; Jorio, A. *Physical Review B* **2010**, 82, (12), 125429.
44. Spyrou, K.; Kang, L.; Diamanti, E. K.; Gengler, R. Y.; Gournis, D.; Prato, M.; Rudolf, P. *Carbon* **2013**, 61, 313-320.
45. Lomeda, J. R.; Doyle, C. D.; Kosynkin, D. V.; Hwang, W. F.; Tour, J. M. *Journal of the American Chemical Society* **2008**, 130, (48), 16201-16206.

46. Maxwell, A. J.; Bruhwiler, P. A.; Nilsson, A.; Martensson, N.; Rudolf, P. *Phys. Rev. B* **1994**, 49, (15), 10717-10725.
47. Felicissimo, M. P.; Jarzab, D.; Gorgoi, M.; Forster, M.; Scherf, U.; Scharber, M. C.; Svensson, S.; Rudolf, P.; Loi, M. A. *J. Mater. Chem.* **2009**, 19, (28), 4899-4901.

## Chapter 4

# Controlled deposition of fullerene derivatives within a graphene template by means of a modified Langmuir-Schaefer method

The scientific and technological potential of graphene includes the development of light, open 3D structures with high surface area, tunable pore size and aromatic functionalities. Towards this aim, we describe a bottom-up approach that combines self-assembly and Langmuir-Schaefer deposition for the production of fullerene-intercalated graphene hybrid materials. This method uses graphene nanosheets as templates for the attachment of two types of fullerene derivatives (bromo-fullerenes,  $C_{60}Br_{24}$  and fullerols,  $C_{60}(OH)_{24}$ ) in a bi-dimensional arrangement, allowing for perfect layer-by-layer growth with control at the molecular level. Our film preparation approach relies on a bottom-up process that includes the formation of a hybrid organo-graphene Langmuir film, which is transferred onto a substrate and then brought in contact with  $C_{60}(OH)_{24}$  molecules in solution to induce self-assembly. In the case of grafting  $C_{60}Br_{24}$  molecules into graphene a further modification of the GO platelets was performed by bringing the surface of the transferred GO Langmuir film in contact with a second amino surfactant solution (capable to interact strongly with the  $C_{60}Br_{24}$ ). By repeating these deposition cycles and thereby stacking numerous organo-graphene layers decorated with fullerene derivatives pillared structures were fabricated in thin films form. These fullerene-based hybrid thin films deposited on hydrophobic substrates were characterized by Raman and X-ray photoelectron (XPS) spectroscopies, X-ray diffraction (XRD), Atomic Force Microscopy (AFM) and contact angle measurements.

---

This chapter is based on the article: "Controlled deposition of fullerene derivatives within a graphene template by means of a modified Langmuir-Schaefer method", by A. Kouloumpis, N. Vourdas, G. Potsi, P. Zygouri, V. Kostas, N. Chalmpes, K. Spyrou, V. Stathopoulos, P. Rudolf and D. Gournis (*to be submitted*).

## 4.1 Introduction

Buckminster fullerene ( $C_{60}$ ) was discovered in 1985 by Kroto, Curl and Smalley;<sup>1</sup> it consists of 60  $sp^2$  carbon atoms arranged in pentagons and hexagons to form a spherical nanostructure (cage).<sup>2</sup> Due to the size and electronic structure of  $C_{60}$  and larger fullerenes, derivatives can be formed by inserting atoms or molecules inside the cage (endohedral fullerenes) and by functionalizing with substituents outside the cage (exohedral fullerenes). Like most organic molecular materials, fullerenes and their derivatives can be insulators, semiconductors, or even superconductors when doped with other atoms or molecules.<sup>3, 4</sup> These tunable conductivity properties render them very attractive as active materials for electronic devices, such as light detectors, transistors, or solar cells.<sup>3, 5</sup>

Although halogenated fullerene derivatives are interesting for their outstanding physical and chemical properties, investigations of their potential for diverse applications are still scarce.<sup>6-8</sup> However the presence of halogens in other carbon materials has been studied already decades ago. Doping with bromine was demonstrated to increase the electrical conductivity of graphite,<sup>9, 10</sup> and carbon nanotubes.<sup>11, 12</sup> More specifically, S. Tongay *et al.*<sup>13</sup> fabricated a superconductive bromine-intercalated graphite by exposing highly ordered pyrolytic graphite (HOPG) to bromine vapour;<sup>13</sup> with the same method N.Jung *et al.*<sup>14</sup> achieved an enhancement of the conductivity for multilayered graphene films and thick graphite. Bromine derivatives of graphene that could be used for reversible bromine storage or as a starting material for further chemical modifications were synthesized by O. Jankovsky<sup>15</sup> and co-workers in 2014. In the same year, K. Klouda *et al.*<sup>8</sup> synthesized hybrid brominated nanostructures containing fullerene molecules within graphene oxide by reacting graphene oxide with brominated fullerene derivatives ( $C_{60}Br_{14-18}$ ) and by direct bromination (with liquid bromide) of an oxidized GO- $C_{60}$  mixture. Moreover Klouda's group reported that the brominated materials thermally decomposed at higher temperatures than the unbrominated ones, due to the retarding action of bromine.<sup>8</sup> A. E. Mansour *et al.*<sup>16</sup> investigated the doping of graphene with bromine to develop high performance transparent conducting electrodes.



The functionalization of a fullerene cage can also be a first step in the synthesis of more complex derivatives with different physical and chemical properties.<sup>3, 5</sup> In this context the halogenation of fullerenes (with fluorine, chlorine, or bromine) is one of the most common chemical reaction to yield derivatives that can be either used as they are or serve as precursors in substitution reactions to sequentially attach aromatic groups to the fullerene cage.<sup>17-20</sup> In the case of brominated fullerene the substitution of the bromine with OH groups results in derivatives with better solubility in water and in aqueous solutions.<sup>21, 22</sup> Polyhydroxylated fullerenes or fullerols ( $C_{60}(OH)_n$ ), have attracted much scientific and industrial attention in engineering,<sup>23-25</sup> where they were found to improve the corrosion resistance and microhardness of coatings,<sup>23</sup> to give better mechanical properties than  $C_{60}$ , when incorporated in poly(styrene-co-4-vinylpyridine) for optical limiting performance<sup>24</sup> or to reinforce and have anti-oxidation effects when mixed with natural rubber to inhibit the decrease of tensile strength after aging.<sup>25</sup> Fullerols improve have been proposed for performing bio-oxidations.<sup>26, 27</sup> They have been tested as agents for Parkinson's disease (PD) prevention and therapy,<sup>28, 29</sup> and as active compounds in the preparation of skin rejuvenation cosmetic formulations,<sup>30</sup> just to name a few of the many fields of science and technology<sup>31-34</sup> where  $C_{60}(OH)_n$  have been considered.

Nanotechnology can tune and control the fundamental physicochemical properties of fullerenes and their derivatives by ordering them into molecular thin films<sup>35-44</sup> for the use in diverse applications including optoelectronics,<sup>45-49</sup> photovoltaics<sup>50, 51</sup> and solar cells,<sup>52-55</sup> sensors,<sup>56-58</sup> biological applications<sup>29, 59</sup> and many more.<sup>60-63</sup> The possibility to control the size and the orientation of (functionalized) fullerene molecules in 2D arrays can lead to new functional and low-dimensional materials with interesting and promising properties.

Here we report a bottom-up layer-by-layer approach for the production of fullerene-graphene oxide hybrid materials that combines the self-assembly with the Langmuir-Schaefer (LS) deposition technique. Graphene oxide nanosheets were used as a template for integrating  $C_{60}$  derivatives (fullerol with chemical formula  $C_{60}(OH)_{24}$  and bromo-fullerene with chemical formula  $C_{60}Br_{24}$ ) in 2D arrays. More specifically, a dilute water suspension of chemically oxidized graphene (GO) was used as subphase in a Langmuir-Blodgett trough and an amino surfactant, which

covalently binds to GO, was applied for the formation of hybridized GO platelets in the air-dispersion interface. After the transfer of the hybrid GO Langmuir film using the Langmuir-Schaefer method (horizontal dipping), the substrate was dipped into a solution of fullerols ( $C_{60}(OH)_{24}$ ) to induce self-assembly (SA). Instead, in the case of grafting  $C_{60}Br_{24}$ , after the transfer of the hybrid GO Langmuir film using the Langmuir-Schaefer method (horizontal dipping), the substrate was first brought in contact with another amino surfactant solution to induce functionalization by self-assembly and then, as the final step, lowered in the solution of the bromo-fullerene to complete the self-assembly with the  $C_{60}Br_{24}$  molecules. Hybrid graphene oxide multilayer thin films hosting fullerene-derivatives molecules within their interlayer space were fabricated by repeating these two procedures, as illustrated in Scheme 4.1. The samples were characterized by Raman and X-ray photoelectron spectroscopies, X-ray diffraction, Atomic Force Microscopy and contact angle measurements.

## **4.2 Experimental Section**

### **4.2.1 Materials**

Buckminster fullerene (99.8%), octadecylamine (ODA,  $\geq 99\%$ ), hexamethylenediamine (HEX,  $\geq 99\%$ ), acetone, methanol and ethanol were purchased from Sigma-Aldrich. Sodium hydroxide (NaOH) pellets were obtained from Vioryl. Ultrapure deionized water (18.2 M $\Omega$ ) produced by a Millipore Simplicity® system was used throughout. The Si wafers (P/Bor, single side polished, purchased from Si-Mat) used as substrates were cleaned prior to use by ultrasonication in water, acetone and ethanol for 15 min each. All reagents were of analytical grade and were used without further purification.

### **4.2.2 Synthesis of Graphene Oxide**

Graphene oxide (GO) was synthesized using a modified Staudenmaier method, as described in Chapter 3 (see section 3.2.2).

### 4.2.3 Synthesis of fullerene derivatives<sup>1</sup>

In a typical synthesis of polybrominated fullerene<sup>22</sup> ( $C_{60}Br_{24}$ ), 300 mg of Buckminster fullerene were dissolved in 2 mL of elementary bromine, in the presence of a catalytic quantity of  $FeBr_3$ . The mixture was stirred for 40 min at room temperature. When the reaction was completed, the excess of unreacted bromine was evaporated and the catalyst was separated by dissolving in a mixture of ethanol/ $H_2O$  (1:2, v/v).

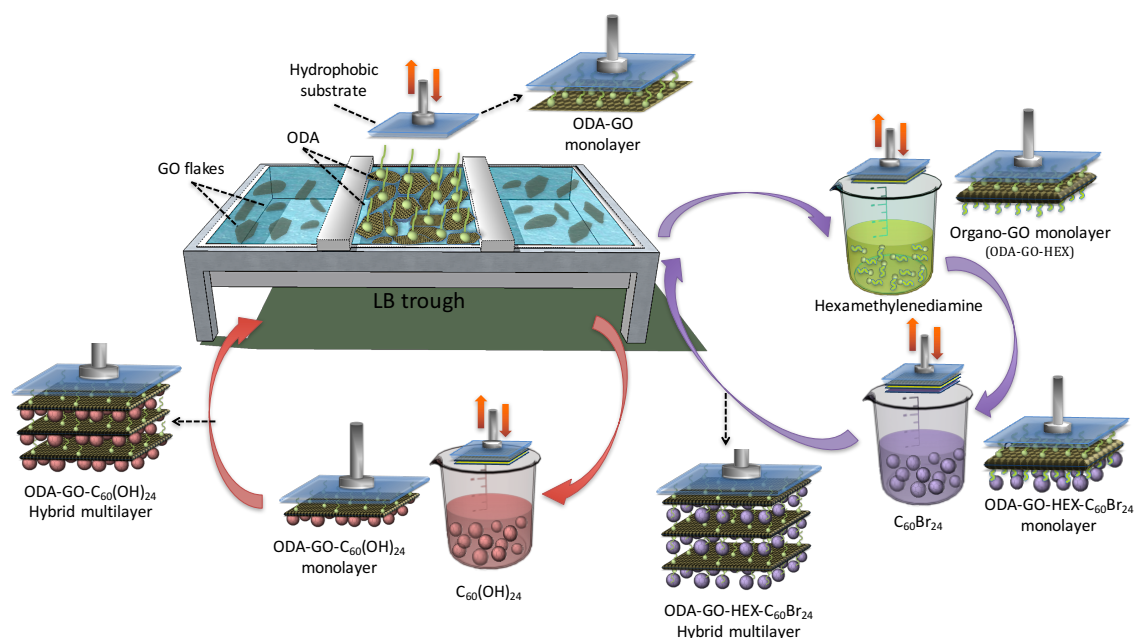
Polyhydroxylated fullerene (fullerol,  $C_{60}(OH)_{24}$ ) was synthesized by using polybrominated fullerenes as precursor.<sup>22</sup> More specifically, fullerol was obtained by reacting 50 mg of  $C_{60}Br_{24}$  with 5 mL of NaOH 2 M (pH = 13) for 2 h at room temperature. After completion of the reaction, the solvent was evaporated at 40 °C; then the mixture was filtered and washed 5 times with 10 mL of ethanol (purity 70 %). The dark brown powder product obtained after the filtration was soluble in polar solvents like water.<sup>22</sup>

### 4.2.4 Preparation of hybrid multilayers of graphene oxide and $C_{60}$ -derivatives

A Langmuir Blodgett (LB) trough (KSV 2000 Nima Technology) was cleaned with ethanol and distilled-deionized water. GO suspensions in ultrapure water ( $0.02 \text{ mg mL}^{-1}$ ) were prepared and used as subphase. To achieve the hybridization of the GO sheets in the LB trough, 200  $\mu\text{L}$  of a  $0.2 \text{ mg mL}^{-1}$  ODA dissolved in a chloroform/methanol mixture (9/1, v/v) were spread onto the water surface using a microsyringe. After a waiting time of 20 min to allow for solvent evaporation and GO-surfactant functionalization to occur, the hybrid ODA-GO layer was compressed at a rate of  $5 \text{ mm min}^{-1}$  until the chosen stabilization pressure of  $20 \text{ mN m}^{-1}$  was reached. This pressure was maintained throughout the deposition process. The hybrid Langmuir layers (ODA-GO) were transferred onto the Si-wafer substrates by horizontal dipping (Langmuir Schaefer technique), with downward and lifting speeds of  $10$  and  $5 \text{ mm min}^{-1}$ , respectively.<sup>44, 64</sup>

---

<sup>1</sup> Fullerene derivatives samples were provided by Dr. Panagiota Zygouri (University of Ioannina, Greece)



**Scheme 4.1.** Schematic representation of the synthetic procedures for fabricating the hybrid films of left: graphene oxide and  $C_{60}(OH)_{24}$  (ODA-GO- $C_{60}(OH)_{24}$ ) or right: graphene oxide and  $C_{60}Br_{24}$  (ODA-GO-HEX- $C_{60}Br_{24}$ ). Both procedures consist in a Langmuir Schaefer deposition combined with with one self-assembly step (left) or two self-assembly steps (right)

After the horizontal lift of a substrate, the ODA-GO film was dipped into an aqueous solution of fullerols ( $0.2 \text{ mg mL}^{-1}$ ). A hybrid graphene/ $C_{60}(OH)_{24}$  multilayer film was constructed by repeating this procedure for 60 times, as shown in Scheme 4.1 (sample denoted as ODA-GO- $C_{60}(OH)_{24}$ ). For the formation of the hybrid graphene oxide film hosting polybrominated fullerene in its interlayer space, a further surface modification of the GO nanosheets was performed by bringing the surface of the transferred Langmuir film (ODA-GO) in contact with a amino surfactant, HEX dissolved in methanol ( $0.2 \text{ mg mL}^{-1}$ ) and making use of a self-assembly step.<sup>44, 65</sup> After this functionalization, in a final stage, the hybrid organo-GO (ODA-GO-HEX) film was lowered into a solution of polybrominated fullerene ( $0.2 \text{ mg mL}^{-1}$ ) dissolved in a ethanol/ $H_2O$  mixture (2/1, v/v) to induce the formation of a hybrid ODA-GO-HEX- $C_{60}Br_{24}$  layer by self-assembly. By repeating this procedure 60 times, a hybrid multilayer film was constructed as shown in Scheme 4.1 (sample denoted as ODA-GO-HEX- $C_{60}Br_{24}$ ). Each time when the substrate was lowered, it was allowed to

touch the air-water interface or the solution surface in a very gentle dip of max 0.5 mm below the liquid surface for 90 s. After each deposition step samples were rinsed several times by dipping into ultrapure water (to eliminate any weakly attached cations or molecules that remained from the deposition steps) and dried with nitrogen flow (to avoid contaminating either the LB air-water interface or the other solutions).<sup>41, 44, 66</sup>

## 4.3 Results-discussion

### 4.3.1 Structural characterization of C<sub>60</sub> derivatives<sup>2</sup>

FTIR spectra of polybrominated fullerene (C<sub>60</sub>Br<sub>24</sub>) and fullerol (C<sub>60</sub>(OH)<sub>24</sub>) are shown in Figure 4.1. In the case of polybrominated fullerene, the stretching vibrations of the C-Br groups were observed in the range of 500-610 cm<sup>-1</sup> (515 cm<sup>-1</sup>, 545 cm<sup>-1</sup> and 609 cm<sup>-1</sup>).<sup>67</sup> Based on the Sadtler Handbook of Infrared spectra<sup>68</sup> bands in the region of 1000-1200 cm<sup>-1</sup> can be attributed to vibrations of C-Br groups; for C<sub>60</sub>Br<sub>24</sub>, these bands appear at 1045 cm<sup>-1</sup>, 1086 cm<sup>-1</sup>, 1144 cm<sup>-1</sup>, 1180 cm<sup>-1</sup>.

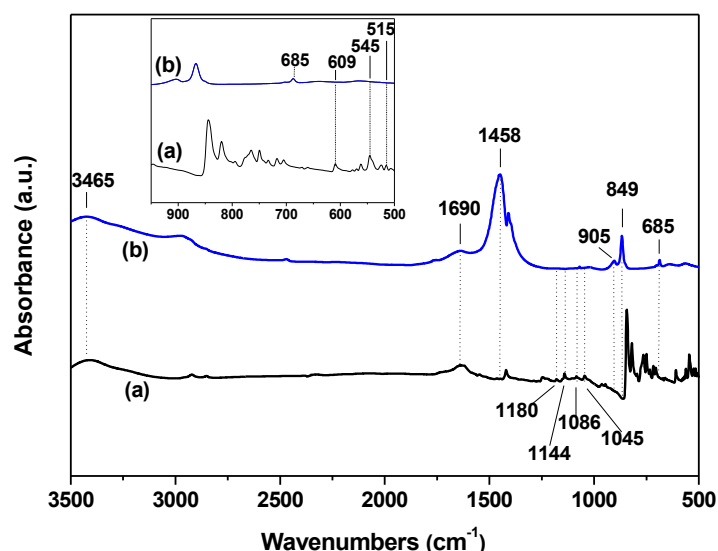


**Figure 4.1:** FTIR spectra of (a) polybrominated fullerene (C<sub>60</sub>Br<sub>24</sub>) and (b) fullerol (C<sub>60</sub>(OH)<sub>24</sub>).

<sup>2</sup> The structural characterization of fullerene derivatives samples was provided by Dr. Panagiota Zygouri (University of Ioannina, Greece)

The spectrum of  $C_{60}(OH)_{24}$  shows characteristic bands due to the presence of hydroxyl groups at  $1065$  and  $1458\text{ cm}^{-1}$  (bending vibrations of C–OH groups), as well as at  $685\text{ cm}^{-1}$ ,  $849\text{ cm}^{-1}$  and  $905\text{ cm}^{-1}$  (wagging vibrations of OH). The bands at  $3465\text{ cm}^{-1}$  (stretching vibration) and  $1690\text{ cm}^{-1}$  (bending vibration) are instead indicative of the presence of water molecules. The band at  $3465\text{ cm}^{-1}$  corresponds to the stretching vibration of the -OH bond and is observed also in liquid water.<sup>69</sup>

Raman spectra of pristine and polybrominated fullerene ( $C_{60}Br_{24}$ ) are shown in Figure 4.2.  $C_{60}$  is characterized by high  $I_h$  symmetry and presents 46 vibrational modes distributed over the 174 vibrational degrees of freedom. From the 46 vibrational modes,  $4(T_{1u})$  are active in the infrared region and 10 ( $2A_g + 8H_g$ ) are active in Raman, while the remaining are optically inactive.<sup>70</sup>

$$\Gamma_{\text{vib}}(C_{60}) = 2A_g(\text{Raman}) + 3F_{1g} + 4F_{2g} + 6G_g + 8H_g(\text{Raman}) + A_u + 4F_{1u}(\text{IR}) + 5F_{2u} + 6G_u + 7H_u$$

In the case of polybrominated fullerene, the bromines are attached to the twelve six-membered rings of the fullerene structure at the 1 and 4 position induce a “boat” conformation, while for the remaining 8 six-membered rings, the bromine atoms bound to the carbons 1, 3 and 5, create a “chair” conformation.<sup>71</sup> The active vibrations of the C-Br groups are five, more specifically stretching vibrations of these groups are observed at  $505\text{ cm}^{-1}$ ,  $516\text{ cm}^{-1}$ ,  $549\text{ cm}^{-1}$ ,  $562\text{ cm}^{-1}$  and  $585\text{ cm}^{-1}$ .

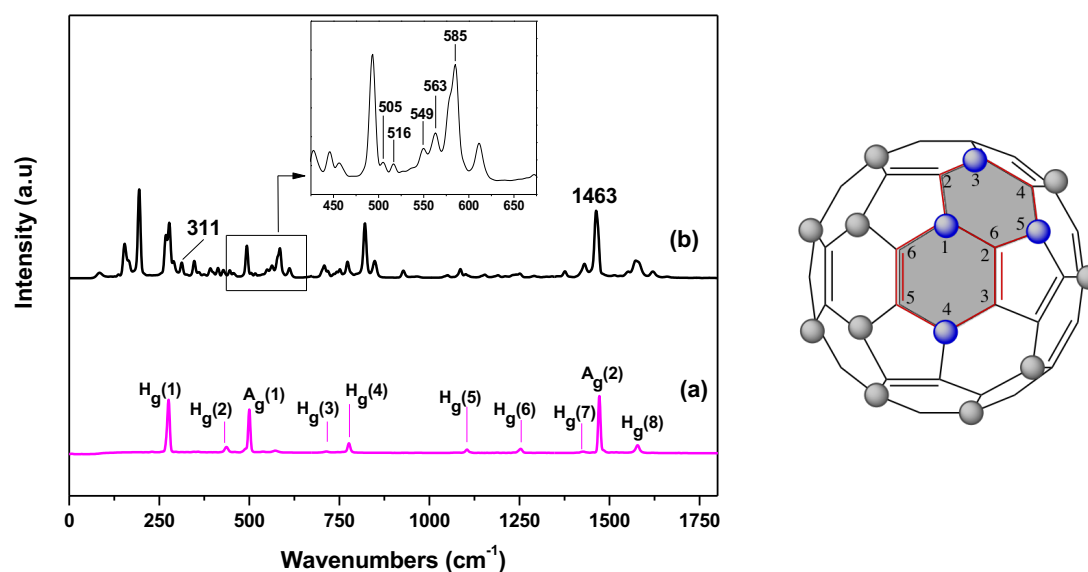


**Figure 4.2:** Left: Raman spectra of (a) Pristine Buckminster fullerene and (b) polybrominated fullerene ( $C_{60}Br_{24}$ ). Right: typical structure of  $C_{60}Br_{24}$ .

The presence of the band at  $1463\text{ cm}^{-1}$  in the spectra of the  $\text{C}_{60}\text{Br}_{24}$ , which is due to the  $\text{Ag}$  symmetry of the fullerene, indicates that the icosahedral structure remains unaffected after the functionalization (Figure 4.2 right). The appearance of a new band at  $308\text{ cm}^{-1}$  can be attributed to a neutral molecular  $\text{Br}_2$  in a charge transfer complex between  $\text{C}_{60}$  and  $\text{Br}_2$ . The absence of any  $\nu_{\text{Br-Br}}$  signal renders the  $\text{C}_{60}\text{Br}_{24}$  a real derivative of fullerene.<sup>72, 73</sup>

Thermogravimetric analysis (TGA) and thermal analysis (DTA) measurements for polybrominated and polyhydroxylated fullerene are presented in Figure 4.3. The TGA curve of  $\text{C}_{60}\text{Br}_{24}$  (a) presents a 9% weight loss up to  $100\text{ }^\circ\text{C}$  corresponding to absorbed water and unreacted molecular bromine ( $\text{Br}_2$ ). At the temperature range between  $100$  and  $180\text{ }^\circ\text{C}$ , a mass loss ( $\sim 31\%$ ) is observed, which can be attributed to the removal of functional groups. The curve of DTA shows an exothermic peak at  $430\text{ }^\circ\text{C}$  related to the combustion of the fullerene carbon cage, which is followed by the total weight loss of the sample ( $\sim 60\text{ wt}\%$ ). In the case of fullerols (b), a mass loss of  $\sim 20\text{ wt}\%$  in the temperature range up to  $120\text{ }^\circ\text{C}$ , points to the presence of naturally absorbed water molecules and demonstrates the hydrophilic character of the  $\text{C}_{60}(\text{OH})_{24}$ . The removal of the hydroxyl groups occurs between  $150$  and  $320\text{ }^\circ\text{C}$  and corresponds to a weight loss of  $\sim 13\%$ .

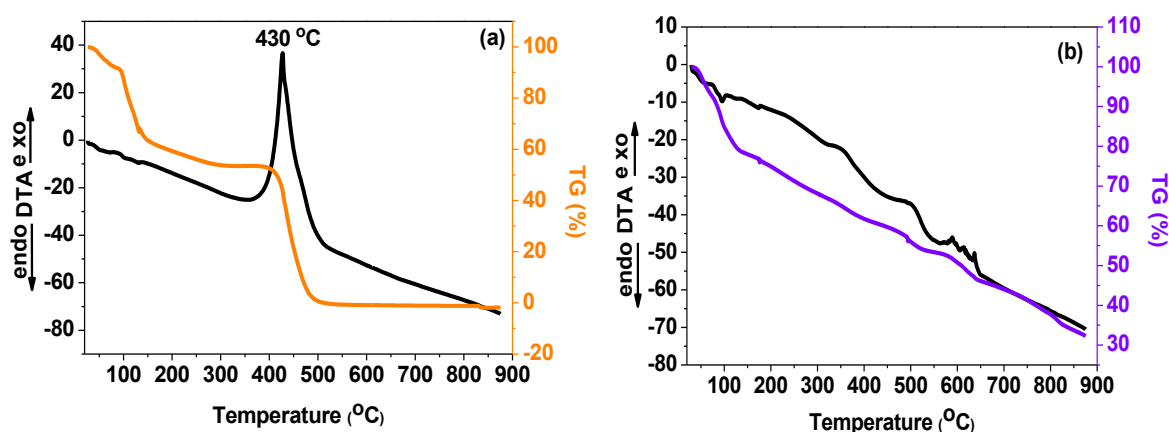


**Figure 4.3:** Thermogravimetric analysis (TGA) and thermal analysis (DTA) measurements of (a) polybrominated ( $\text{C}_{60}\text{Br}_{24}$ ) and (b) polyhydroxylated fullerenes ( $\text{C}_{60}(\text{OH})_{24}$ ).

Above 350 °C the decomposition of the graphitic lattice resulting in a weight loss close to 37%. The removal of the hydroxyl groups and the decomposition of the fullerene are not separated in the DTA curve, indicating an interdependence of these two phenomena and consequently testifying to the successful chemical functionalization of the fullerene.

### 4.3.2 Structural control of hybrid monolayers

To demonstrate the attachment of ODA to the GO flakes, we recorded the surface pressure-molecular area ( $\pi$ -A) isotherms while compressing the Langmuir film by means of the movable barriers of the LB trough. Figure 4.4 displays the  $\pi$ -A isotherms of an ODA monolayer on pure water and on a GO dispersion. The curves show changes in slope corresponding to the phase transitions from two dimensional gas to condensed liquid and then to solid during the compression process. The fact that the compression of ODA on the GO suspension gives rise to an increase of the surface pressure much earlier during the compression that for ODA on pure water, indicates that GO has hybridized by covalent bonding via the amide functionality of ODA and a hybrid floating layer of ODA-GO has been formed.<sup>44</sup>

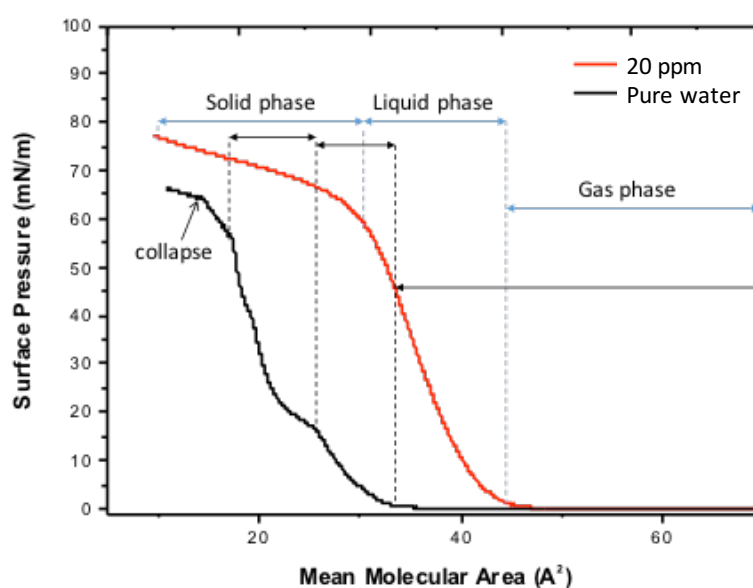


**Figure 4.4.**  $\pi$ -A isotherms recorded during the compression of ODA monolayers on pure water and on an aqueous dispersion of 20 ppm GO.



Representative AFM images of hybrid Langmuir monolayers (ODA-GO) transferred onto the Si-wafer at different surface pressures in the LB trough, namely 5, 10, 15 and 20 mN/m, are shown in Figure 4.5. The topographic images revealed that the substrate surface coverage of the hybrid ODA-GO monolayers is higher as the surface pressure increases. GO nanosheets with well-defined edges are easily observed in the AFM micrographs, verifying the formation of a hybrid Langmuir film at the air-dispersion interface. More specifically, when the Langmuir film was compressed at 5 mN m<sup>-1</sup> (Figure 4.5a), the GO platelets appear isolated with an empty space between them. When the Langmuir film was further compressed at 10 mN m<sup>-1</sup> (Figure 4.5b), the GO platelets contact each other, with still rather large voids between them and at even higher surface pressure of 15 mN m<sup>-1</sup> (Figure 4.5c), the nanosheets become more closely packed.

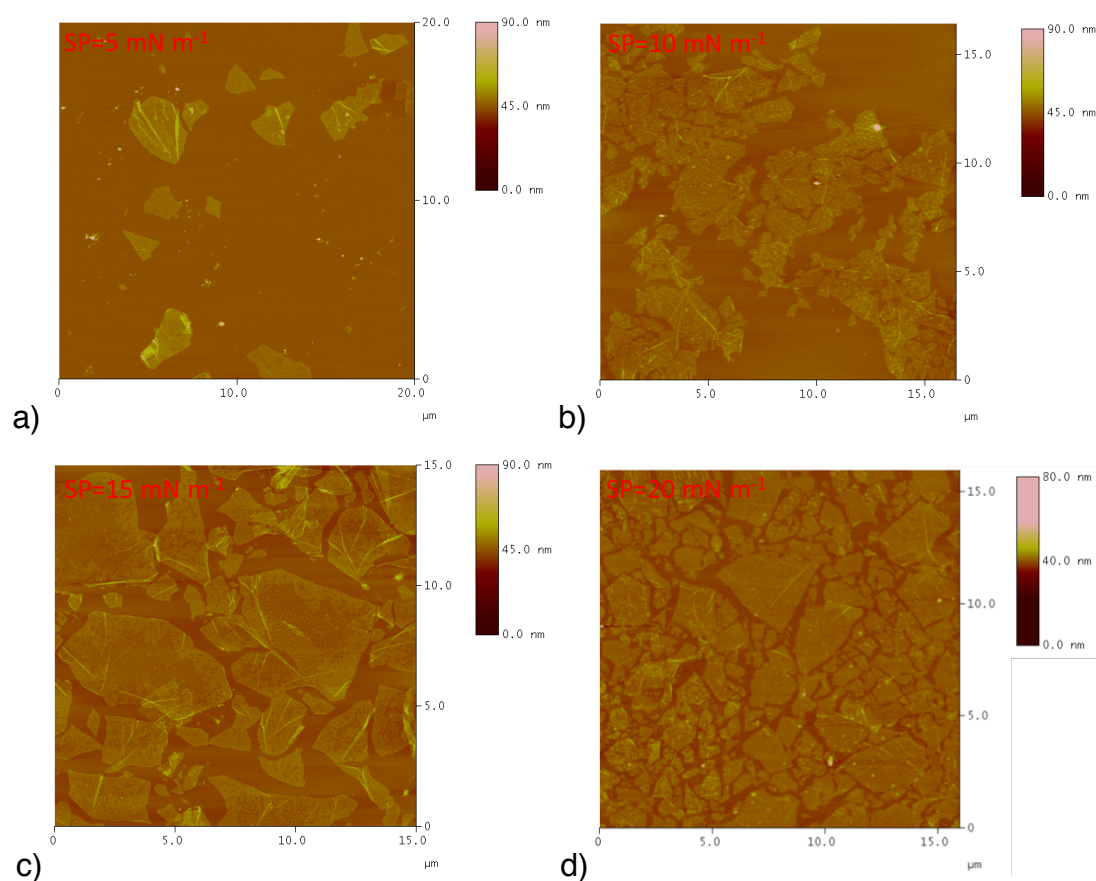


**Figure 4.5.** AFM height images of ODA-GO monolayers deposited on Si-wafer substrates at different surface pressures of a) 5 mN m<sup>-1</sup>, b) 10 mN m<sup>-1</sup>, c) 15 mN m<sup>-1</sup> and d) 20 mN m<sup>-1</sup> during the compression process.

When deposited at  $20 \text{ mN m}^{-1}$  the hybrid film becomes very dense but with only very few overlaps between adjacent flakes (Figure 4.5d). Furthermore, the GO layers exhibit wrinkles that may be related to water-GO interaction and are formed during dipping and drying. GO sheets can become wrinkled during water evaporation due to surface tension.<sup>74, 75</sup> The average thickness of the flakes is  $1\text{-}1.5 \pm 0.2 \text{ nm}$  as derived from topographical height profile (section analysis) corresponding to the size of single graphene oxide layers, which is  $6.1 \text{ \AA}$ .<sup>76 44</sup>

Detailed AFM images of single ODA-GO-HEX- $\text{C}_{60}\text{Br}_{24}$  and ODA-GO- $\text{C}_{60}(\text{OH})_{24}$  hybrid layers deposited on Si-wafer are shown in Figure 4.6. The micrographs reveal the presence of quite uniform and nearly spherical particles decorating several micrometer size layers indicating the successful attachment of the  $\text{C}_{60}$  derivatives on the graphene oxide surface. More specifically, the  $\text{C}_{60}\text{Br}_{24}$  decoration in the hybrid ODA-GO-HEX monolayer is relatively uniform revealing small particles in all over the surface of the GO sheets while wrinkled sheets were also observed.

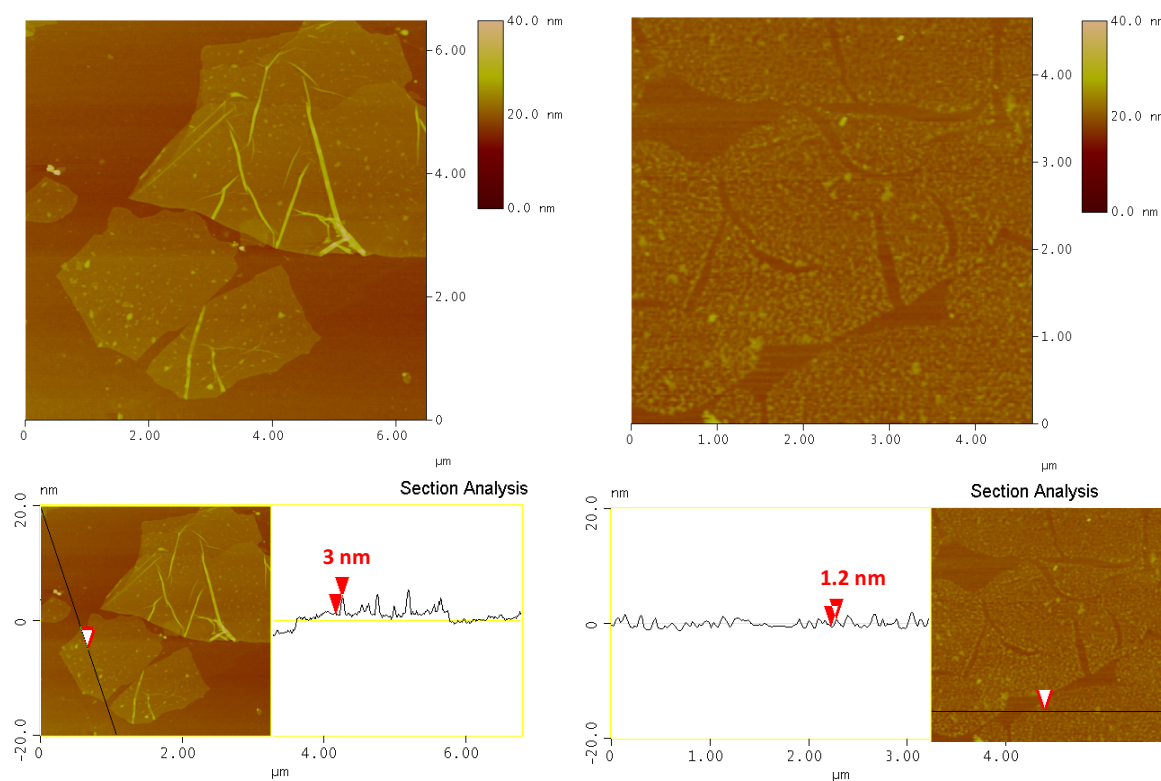


**Figure 4.6.** AFM height images and cross section analysis profile of ODA-GO-HEX- $\text{C}_{60}\text{Br}_{24}$  (left) and ODA-GO- $\text{C}_{60}(\text{OH})_{24}$  (right) hybrid single layers.

In the other hand, the hybrid ODA-GO-C<sub>60</sub>(OH)<sub>24</sub> layer exhibit a smoother distribution and higher coverage of C<sub>60</sub>(OH)<sub>24</sub> molecules on the graphene oxide layers as compared to C<sub>60</sub>Br<sub>24</sub> in the hybrid ODA-GO-HEX-C<sub>60</sub>Br<sub>24</sub> layer. This different morphology is due to the direct attachment of C<sub>60</sub>(OH)<sub>24</sub> to the polar oxygen-containing groups homogeneously distributed on the graphitic surface (without interposed surfactant like in the case of brominated fullerene). The average size of decorating C<sub>60</sub>Br<sub>24</sub> and C<sub>60</sub>(OH)<sub>24</sub> molecules was about 3±0.2 nm and 1.8±0.2 nm respectively as deduced from the height profile analysis. The larger size of the C<sub>60</sub>Br<sub>24</sub> moieties arises probably from the presence of the adsorbed HEX molecules attached to C<sub>60</sub>Br<sub>24</sub>.

### 4.3.3 Characterization of graphene/C<sub>60</sub>-derivative hybrid multilayers

The X-ray diffraction patterns of the produced ODA-GO-HEX-C<sub>60</sub>Br<sub>24</sub> and ODA-GO-C<sub>60</sub>(OH)<sub>24</sub> hybrid multilayers (60 layers) are shown in Figure 4.7. The hybrid multilayer with C<sub>60</sub>Br<sub>24</sub> shows a 001 diffraction peak at 2θ=2.3° from which a d<sub>001</sub>-spacing of 38.4 Å is deduced.

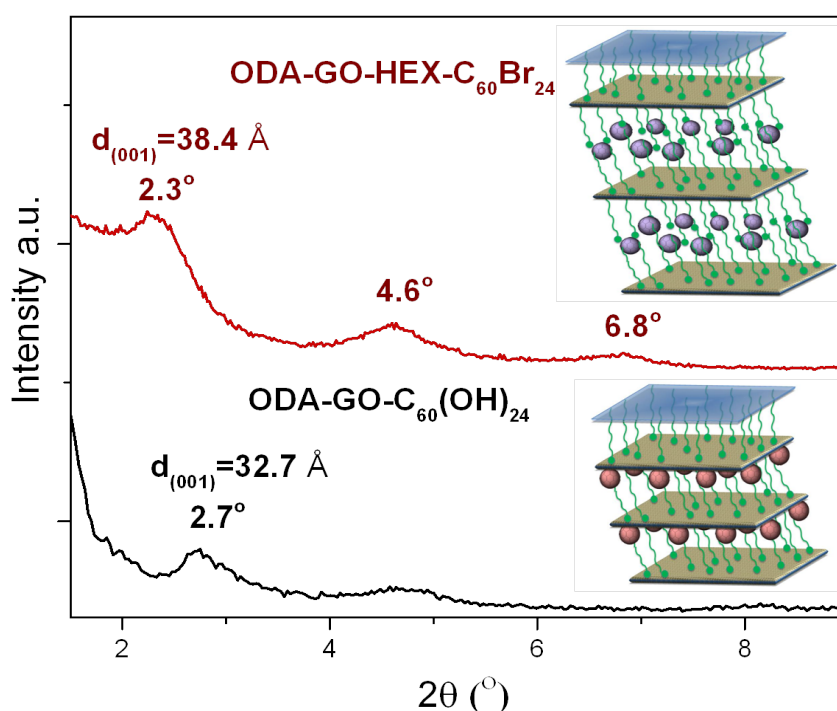


**Figure 4.7.** XRD patterns and schematic illustration (inset) of ODA-GO-HEX-C<sub>60</sub>Br<sub>24</sub> and ODA-GO-C<sub>60</sub>(OH)<sub>24</sub> hybrid multilayers (60 layers).

This  $d_{001}$  value corresponds to an interlayer space of  $\Delta = 38.4 - 6.1 = 32.3 \text{ \AA}$ , where the value of  $6.1 \text{ \AA}$  represents the thickness of the GO single layer,<sup>76</sup> indicating the successful insertion of the  $C_{60}Br_{24}$  molecules as pillars between GO sheets. Moreover, the presence of higher order (00l) reflections in the XRD pattern of ODA-GO-HEX- $C_{60}Br_{24}$  suggests very high order in the stacking of the GO layers. On the other hand, the ODA-GO- $C_{60}(OH)_{24}$  hybrid multilayer shows a 001 diffraction peak at  $2\theta = 2.7^\circ$ , resulting in a smaller  $d_{001}$ -spacing of  $32.7 \text{ \AA}$ . This value corresponds to an interlayer space of  $\Delta = 32.7 - 6.1 = 26.6 \text{ \AA}$ , testifying to the presence of  $C_{60}(OH)_{24}$  molecules in the interlayer space.<sup>77</sup> This value is smaller as compared to the  $d_{001}$ -spacing of ODA-GO-HEX- $C_{60}Br_{24}$  because the  $C_{60}(OH)_{24}$  molecules are directly attached to the graphene oxide layers without an interposed surfactant.

The Raman spectra of the produced ODA-GO-HEX- $C_{60}Br_{24}$  and ODA-GO- $C_{60}(OH)_{24}$  hybrid multilayers deposited on a Si wafer are shown in Figure 4.8. Spectra of graphene-based thin films exhibit the characteristic bands. The second order D band at around  $1350 \text{ cm}^{-1}$  that is connected to  $sp^3$  hybridized carbon arising from lattice defects and distortions while the first order G band at around  $1600 \text{ cm}^{-1}$  is linked with  $sp^2$  hybridized carbon atoms of the graphitic lattice.<sup>78, 79</sup>

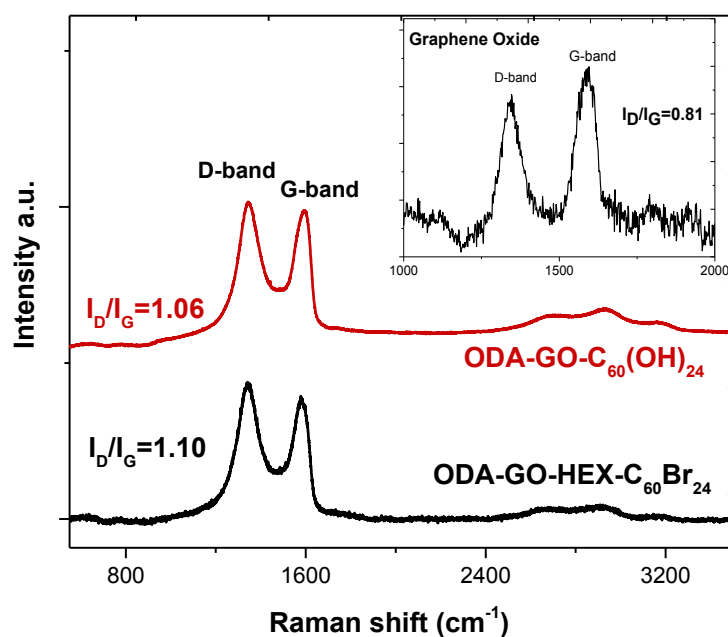


**Figure 4.8.** Raman spectra of ODA-GO-HEX- $C_{60}Br_{24}$  and ODA-GO- $C_{60}(OH)_{24}$  hybrid multilayers (inset: Raman spectrum of graphene oxide).

The ratio of the D- to G-band intensities ( $I_D/I_G$ ) is indicative of the quality of the graphitic lattice and was found to be 0.81 for the pristine GO (Figure 4.8, inset). The ratio of the D- to G-band intensities ( $I_D/I_G$ ) for the hybrids ODA-GO-HEX-C<sub>60</sub>Br<sub>24</sub> and ODA-GO-C<sub>60</sub>(OH)<sub>24</sub> multilayers is at least 1.1 and 1.06 respectively. This increase of the  $I_D/I_G$  ratio in the case of the hybrid films could be assigned to the relative increase of the D' band (1620 cm<sup>-1</sup>), which exceeds the intensity of the G band<sup>80</sup> suggesting the hybridization of GO due to the covalent bonding of the amide functionality of ODA. Moreover, both spectra display three broad bands in the 2D region at ~2700, ~2930 and ~3200 cm<sup>-1</sup>, which are typical of GO materials. These are related with the 2D (or else G') vibrational mode, the D+D' mode and the 2D' mode in that order.<sup>78, 79, 81, 82</sup>

In order to gain further information for the type of bonding between the graphene oxide layers and the C<sub>60</sub> derivatives we employed X-Ray photoelectron spectroscopy measurements. Figure 4.9 displays the C1s and N1s core level regions of the ODA-GO-C<sub>60</sub>(OH)<sub>24</sub> hybrid multilayer. Four contributions located at binding energies of 284.6 eV, 286.1 eV, 287.2 eV and 288.6 eV can be identified. The peak at 284.6, which accounts for 61.1% of the total carbon intensity, originates from the carbon-carbon bonds of graphene oxide and of the fullerene cage, as well the C-C of ODA. The peak at 286.1 eV is due to C-O of GO and of the hydroxyl groups of fullerol. The same peak also contains contributions from C-N bonds of ODA molecules when reacted with the epoxy groups of graphene oxide. The contribution at 287.2 eV is due to C=O (carbonyl) as well C-O-C (epoxy) functional groups and accounts for 10.7 % of the total carbon intensity. A last peak centred at 288.6 eV stems from carboxyl groups of graphene oxide (3.1%). Additionally there is no characteristic shake up peaks of C<sub>60</sub><sup>83</sup> are observed because the  $\pi$  electrons are no longer delocalized over the whole molecule.<sup>84, 85</sup>

In the Nitrogen 1s photoelectron spectra we identify three contributions, one at 399.3 eV attributed to C-N-C bond of ODA with the epoxy groups of graphene oxide, a second one at 400.8 eV corresponding to the primary amines that may interact with the GO surface by non-covalent bonding and a third one, which originates from the protonated amines of ODA-GO-C<sub>60</sub>(OH)<sub>24</sub>.

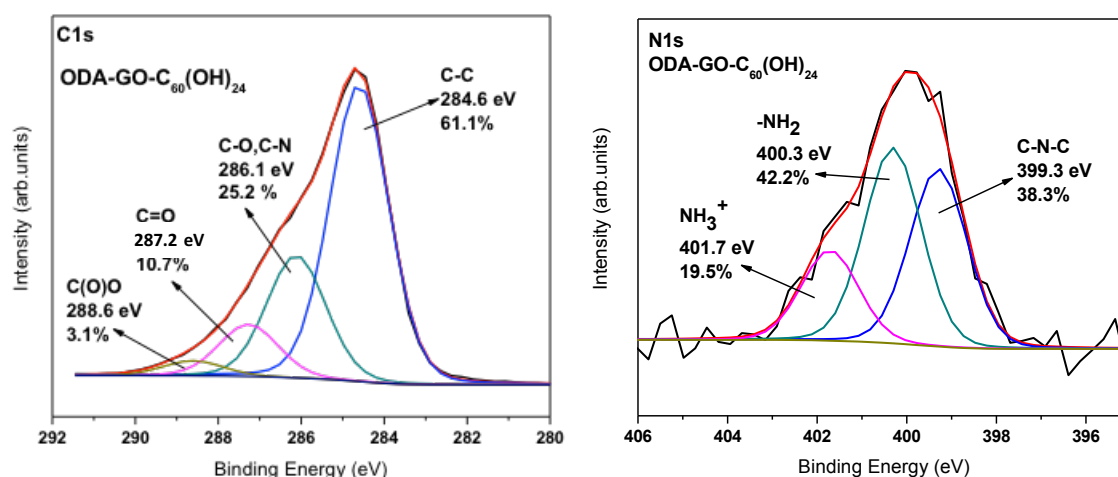


**Figure 4.9.** C1s (left) and N1s (right) core level photoemission spectra of a ODA-GO-C<sub>60</sub>(OH)<sub>24</sub> hybrid multilayer film.

Figure 4.10 shows the C1s and N1s photoemission spectra of the ODA-GO-HEX-C<sub>60</sub>Br<sub>24</sub> hybrid multilayer. The main contribution to the C1s line at 284.6 eV binding energy results from carbon-carbon bonds of graphene oxide and of the fullerene cage, as well as from the C-C bonds of ODA and accounts for 57.4% of the total carbon intensity.

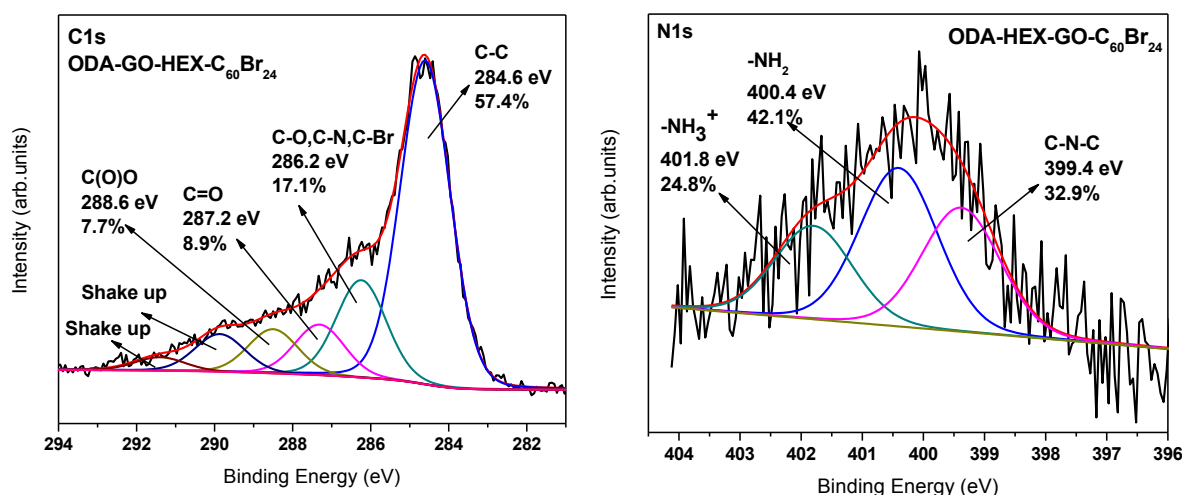


**Figure 4.10.** C1s (left) and N1s (right) core level photoemission spectra of the ODA-GO-HEX-C<sub>60</sub>Br<sub>24</sub> hybrid multilayer film.

A less intense peak (17.1%) arises from the C-O of GO and the C-Br bond of fullerene derivative and contains also contributions from C-N bonds of ODA molecules due to the chemical grafting of the amino groups of ODA with the epoxy groups of GO. The contribution at 287.2 eV is due to the C=O (carbonyl) as well C-O-C (epoxy) functional groups and accounts for 8.9 % of the total carbon intensity while the presence of carboxyl groups is demonstrated from the peak located at 288.6 eV (7.7%). The additional peaks at 290.0 eV and 291.5 eV in the ODA-GO-HEX-C<sub>60</sub>Br<sub>24</sub> spectrum are due to C1s shake up features of C<sub>60</sub><sup>86, 87</sup> resulting from  $\pi$ - $\pi^*$  transitions excited in the photoemission process and therefore gives proof to the presence of fullerene derivatives in the hybrid multilayer.

In the Nitrogen 1s photoelectron spectrum of ODA-GO-HEX-C<sub>60</sub>Br<sub>24</sub> we identify three contributions like in the case of ODA-GO-C<sub>60</sub>(OH)<sub>24</sub>, one at 399.4 eV attributed to C-N-C bond of ODA and/or HEX molecules with the epoxy groups of graphene oxide, a second one at 400.8 eV corresponding to the primary amines that may interact with the GO surface by non-covalent bonding or physisorb to the graphene surface unreacted and a third one, which derives from the protonated amines of ODA-GO-HEX-C<sub>60</sub>Br<sub>24</sub> system. Furthermore we observe an increase of the NH<sub>3</sub><sup>+</sup> amines for ODA-GO-HEX-C<sub>60</sub>Br<sub>24</sub>, implying that a higher percentage of NH<sub>3</sub><sup>+</sup> amines interacts electrostatically with the graphene surface; this results in a lower C-N-C peak (32.9 % of the total N1s intensity) as compared to the C-N-C peak (38.3 % of the total N1s intensity) of the ODA-GO-C<sub>60</sub>(OH)<sub>24</sub> hybrid film.

Water contact angle (CA) measurements are presented in Table 4.1. The CA for the ODA-GO-C<sub>60</sub>(OH)<sub>24</sub> hybrid multilayer film results systematically higher than that of the ODA-GO-C<sub>60</sub>Br<sub>24</sub> hybrid multilayer film, with the first exhibiting CA=85° and the latter CA=55°, ca. 1 min after the droplet touches the surfaces. Both advancing and receding CA are higher for the ODA-GO-C<sub>60</sub>(OH)<sub>24</sub> system.

Despite the fact that C<sub>60</sub>(OH)<sub>24</sub> molecules are considered to be more hydrophilic than of C<sub>60</sub>Br<sub>24</sub> due to the -OH functional groups, our CA results revealed that the ODA-GO-C<sub>60</sub>(OH)<sub>24</sub> hybrid system exhibits a more hydrophobic character than ODA-GO-HEX-C<sub>60</sub>Br<sub>24</sub>.

**Table 4.1.** Water contact angle measurements

Sample	CA (t=0)	CA (t=1min)	Advancing CA	Receding CA
ODA-GO-HEX-C <sub>60</sub> Br <sub>24</sub> (30 layers)	59±1°	55±1°	64±1°	<20±1°
ODA-GO-C <sub>60</sub> (OH) <sub>24</sub> (30 layers)	98±1°	85±1°	103±1°	40±1°

This difference can be attributed to the different synthesized nanostructures. Microscopy studies revealed that the distribution of the grafted C<sub>60</sub>(OH)<sub>24</sub> molecules on the graphene oxide layer is more dense and homogeneous comparing the ODA-GO-HEX-C<sub>60</sub>Br<sub>24</sub> hybrid multilayer, resulting in a different morphology. Moreover the hydrophilic behaviour of the ODA-GO-HEX-C<sub>60</sub>Br<sub>24</sub> film, compared to the more hydrophobic behaviour of the ODA-GO-C<sub>60</sub>(OH)<sub>24</sub> is corroborated by the XPS data discussed above. As was observed from Fig. 4.9 and Fig. 4.10 the contributions of the hydrophilic C(O)O (7.7% of the total C1s intensity) and NH<sub>3</sub><sup>+</sup> (24.8% of the total N1s intensity) groups for ODA-GO-HEX-C<sub>60</sub>Br<sub>24</sub>, are more dominant than the corresponding ones for ODA-GO-C<sub>60</sub>(OH)<sub>24</sub> (3.1% of the total C1s intensity and 19.5% of the total N1s intensity), while the contribution due to aliphatic/hydrophobic carbon bonds (C-C) is higher for ODA-GO-C<sub>60</sub>(OH)<sub>24</sub> (61.1% of the total C1s intensity) than for ODA-GO-HEX-C<sub>60</sub>Br<sub>24</sub> (57.4% of the total C1s intensity).

## 4.4 Conclusions

C<sub>60</sub>(OH)<sub>24</sub> and C<sub>60</sub>Br<sub>24</sub> fullerene derivatives were effectively inserted between graphene oxide layers through a layer-by-layer synthetic approach, which combines Langmuir-Schaefer deposition and self-assembly steps. The effectiveness of this method in terms of coverage, uniformity and single-layer level control of the assembly was confirmed by  $\pi$ -A isotherms and AFM measurements. X-ray diffraction measurements revealed the successful insertion of C<sub>60</sub>Br<sub>24</sub> and C<sub>60</sub>(OH)<sub>24</sub> molecules



between the graphene oxide nanosheets resulting in hybrid multilayer structures. The existence of  $C_{60}(OH)_{24}$  and  $C_{60}Br_{24}$  in the hybrid system was revealed by X-ray photoelectron spectroscopy, while Raman spectroscopy showed that the insertion of the fullerene derivatives between the graphene oxide nanosheets caused an increase of the  $I_D/I_G$  ratio, confirming the covalent bonding of the amide functionality of ODA to GO. Corroborating the XPS results, contact angle measurements revealed that the hybrid film of graphene oxide and  $C_{60}(OH)_{24}$  exhibits a more hydrophobic character, while the hybrid film of graphene oxide and  $C_{60}Br_{24}$  is more hydrophilic, suggesting that the hydrophobicity doesn't depend on the functional groups of the pristine nanomaterials but on the morphology of the hybrid systems. These novel fullerene-based hybrid films could be candidate nanomaterials for potential applications in photovoltaics, sensors, or optoelectronic devices as well as in photocatalysis and drug delivery.

## 4.5 References

1. Kroto, H. W.; Heath, J. R.; O'Brien, S. C.; Curl, R. F.; Smalley, R. E. *Nature* **1985**, 318, (6042), 162-163.
2. David, W. I. F.; Ibberson, R. M.; Matthewman, J. C.; Prassides, K.; Dennis, T. J. S.; Hare, J. P.; Kroto, H. W.; Taylor, R.; Walton, D. R. M. *Nature* **1991**, 353, (6340), 147-149.
3. Georgakilas, V.; Perman, J. A.; Tucek, J.; Zboril, R. *Chemical Reviews* **2015**, 115, (11), 4744-4822.
4. Dresselhaus, M. S.; Dresselhaus, G.; Eklund, P. C., Chapter 15 - Superconductivity. In *Science of Fullerenes and Carbon Nanotubes*, Academic Press: San Diego, 1996; pp 616-653.
5. Scharff, P., Fundamental Properties and Applications of Fullerene and Carbon Nanotube Systems. In *Frontiers of Multifunctional Nanosystems*, Springer Netherlands: Dordrecht, 2002; pp 213-224.
6. Zachariah, M.; Romanini, M.; Zygouri, P.; Gournis, D.; Tamarit, J. L.; Barrio, M.; Macovez, R. *Synthetic Metals* **2016**, 217, 123-128.
7. Saikia, I.; Borah, A. J.; Phukan, P. *Chemical Reviews* **2016**, 116, (12), 6837-7042.
8. Klouda, K.; Zemanova, E.; Friedrichova, R.; Weisheitova, M. *International Journal of Materials Science and Applications*. **2014**, 3, (6), 293-302.
9. Hennig, G. *The Journal of Chemical Physics* **1952**, 20, (9), 1443-1447.
10. Tadashi, S.; Yoichi, T.; Takashi, M. *Bulletin of the Chemical Society of Japan* **1970**, 43, (1), 34-38.
11. Lee, R. S.; Kim, H. J.; Fischer, J. E.; Thess, A.; Smalley, R. E. *Nature* **1997**, 388, (6639), 255-257.
12. Bulusheva, L. G.; Okotrub, A. V.; Flahaut, E.; Asanov, I. P.; Gevko, P. N.; Koroteev, V. O.; Fedoseeva, Y. V.; Yaya, A.; Ewels, C. P. *Chemistry of Materials* **2012**, 24, (14), 2708-2715.
13. Tongay, S.; Hwang, J.; Tanner, D. B.; Pal, H. K.; Maslov, D.; Hebard, A. F. *Physical Review B* **2010**, 81, (11), 115428.

14. Jung, N.; Kim, N.; Jockusch, S.; Turro, N. J.; Kim, P.; Brus, L. *Nano Letters* **2009**, 9, (12), 4133-4137.
15. Jankovsky, O.; Simek, P.; Klimova, K.; Sedmidubsky, D.; Matejkova, S.; Pumera, M.; Sofer, Z. *Nanoscale* **2014**, 6, (11), 6065-6074.
16. Mansour, A. E.; Dey, S.; Amassian, A.; Tanielian, M. H. *ACS Applied Materials & Interfaces* **2015**, 7, (32), 17692-17699.
17. Djordjević, A.; Vojinović-Miloradov, M.; Petranović, N.; Devečerski, A.; Lazar, D.; Ribar, B. *Fullerene Science and Technology* **1998**, 6, (4), 689-694.
18. Seshadri, R.; Govindaraj, A.; Nagarajan, R.; Pradeep, T.; Rao, C. N. R. *Tetrahedron Letters* **1992**, 33, (15), 2069-2070.
19. Miyamoto, Y.; Oshiyama, A.; Saito, S. *Solid State Communications* **1992**, 82, (6), 437-441.
20. Sekine, H.; Maeda, H.; Kosuge, M.; Tanaka, Y.; Tokumoto, M. *Journal of Applied Physics* **1992**, 72, (11), 5448-5450.
21. Djordjevic, A.; Srdjenovic, B.; Seke, M.; Petrovic, D.; Injac, R.; Mrdjanovic, J. *Journal of Nanomaterials* **2015**, 2015, 15.
22. Macovez, R.; Mitsari, E.; Zachariah, M.; Romanini, M.; Zygouri, P.; Gournis, D.; Tamarit, J. L. *The Journal of Physical Chemistry C* **2014**, 118, (9), 4941-4950.
23. Antihovich, I. V.; Ablazhey, N. M.; Chernik, A. A.; Zharsky, I. M. *Procedia Chemistry* **2014**, 10, 373-377.
24. Ouyang, J.; Hong Goh, S.; Izaac Elim, H.; Chen Meng, G.; Ji, W. *Chemical Physics Letters* **2002**, 366, (3-4), 224-230.
25. Kondo, H.; Ohtake, Y. *NIPPON GOMU KYOKAISHI* **2009**, 82, (3), 98-104.
26. Vileno, B.; Marcoux, P. R.; Lekka, M.; Sienkiewicz, A.; Fehér, T.; Forró, L. *Advanced Functional Materials* **2006**, 16, (1), 120-128.
27. Injac, R.; Prijatelj, M.; Strukelj, B., Fullerenol Nanoparticles: Toxicity and Antioxidant Activity. In *Oxidative Stress and Nanotechnology: Methods and Protocols*, Armstrong, D.; Bharali, J. D., Eds. Humana Press: Totowa, NJ, 2013; pp 75-100.
28. Cai, X.; Jia, H.; Liu, Z.; Hou, B.; Luo, C.; Feng, Z.; Li, W.; Liu, J. *Journal of Neuroscience Research* **2008**, 86, (16), 3622-3634.
29. Zhou, A.; Zhang, J.; Xie, Q.; Yao, S. *Biomaterials* **2001**, 22, (18), 2515-2524.

30. Marko, L. *Recent Patents on Biotechnology* **2009**, 3, (2), 118-123.
31. Letenko, D. G.; Nikitin, V. A.; Semenov, K. N.; Charykov, N. A.; Ivanov, A. S. *Russian Journal of Physical Chemistry A* **2012**, 86, (12), 1808-1815.
32. Navarro, D. A.; Kookana, R. S.; McLaughlin, M. J.; Kirby, J. K. *Environmental Science & Technology Letters* **2016**, 3, (1), 7-12.
33. Indeglia, P. A.; Georgieva, A.; Krishna, V. B.; Bonzongo, J.-C. J. *Journal of Nanoparticle Research* **2014**, 16, (9), 1-15.
34. Tomić, M.; Vasić-Milovanović, A.; Matija, L.; Koruga, Đ. *Fullerenes, Nanotubes and Carbon Nanostructures* **2016**, 24, (7), 423-426.
35. Tisserant, J. N.; Reissner, P. A.; Jenatsch, S.; Beyer, H.; Hany, R.; Stemmer, A. *RSC Advances* **2016**, 6, (28), 23141-23147.
36. Santhosh, V.; Voggu, R.; Chaturbedy, P.; Ganapathy, R.; Rao, C. N. R. *Carbon* **2016**, 96, 1-5.
37. Zhang, Y. Q.; Wang, W. J.; Li, S. H.; Gao, X. X.; Zhang, B. Y.; Liu, Y. L.; Wang, Q. G.; Shi, Q., Langmuir-blodgett films of a new diels-alder adduct of C60 with 1,1'-biindene. In *Materials Science Forum*, 2015; Vol. 809-810.
38. Minar, N. K.; Hou, K.; Westermeier, C.; Döblinger, M.; Schuster, J.; Hanusch, F. C.; Nickel, B.; Ozin, G. A.; Bein, T. *Angewandte Chemie - International Edition* **2015**, 54, (26), 7577-7581.
39. Leman, D.; Kelly, M. A.; Ness, S.; Engmann, S.; Herzing, A.; Snyder, C.; Ro, H. W.; Kline, R. J.; DeLongchamp, D. M.; Richter, L. J. *Macromolecules* **2015**, 48, (2), 383-392.
40. Kojima, H.; Abe, R.; Ito, M.; Tomatsu, Y.; Fujiwara, F.; Matsubara, R.; Yoshimoto, N.; Nakamura, M. *Applied Physics Express* **2015**, 8, (12).
41. Gengler, R. Y. N.; Gournis, D.; Aimon, A. H.; Toma, L. M.; Rudolf, P. *Chemistry-a European Journal* **2012**, 18, (24), 7594-7600.
42. Gayathri, S. S.; Patnaik, A. *Chemical Physics Letters* **2007**, 433, (4-6), 317-322.
43. Conoci, S.; Guldi, D. M.; Nardis, S.; Paolesse, R.; Kordatos, K.; Prato, M.; Ricciardi, G.; Vicente, M. G. H.; Zilbermann, I.; Valli, L. *Chemistry-a European Journal* **2004**, 10, (24), 6523-6530.

44. Kouloumpis, A.; Dimos, K.; Spyrou, K.; Georgakilas, V.; Rudolf, P.; Gournis, D. *Frontiers in Materials* **2015**, 2, (10).
45. Malgas, G. F.; Motaung, D. E.; Arendse, C. J. *Journal of Materials Science* **2012**, 47, (10), 4282-4289.
46. Jiang, X.; Yuan, M.; Liu, H.; Liubang, L.; Du, Z. *Materials Letters* **2016**, 176, 52-55.
47. Tutt, L. W.; Kost, A. *Nature* **1992**, 356, (6366), 225-226.
48. Allemand, P. M.; Khemani, K. C.; Koch, A.; Wudl, F.; Holczer, K.; Donovan, S.; Gruner, G.; Thompson, J. D. *Science* **1991**, 253, (5017), 301-303.
49. Lewandowska, K.; Pilarczyk, K.; Podborska, A.; Kim, T. D.; Lee, K. S.; Szaciłowski, K. *Applied Physics Letters* **2015**, 106, (4).
50. Zhang, Z.; Wei, L.; Qin, X.; Li, Y. *Nano Energy* **2015**, 15, 490-522.
51. Mi, D.; Kim, J. H.; Kim, H. U.; Xu, F.; Hwang, D. H. *Journal of Nanoscience and Nanotechnology* **2014**, 14, (2), 1064-1084.
52. Savagatrup, S.; Printz, A. D.; O'Connor, T. F.; Zaretski, A. V.; Rodriguez, D.; Sawyer, E. J.; Rajan, K. M.; Acosta, R. I.; Root, S. E.; Lipomi, D. J. *Energy and Environmental Science* **2015**, 8, (1), 55-80.
53. Kumar, P. *Water and Energy International* **2014**, 57 RNI, (6), 23-27.
54. Wu, Q.; Zhao, D.; Schneider, A. M.; Chen, W.; Yu, L. *Journal of the American Chemical Society* **2016**, 138, (23), 7248-7251.
55. Liang, P. W.; Chueh, C. C.; Williams, S. T.; Jen, A. K. Y. *Advanced Energy Materials* **2015**, 5, (10).
56. Ueda, H.; Nishiyama, K.; Yoshimoto, S. *Electrochimica Acta* **2016**, 210, 155-162.
57. Foote, C. S. *Topics in Current Chemistry* **1994**, 169, 347-363.
58. Chlistunoff, J.; Cliffl, D.; Bard, A. J. *Thin Solid Films* **1995**, 257, (2), 166-184.
59. Kopova, I.; Lavrentiev, V.; Vacik, J.; Bacakova, L. *PLoS ONE* **2015**, 10, (4), e0123680.
60. Hirsch, A. *Angewandte Chemie-International Edition in English* **1993**, 32, (8), 1138-1141.
61. Giacalone, F.; Martín, N. *Chemical Reviews* **2006**, 106, (12), 5136-5190.
62. Konishi, T.; Ikeda, A.; Shinkai, S. *Tetrahedron* **2005**, 61, (21), 4881-4899.

63. Nierengarten, J. F. *New Journal of Chemistry* **2004**, 28, (10), 1177-1191.
64. Michopoulos, A.; Kouloumpis, A.; Gournis, D.; Prodromidis, M. I. *Electrochimica Acta* **2014**, 146, 477-484.
65. Gengler, R. Y. N.; Veligura, A.; Enotiadis, A.; Diamanti, E. K.; Gournis, D.; Jozsa, C.; van Wees, B. J.; Rudolf, P. *Small* **2010**, 6, (1), 35-39.
66. Michopoulos, A.; Kouloumpis, A.; Gournis, D.; Prodromidis, M. I. *Electrochimica Acta* **2014**, 146, (0), 477-484.
67. Birkett, P. R.; Kroto, H. W.; Taylor, R.; Walton, D. R. M.; Ian Grose, R.; Hendra, P. J.; Fowler, P. W. *Chemical Physics Letters* **1993**, 205, (4), 399-404.
68. Simons, W. W., *The Sadtler Handbook of Infrared Spectra*. Sadtler: 1978.
69. Macovez, R.; Mitsari, E.; Zachariah, M.; Romanini, M.; Zygouri, P.; Gournis, D.; Tamarit, J. L. *Journal of Physical Chemistry C* **2014**, 118, (9), 4941-4950.
70. Kuzmany, H.; Pfeiffer, R.; Hulman, M.; Kramberger, C. *Philosophical Transactions of the Royal Society a-Mathematical Physical and Engineering Sciences* **2004**, 362, (1824), 2375-2406.
71. Echeverria, J.; Casanova, D.; Lluell, M.; Alemany, P.; Alvarez, S. *Chemical Communications* **2008**, (24), 2717-2725.
72. Huong, P. V. *Solid State Communications* **1993**, 88, (1), 23-26.
73. Tebbe, F. N.; Harlow, R. L.; Chase, D. B.; Thorn, D. L.; Campbell, G. C.; Calabrese, J. C.; Herron, N.; Young, R. J.; Wasserman, E. *Science* **1992**, 256, (5058), 822-825.
74. Shen, X.; Lin, X.; Yousefi, N.; Jia, J.; Kim, J.-K. *Carbon* **2014**, 66, 84-92.
75. Chen, Y.; Guo, F.; Jachak, A.; Kim, S.-P.; Datta, D.; Liu, J.; Kulaots, I.; Vaslet, C.; Jang, H. D.; Huang, J.; Kane, A.; Shenoy, V. B.; Hurt, R. H. *Nano Letters* **2012**, 12, (4), 1996-2002.
76. Dekany, I.; Kruger-Grasser, R.; Weiss, A. *Colloid and Polymer Science* **1998**, 276, (7), 570-576.
77. Gournis, D.; Georgakilas, V.; Karakassides, M. A.; Bakas, T.; Kordatos, K.; Prato, M.; Fanti, M.; Zerbetto, F. *Journal of the American Chemical Society* **2004**, 126, (27), 8561-8568.

78. Ferrari, A. C.; Meyer, J. C.; Scardaci, V.; Casiraghi, C.; Lazzeri, M.; Mauri, F.; Piscanec, S.; Jiang, D.; Novoselov, K. S.; Roth, S.; Geim, A. K. *Physical Review Letters* **2006**, 97, (18), 187401.
79. Torrisi, F.; Hasan, T.; Wu, W.; Sun, Z.; Lombardo, A.; Kulmala, T. S.; Hsieh, G.-W.; Jung, S.; Bonaccorso, F.; Paul, P. J.; Chu, D.; Ferrari, A. C. *ACS Nano* **2012**, 6, (4), 2992-3006.
80. Tuinstra, F.; Koenig, J. L. *The Journal of Chemical Physics* **1970**, 53, (3), 1126-1130.
81. Cancado, L. G.; Jorio, A.; Ferreira, E. H. M.; Stavale, F.; Achete, C. A.; Capaz, R. B.; Moutinho, M. V. O.; Lombardo, A.; Kulmala, T. S.; Ferrari, A. C. *Nano Letters* **2011**, 11, (8), 3190-3196.
82. Martins Ferreira, E. H.; Moutinho, M. V. O.; Stavale, F.; Lucchese, M. M.; Capaz, R. B.; Achete, C. A.; Jorio, A. *Physical Review B* **2010**, 82, (12), 125429.
83. Leiro, J. A.; Heinonen, M. H.; Laiho, T.; Batirev, I. G. *Journal of Electron Spectroscopy and Related Phenomena* **2003**, 128, (2-3), 205-213.
84. Xing, G.; Zhang, J.; Zhao, Y.; Tang, J.; Zhang, B.; Gao, X.; Yuan, H.; Qu, L.; Cao, W.; Chai, Z.; Ibrahim, K.; Su, R. *The Journal of Physical Chemistry B* **2004**, 108, (31), 11473-11479.
85. Sun, Y.-B.; Cao, C.-Y.; Yang, S.-L.; Huang, P.-P.; Wang, C.-R.; Song, W.-G. *Chemical Communications* **2014**, 50, (71), 10307-10310.
86. Spyrou, K.; Calvaresi, M.; Diamanti, E. K.; Tsoufis, T.; Gournis, D.; Rudolf, P.; Zerbetto, F. *Advanced Functional Materials* **2015**, 25, (2), 263-269.
87. Spyrou, K.; Kang, L.; Diamanti, E. K.; Gengler, R. Y.; Gournis, D.; Prato, M.; Rudolf, P. *Carbon* **2013**, 61, 313-320.





## Chapter 5

### Graphene/carbon-dot hybrid thin films prepared by a modified Langmuir-Schaefer method

The special electronic, optical, thermal and mechanical properties of graphene resulting from its 2D nature, together the ease of functionalizing it through a simple acid treatment make graphene an ideal building block for the development of new hybrid nanostructures with well-defined dimensions and behaviour. Such hybrids have great potential as active materials in applications such as gas storage, gas/liquid separation, photocatalysis, bioimaging, optoelectronics and nanosensing. In this study, luminescent carbon dots (C-dots) were sandwiched between oxidized graphene sheets to form novel hybrid multilayer films. Our thin-film preparation approach combines self-assembly with the Langmuir-Schaefer deposition and uses graphene oxide nanosheets as template for grafting C-dots in a bidimensional array. Repeating the cycle results in a facile and low-cost layer-by-layer procedure for the formation of highly ordered hybrid multilayers, which were characterized by photoluminescence, UV-Vis, X-ray photoelectron and Raman spectroscopies, as well as X-ray diffraction and atomic force microscopy.

---

This chapter is based on the article: "Graphene/carbon-dot hybrid thin films prepared by a modified Langmuir-Schaefer method", by A. Kouloumpis, E. Thomou, N. Chalmes, K. Dimos, K. Spyrou, A. B. Bourlinos, I. Koutselas, D. Gournis and P. Rudolf. *ACS Omega* 2017, 2 (5), 2090-2099.

## 5.1 Introduction

Carbon dots (C-dots),<sup>1, 2</sup> which were serendipitously discovered during the purification of single-walled carbon nanotubes,<sup>3</sup> have an almost spherical shape and sizes ranging from 10 to a few nanometers. Their good solubility, low cytotoxicity,<sup>4, 5</sup> great compatibility,<sup>6</sup> efficient functionalization<sup>7</sup> and chemical passivity<sup>8</sup> make them suitable for applications in bioimaging,<sup>4, 9</sup> photocatalysis,<sup>10</sup> drug and gene delivery,<sup>11, 12</sup> optoelectronic devices,<sup>13, 14</sup> nanoprobe<sup>15</sup> and sensors.<sup>16, 17</sup> The C-dots can be synthesized by many methods namely, laser ablation,<sup>18</sup> microwave-assisted pyrolysis,<sup>19</sup> thermal oxidation,<sup>20</sup> arc discharge,<sup>3</sup> electrochemical oxidation,<sup>21, 22</sup> ultrasonication<sup>23</sup> and combustion.<sup>24</sup> Microwave-assisted pyrolysis, which was used in this study, is a preferable choice because of its low cost, facility and efficiency. A remarkable property of C-dots is photoluminescence; however, the mechanism generating it is not yet well understood but several potential origins have been suggested such as surface passivation, surface groups, polyaromatic fluorophores, pairing of electrons and holes on the surface of the C-dot, differently sized nanoparticles and structural defects.<sup>25, 26</sup>

In this study we aim at arranging C-dots in two-dimensional arrays. In fact, 2D materials have revealed outstanding and promising prospects in science and nanotechnology in the last years because of their unique properties in the fields of photonics, sensing, flexible electronics and energy harvesting.<sup>27, 28</sup> Graphene, being a single-layered material with superior electronic, optical, thermal and mechanical properties is ideally suited for layer-by-layer (LbL) assembly. Novel functional materials<sup>29</sup> with modified, optimized, or enhanced properties can be formed by constructing pillared structures where graphene sandwiches a variety of guest moieties. Thus, the synthesis of a hybrid thin film, combining the properties of carbon dots and graphene is a great challenge for potential applications in the fields of sensing, catalysis, optoelectronics and biomedicine.

There have already been several efforts in this direction, for instance Datta *et al.*<sup>30</sup> prepared a hybrid material combining chemically oxidized graphene (also known as graphene oxide, GO) and C-dots for bioimaging and cell-labeling applications. The

synthesis of this material was achieved *via* non-covalent interactions following a self-assembly path. The fluorescence of the carbon dots was not majorly changed by the vicinity of graphene oxide and the cytotoxicity remained at a relatively low level. Another example is the work of Zhang *et al.*,<sup>31</sup> who synthesized a composite material via direct assembly of carbon dots on the layered double hydroxide (LDH) surface. This hybrid material is an excellent absorber of methyl blue, making it suitable for the removal of anionic organic dyes.

In this study, a facile and low-cost bottom-up layer-by-layer (LbL) approach, which combines the Langmuir-Schaefer (LS) with self-assembly (SA) technique, was used for the production of new class of highly ordered C-dot intercalated graphene structures.<sup>32</sup> This method uses graphene oxide nanosheets as platform for grafting C-dots in a 2D configuration and allows for perfect layer-by-layer growth.<sup>33</sup> This precise control combined with the possibility to cover large substrates in a homogeneous fashion make the LB technique promising for preventing aggregation of carbon-based nanostructures such as fullerene derivatives or carbon dots<sup>34, 35, 36</sup> in hybrid multilayers.

For our thin film preparation approach the C-dots (with a mean diameter of 4 nm) were produced via microwave assisted pyrolysis,<sup>37</sup> using citric acid which acts as the carbon source and urea that offers the hydrophilic amine-groups on the surface of the C-dots. Suspensions of graphene oxide (prepared as described below) in ultrapure water were used as subphase in the Langmuir-Blodgett (LB) deposition system. As described in our previous work,<sup>32, 38</sup> spreading the long-chain molecule octadecylamine (ODA) on the water surface triggers the GO to covalently bond via the amide functionality. This results in the formation of a Langmuir film of ODA-GO on the water surface, the packing of which can be modified by applying an external pressure through the movable barrier of the LB apparatus. The hybrid Langmuir film was transferred to a hydrophobic support (hydrophobicity increases the transfer ratio) by horizontally lowering it (known as LS method) to touch the ODA-GO/water interface. After lifting the substrate again from the interface, it was lowered into an aqueous dispersion of C-dots to induce self-assembly of the latter on the GO sheets. By repeating this cyclic procedure hybrid multilayer films were fabricated and

characterized by photoluminescence, UV-Vis, X-ray photoelectron and Raman spectroscopies as well as X-ray diffraction and atomic force microscopy.

## **5.2 Experimental Section**

### **5.2.1 Materials**

Citric acid (99%), urea (98%), octadecylamine (99%, ODA), acetone, methanol and ethanol were purchased from Sigma-Aldrich while nitric acid (65%), sulfuric acid (95-97%), potassium chlorate and powder graphite (pulum,  $\leq 0.2$  mm) were acquired from Fluka. Ultrapure water (18.2 M $\Omega$ ) was produced by a Millipore Simplicity® system. The Si-wafers (P/Bor, single side polished, Si-Mat) and quartz substrates (Aldrich) were cleaned prior to use for 15 min in an ultrasonic bath with water, acetone and ethanol. All reagents were of analytical grade and used without further purification.

### **5.2.2 Synthesis of graphene oxide**

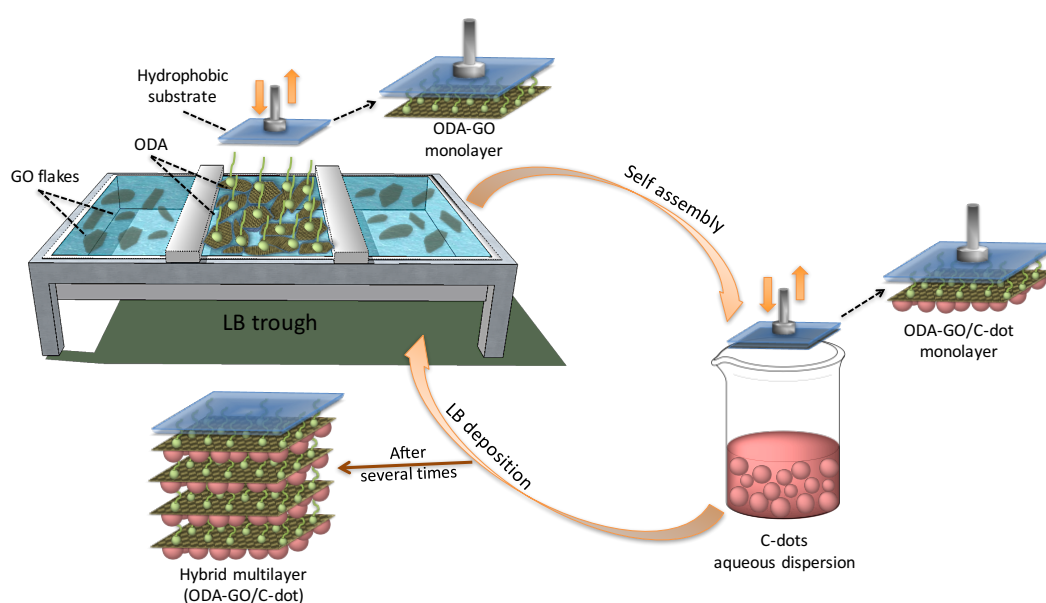
Graphene oxide (GO) was synthesized using a modified Staudenmaier method, as described in Chapter 3 (see section 3.2.2). The oxidation procedure was repeated two more times and finally the sample was dried at room temperature.

### **5.2.3 Synthesis of C-dots**

Carbon dots were synthesized using microwave-assisted pyrolysis.<sup>37</sup> More specifically, 3 g of citric acid and 3 g of urea were dissolved in 10 mL distilled-deionized water in order to form a transparent solution. The solution was heated in a microwave oven (750 W, HOME, HMG23\_8EL) for 5 min and subsequently heated in a drying oven at 65 °C overnight. A certain amount of water was added to the obtained solid, forming a dark brown aqueous dispersion, which was filtered in order to remove large particles. The C-dots were used immediately after the filtration or kept in dark for later use. It is noteworthy to mention that C-dots are quite sensitive to light as their color after a couple of weeks of exposure to light changes from dark orange to light orange, then yellow and finally light yellow.

### 5.2.4 Preparation of hybrid graphene/C-dots multilayers

A Langmuir Blodgett trough (KSV 2000 Nima Technology) was cleaned with ethanol and distilled-deionized water. GO suspensions in ultrapure water ( $0.02 \text{ mg mL}^{-1}$ ) were used as subphase and a Pt Wilhelmy plate was employed to monitor the surface pressure during the compression and deposition procedures. For the formation of GO film in the air-water interface,  $200 \mu\text{L}$  of a  $0.2 \text{ mg mL}^{-1}$  ODA solution in chloroform/methanol 9/1 (v/v) were spread onto the subphase with the help of a microsyringe. After a waiting time of 20 min to allow solvent evaporation and the GO-surfactant functionalization to occur, the hybrid ODA-GO layer was compressed at a rate of  $5 \text{ mm min}^{-1}$  until the target surface pressure of  $20 \text{ mN m}^{-1}$  was reached, forming a dense ODA-GO Langmuir layer.<sup>39</sup> This pressure was maintained throughout the deposition process. Layers were transferred onto the hydrophobic substrates by the LS technique (horizontal dipping), with downward and lifting speeds of  $10$  and  $5 \text{ mm min}^{-1}$ , respectively. After the transfer of the ODA-GO layer to substrates, the hybrid GO film was dipped into an aqueous dispersion of C-dots ( $0.2 \text{ mg mL}^{-1}$ ) to induce the formation of a graphene/C-dot hybrid layer (**ODA-GO/C-dot**) by self-assembly. A hybrid multilayer film was formed by repeating this cyclic procedure for 60 times, as shown in Scheme 5.1.



**Scheme 5.1.** Schematic representation of the synthetic procedure for the development of the hybrid GO/C-dot multilayer film.

After each deposition step the substrates were rinsed several times by dipping into ultrapure water (to remove any weakly attached cations or molecules that remained from the deposition steps) and dried with nitrogen flow (to avoid contaminating the aqueous suspension in the LB trough and/or the C-dot dispersion).<sup>39, 40</sup> Hydrophobic Si-wafers and surfactant-treated quartz substrates (see Appendix B for quartz modification) were used for the deposition of the hybrid films.

## **5.3 Results and Discussion**

### **5.3.1 Structural and morphological characterization of pristine C-dots**

Carbon dots were synthesized by employing the microwave-assisted pyrolysis procedure applied by Qu *et al.*<sup>37</sup> According to these authors, water-soluble luminescent C-dots decorated with terminal amine groups on the surface of the dots exhibiting relative stable physicochemical and optical features are obtained. A detailed characterization of the produced C-dots (including XRD, FT-IR, UV-Vis and XPS measurements as well as optical images of their aqueous dispersions and films under UV light) confirms these conclusions and is presented in the Appendix B. PL spectra of the C-dots aqueous dispersions with excitation wavelengths from 300 to 460 nm are shown in Figure 5.1. These spectra are typical of C-dots<sup>7, 18</sup> exhibiting excitation-dependent photoluminescence with emission red shifting from ~425 nm up to ~525 nm with increasing excitation wavelength. The maximum fluorescence intensity with emission at 447 nm is observed when the C-dots are excited at 360 nm. The broad emission bands, as well as the appearance of two distinctive peaks in Fig. 5.1e spectrum or shoulders in other spectra, as at ~500 nm in the case of Fig. 5.1d, reveal the complicated mechanism of the C-dot fluorescence.<sup>41</sup> The presence of various surface groups and traps leads to many dissimilar states which can be involved in the emission process and thus also explains the excitation-dependent nature of the C-dot photoluminescence.<sup>41</sup>

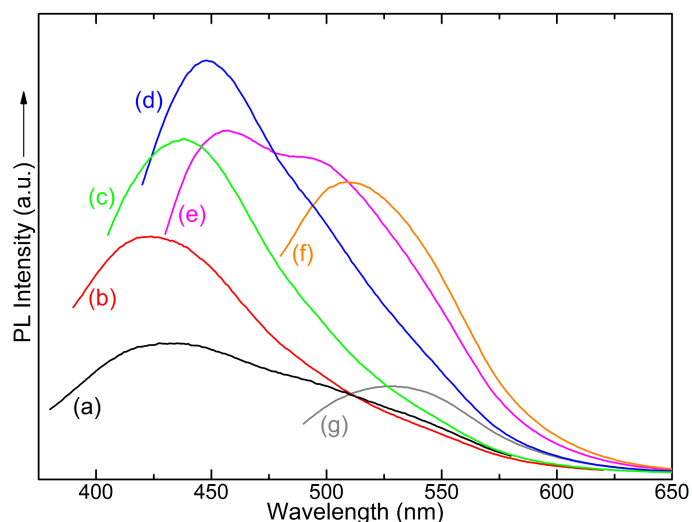


**Figure 5.1.** Photoluminescence spectra of C-dots aqueous dispersion; Excitation wavelengths: (a) 300 nm; (b) 320 nm; (c) 340 nm; (d) 360 nm; (e) 380 nm; (f) 400 nm and (g) 460 nm.

To image pristine C-dots by we adopted a deposition procedure in which we first transferred a stearic acid Langmuir film on a Si-wafer and then horizontally dipped it into the C-dot dispersion to induce self-assembly (for the details of the preparation see the Appendix B). AFM images of such a stearic acid/C-dot hybrid monolayer are shown in Figure 5.2.

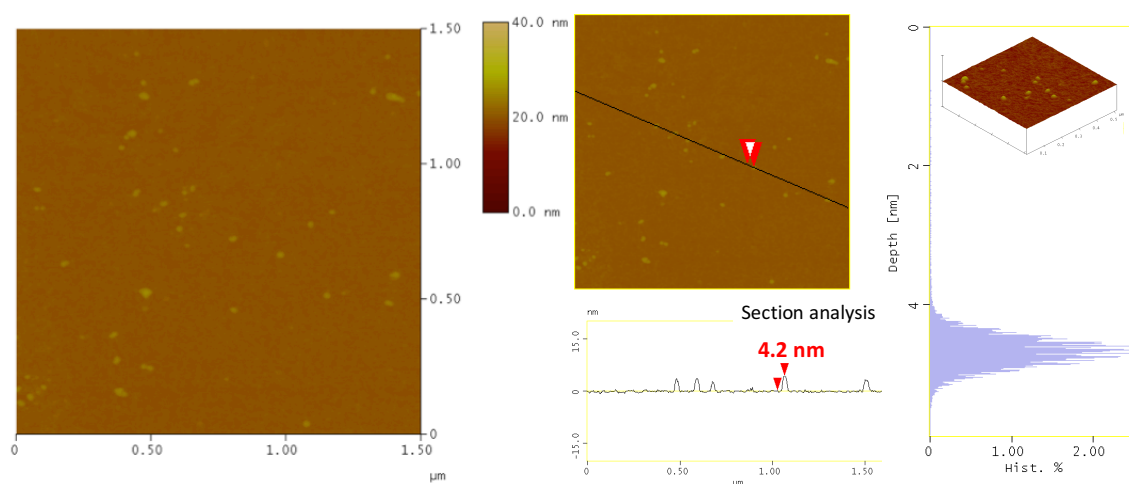


**Figure 5.2.** AFM topography images of a stearic acid/C-dot hybrid monolayer deposited on a Si-wafer (Section analysis and Depth analysis histogram are included)

Isolated and uniform particles can be observed, confirming that combining the Langmuir-Schaefer technique with self-assembly<sup>34, 35, 42</sup> avoids aggregation of C-dots. From the topographical height profile (section analysis) the height of particles is found to be about  $4.2 \pm 0.2$  nm, as derived, while their average height deduced from the depth-analysis histogram<sup>37</sup> is  $4.5 \pm 0.2$  nm.

### 5.3.2 Structural control and characterization of hybrid ODA-GO/C-dot monolayers

$\pi$ -A isotherms of ODA Langmuir films on pure water and on an aqueous GO suspension (20 ppm) are shown in Figure 5.3. The curves show the change in the slope corresponding to the phase transitions of ODA-GO sheets from a 2D gas to a 2D liquid phase and then to a 2D solid during the compression process.<sup>39, 40</sup> In the absence of GO, the  $\pi$ -A isotherm is a smoothly increasing curve with a lift off area of  $32.8 \text{ \AA}^2$ . When adding a small amount of GO ( $0.02 \text{ mg mL}^{-1}$ ) to the aqueous subphase, the lift-off area increases to  $52 \text{ \AA}^2$ , which demonstrates that the GO flakes stabilize the ODA layer<sup>39</sup> through covalent grafting of the terminal amine groups of ODA to the epoxides of the GO sheets via nucleophilic substitution reactions.<sup>43-45</sup>

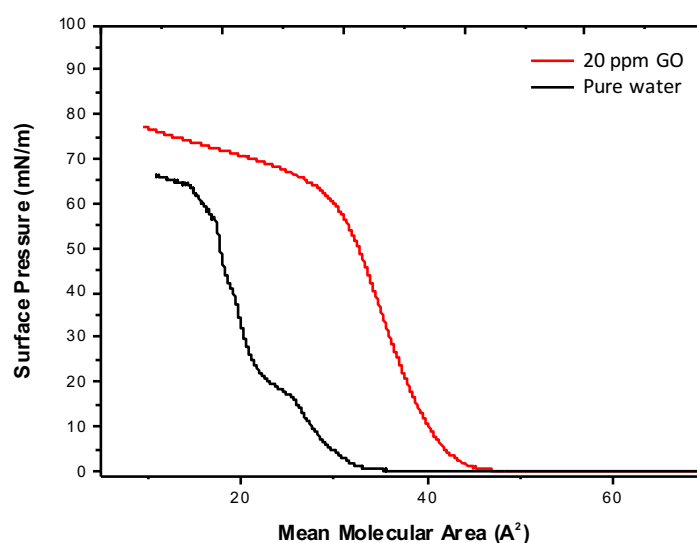


**Figure 5.3.**  $\pi$ -A isotherms of ODA Langmuir films on pure water and on an aqueous dispersion of GO.



Representative AFM images of the first hybrid ODA-GO/C-dot monolayer deposited on Si-wafer by combining the LS method with self-assembly are presented in Figure 5.4. The topographic images show that the surface coverage of the substrate is quite high; GO layers with well defined edges are almost contacting each other with small voids between them. This closely packed homogeneous array demonstrates the highly controllable formation of ODA-GO/C-dot hybrid layers.<sup>39</sup> The average thickness of the flakes is 1.0-1.5 nm as derived from topographical height profile (section analysis) corresponding to the size of single graphene oxide layers,<sup>46</sup> which is 6.1 Å. Moreover, uniform particles can be observed on top of the GO layers. The average size (section analysis) of these particles is 4.5-5.0 nm corresponding to the exact size of the pristine C-dots (see Fig. 5.2).

Raman spectra of ODA-GO/C-dot and ODA-GO hybrid monolayers deposited on Si-wafer are presented in Figure 5.5. Both spectra display the characteristic D- and G-bands associated with  $sp^3$  and  $sp^2$  hybridized carbon atoms, respectively.<sup>47, 48</sup>

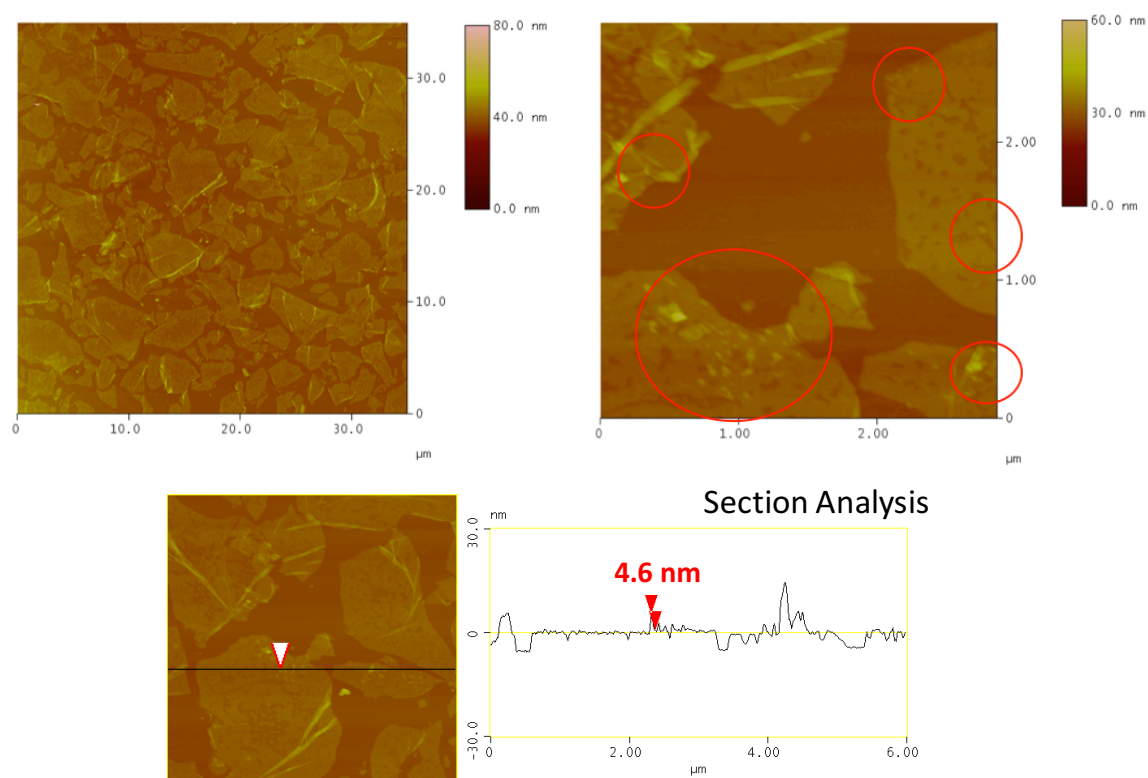


**Figure 5.4.** AFM height images and section analysis of ODA-GO/C-dot hybrid monolayers deposited by combining the Langmuir Schaefer method with self-assembly.

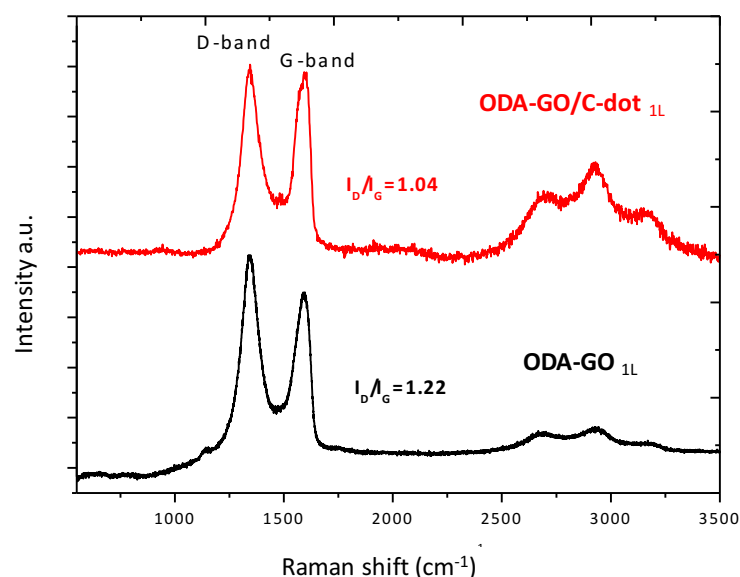


**Figure 5.5.** Raman spectra of ODA-GO and ODA-GO/C-dot hybrid monolayers

Because of the presence of ODA, the D-band intensity is significantly enhanced for the ODA-GO layer, which is also reflected in the ratio of the intensities of D-band to G-band ( $I_D/I_G$ ) that is frequently used to express the degree of functionalization of graphene materials and amounts to 1.22. In contrast, the  $I_D/I_G$  ratio decreases to 1.04 when C-dots are added to the hybrid system, in agreement with the Raman spectrum of C-dots alone where the  $I_D/I_G$  ratio amounts to 0.95 (see Fig. B6 in the Appendix B). Both spectra exhibit three broad bands at  $\sim 2700$ ,  $\sim 2930$  and  $\sim 3180$   $\text{cm}^{-1}$  which are linked to the 2D vibrational mode, D+D' mode and 2D' mode, respectively.<sup>47-50</sup> Although no shifting of the peaks is observed, the grafting of the C-dots enhances the intensity of the bands in the 2D region. We can therefore conclude that the change in the  $I_D/I_G$  ratio and the intensity increase in the 2D region testify to the successful attachment of C-dots on the surface of ODA-GO and hence the formation of the ODA-GO/C-dot hybrid monolayer.

### 5.3.3 Characterization of graphene/C-dot hybrid films

The X-ray diffraction patterns of the a 60 layer thick graphene/C-dot hybrid multilayer, in comparison with the pattern of a ODA-GO/ODA hybrid multilayer constructed under the same conditions are shown in Figure 5.6. The graphene/C-dot

hybrid multilayer shows the 001 diffraction peak below  $2^\circ$  ( $2\theta$ ) indicating the successful intercalation of C-dots between the organo-modified GO sheets. Since this peak also partially overlaps with the (000) beam, we also report the spectrum where a baseline was subtracted (see red line in Figure 5.6). The 001 peak's position at  $2\theta=1.7^\circ$  corresponds to a  $d_{001}$ -spacing of  $52.0\pm 0.1$  Å. The position of the 003 reflection peak at  $5.1^\circ$  confirms this result. The  $d_{001}$  value of 52.0 Å is much higher than the corresponding value of a hybrid organo-GO multilayer ( $d_{001}=37.6\pm 0.1$  Å), where instead of the C-dots a second ODA molecule is grafted in the self-assembly step. In fact, we propose that the hydrophilic-terminal groups of C-dots interact with a first graphene oxide layer while at the same time they interpenetrate the flexible organic chains of ODA molecules covalently attached on the second GO layer (see inset sketch).

The C1s core level X-ray photoemission spectrum of a 60 layer thick ODA-GO/C-dot hybrid multilayer is shown in Figure 5.7 and compared to the spectra of pristine GO and of C-dots. The C1s core level X-ray photoemission spectrum of graphene oxide reveals the different oxygen functional groups emerging after the oxidation.

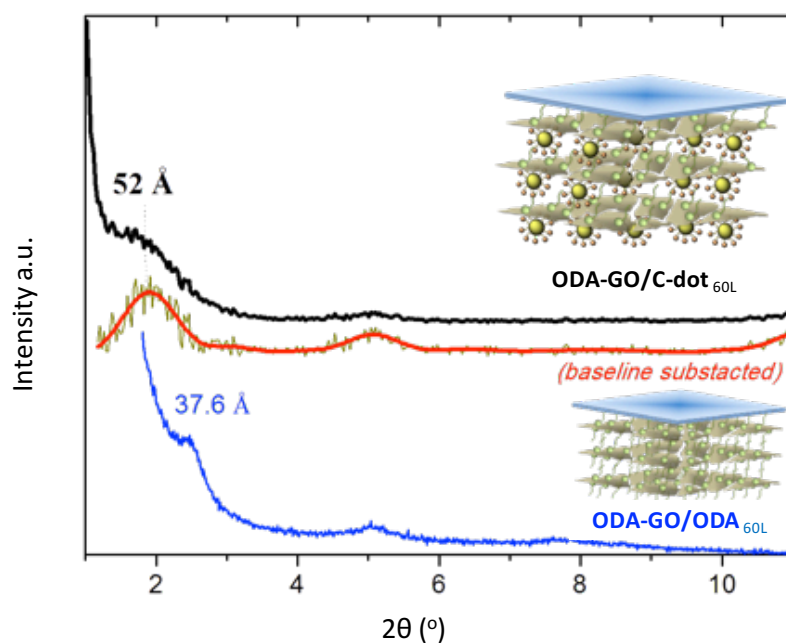


**Figure 5.6.** Comparison of XRD pattern of a 60 layer thick ODA-GO/C-dot hybrid multilayer with a 60 layer thick ODA-GO/ODA multilayer

More specifically, the contribution at 288.1 eV is due to carbonyl (C = O) groups and makes up 11.0% of the total carbon intensity, the peak due to epoxy (C–O–C) functional groups is located at 286.9 eV and correspond to 32.5% of the total carbon intensity. Two peaks centred at 285.5 eV and 289.1 eV stem from the C–O and C(O)O bonds and represent 34.5% and 17.8% of the total carbon 1s peak intensity, respectively. Additionally one identifies the peak at 284.6 eV arising from the C-C and C-H bonds of the hexagonal lattice and accounting for 4.2% of the total carbon intensity. On the other hand, the C1s photoelectron spectrum of carbon dots comprises three peaks that are assigned to C-C and/or C-H bonds (66.7% of the total spectral intensity), C-O and/or C-N bonds (21.0 %) and C=O bonds (12.3 %). The spectrum of hybrid multilayer consists of five components; a first peak at 284.6 eV is due to C-C and C-H bonds contributing just 6.9% in the total C1s intensity. The main component at 285.6 eV (61.0%) is ascribed to the C-O and C-N bonds and arises from the hydroxyl moieties of both GO and C-dots as well as from the amine groups of ODA and C-dots. The third peak at 286.6 eV (11.8%) is assigned to the C-O-C epoxide/ether groups; this peak is significantly reduced compared to the GO photoelectron spectra due to the bond between the amine end groups of carbon-dots and the epoxy groups of GO. Finally, the peak at 287.7 eV (17.0%) represents the ketonic functionalities (C=O), while the smallest contribution (3.3%) at 288.9 eV comes of carboxyl groups (O-C=O). The high intensity of the C-O/C-N peak and the significant contribution of the carbonyl groups imply that the C-dots bear both oxygen and nitrogen containing surface functional groups, as confirmed by the FT-IR and XPS spectra of the pristine C-dots in the Appendix B.

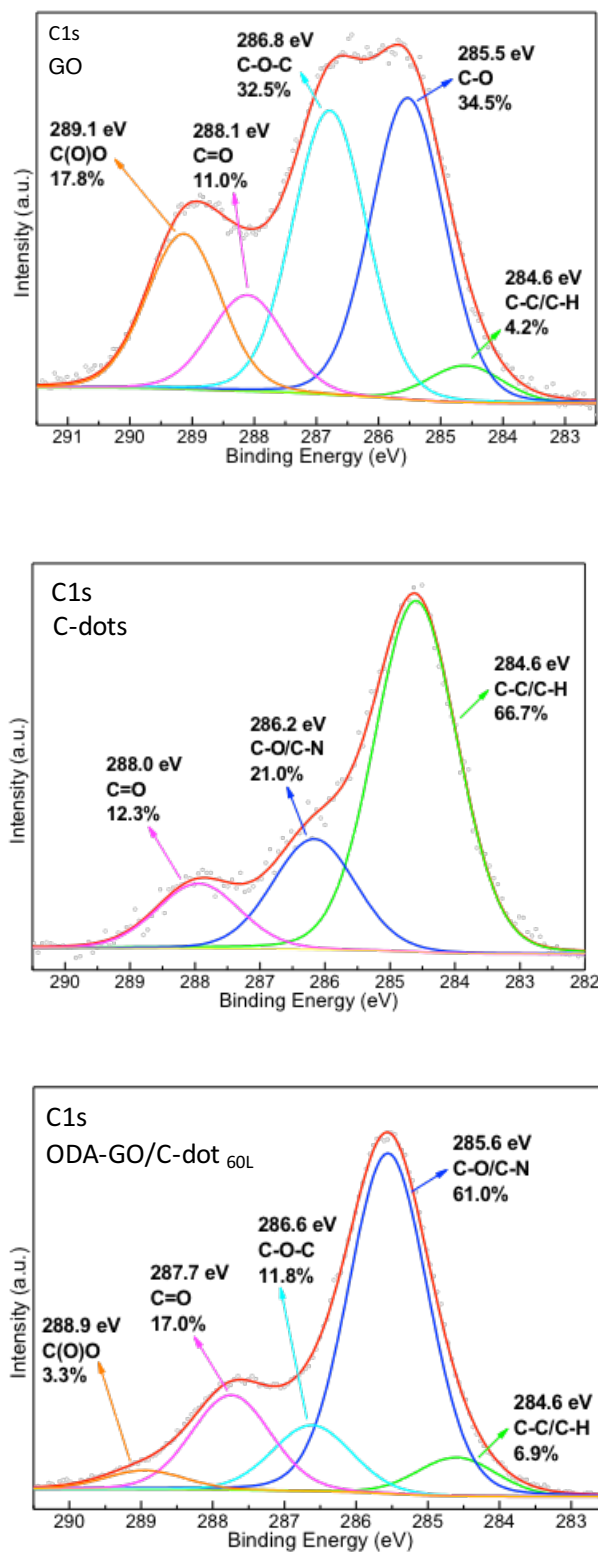


**Figure 5.7.** C1s core level X-ray photoemission spectra of graphene oxide (GO) (top panel), C-dots (middle panel) and graphene/C-dot hybrid multilayer (bottom panel).

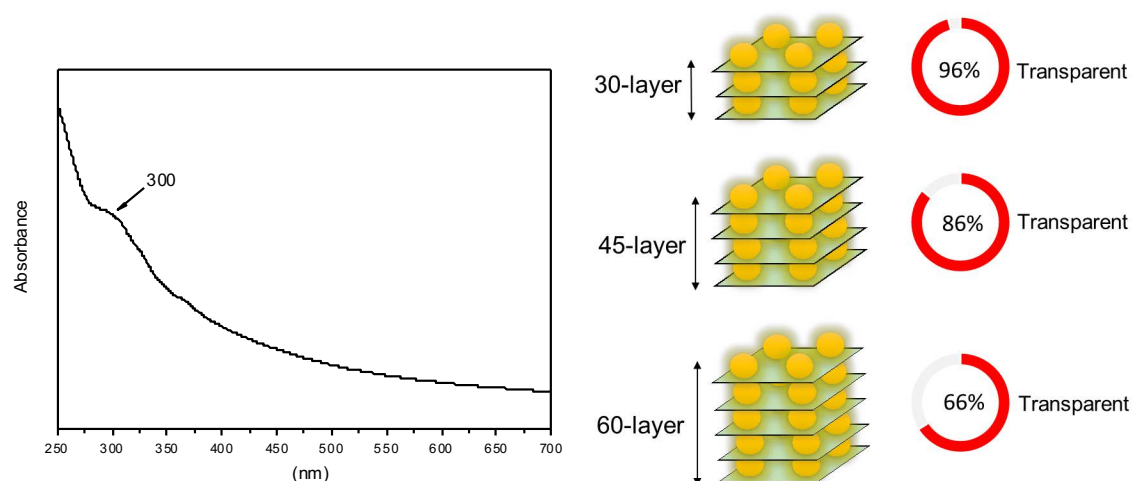


**Figure 5.8.** UV-Vis absorption spectrum of a 60 layer thick ODA-GO/C-dot hybrid multilayer deposited on quartz (left) and transparency (at 550 nm) for different thicknesses of the deposited hybrid layers (right).

The UV-Vis absorption spectrum of the 60 layer thick ODA-GO/C-dot hybrid multilayer deposited on quartz substrates is presented in Figure 5.8 (left) and shows an ascending absorption profile from lower to higher energies with a tiny absorption step at around 300 nm. The latter as well as the overall absorption characteristics of the material are correlated with the presence of C-dots in the interlayer space of the hybrid multilayer. Furthermore, the transparency can be controlled by adjusting the number of the deposited layers; a 30-layer film is 96 % transparent at 550 nm, while the transparency of 45-layer film and 60-layer film decreases to 86 % and 66 %, respectively (Figure 5.8 right). These values are considerable higher compared with other graphene-based films reported in the literature.<sup>51-56</sup>

As expected, the hybrid multilayers display photoluminescence due to the presence of C-dot. The PL spectra of the ODA-GO/C-dot hybrid multilayer collected with excitation wavelengths from 280 to 440 nm are shown in Figure 5.9. Once again, excitation-dependent photoluminescence characteristic of C-dots is observed. As the excitation wavelength varies from 280 to 440 nm, emission shifts from ~356 nm up to ~555 nm. In contrast to the pristine C-dots, the maximum fluorescence intensity of the hybrid multilayer is observed when exciting at high energy (280 nm) and produces an emission peaked at 356 nm.

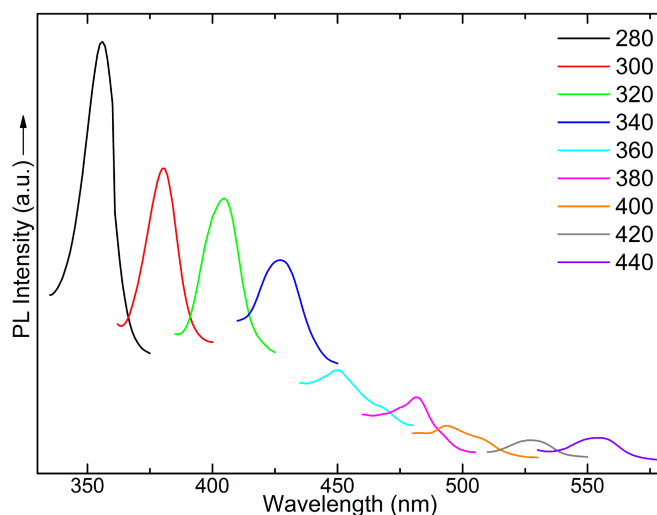


**Figure 5.9.** Photoluminescence spectra of the ODA-GO/C-dot hybrid multilayers with excitation wavelengths from 280 to 440 nm.

Moreover, the emission peaks are significantly narrower compared to the peaks of the PL spectra of pristine C-dots. The latter two facts suggest that either only smaller C-dots were incorporated in the interlayer space of GO - as also suggested by the AFM analysis, or the interparticle interactions between C-dots are much smaller in the hybrid multilayer; of course also both hypothesis could be true. In any case, the hybrid multilayers exhibit adjustable and high quality photoluminescence with narrow emission lines.

Furthermore, it is important to note that the ODA-GO/C-dot hybrid films do not appear to exhibit any PL quenching phenomena. This fact can be deduced by comparing the number of C-dots accessible by the PL excitation beam, with a 3 mm  $\times$  3 mm frontal area, in a 60 layer film to the number of C-dots accessed when the beam passes through the pristine C-dot aqueous dispersion, where the depth of the source beam penetration is assumed 5 mm and all self-absorption effects have been excluded. Assuming that three C-dots are positioned on each graphene sheet, spaced 50 nm from each other in both directions, it can be estimated that the number of accessible C-dots is  $216 \cdot 10^9$ . On the contrary, if the beam accesses an aqueous dispersion of C-dots, where each C-dot has a mass density of  $2 \text{ g/cm}^3$  and a radius of 2.5 nm and the dispersion was prepared as 0.15 g C-dots/mL of  $\text{H}_2\text{O}$ , the accessible number of C-dots by the beam is  $2.2 \cdot 10^{13}$ . Thus, the number of C-dots

interrogated in the ODA-GO/C-dot film is 100 times less than those being observed in the solution. Therefore, if the C-dots within the ODA-GO/C-dot suffered any PL quenching, their already lower concentration would not have provided such a strong PL signal. In fact, as recently reported by Vassilakopoulou *et al.*,<sup>57</sup> C-dots encapsulated in MCM-41, continue to exhibit their PL signal without quenching while being protected by the matrix.

## **5.4 Conclusions**

In summary, a low cost and highly controllable layer-by-layer synthetic approach for the preparation of a new class of hybrid intercalated graphene structures is presented. A hybrid multilayer consisting of luminescent carbon dots (C-dots) sandwiched between graphene oxide layers was successfully fabricated by combining the Langmuir-Schaefer method with self-assembly. This approach allows for a tunable coverage, uniformity over extended surface areas and single-layer-level control of the assembly as confirmed by  $\pi$ -A isotherms and AFM. X-ray diffraction measurements revealed the presence of the C-dots within graphene nanosheets and confirmed the highly ordered structure of the hybrid multilayer. We postulate that the hydrophilic-terminal groups of C-dots interact with graphene oxide layer above while at the same time being trapped within the flexible organic chains of the organic surfactant (ODA) that is covalently attached on a second GO layer below. The existence of C-dots in the hybrid multilayer system was corroborated by X-ray photoelectron spectroscopy while Raman spectroscopy showed that the insertion of the C-dots between the graphene oxide nanosheets left the electronic structure of GO unaffected. The transparency of the hybrid multilayers can be controlled by adjusting the number of the deposited layers and is considerable higher than that of other graphene-based films reported in the literature. Finally, the hybrid multilayers exhibit adjustable and high-quality photoluminescence with narrow emission lines. The ODA-GO/C-dot multilayer constitutes a novel hybrid system suitable for being employed in diverse applications such as nanoprobe, sensors, optoelectronic



devices and transparent electrodes as well as in the fields of photocatalysis and drug delivery. Moreover, another potential application of the produced graphene/C-dot hybrid thin films is in light emitting diodes (LEDs). Recently, X. Zhang *et al.*<sup>58</sup> have fabricated a carbon-dot based LED, where the color of the light emitted from the C-dots is voltage dependent and with increasing bias, the emission peaks also became stronger.<sup>58</sup> In our hybrid system the use of graphene as a template could play an important role because the conductivity of graphene can enhance the voltage-dependent color emission of C-dots favoring the development of colorful and brighter LEDs with multicolor single pixels

## 5.5 References

1. Zhao, A.; Chen, Z.; Zhao, C.; Gao, N.; Ren, J.; Qu, X. *Carbon* **2015**, 85, 309-327.
2. Lim, S. Y.; Shen, W.; Gao, Z. *Chem. Soc. Rev.* **2015**, 44, (1), 362-381.
3. Xu, X.; Ray, R.; Gu, Y.; Ploehn, H. J.; Gearheart, L.; Raker, K.; Scrivens, W. A. *Journal of the American Chemical Society* **2004**, 126, (40), 12736-12737.
4. Yang, S.-T.; Cao, L.; Luo, P. G.; Lu, F.; Wang, X.; Wang, H.; Mezziani, M. J.; Liu, Y.; Qi, G.; Sun, Y.-P. *Journal of the American Chemical Society* **2009**, 131, (32), 11308-11309.
5. Yang, S.-T.; Wang, X.; Wang, H.; Lu, F.; Luo, P. G.; Cao, L.; Mezziani, M. J.; Liu, J.-H.; Liu, Y.; Chen, M.; Huang, Y.; Sun, Y.-P. *The Journal of Physical Chemistry C* **2009**, 113, (42), 18110-18114.
6. Baker, S. N.; Baker, G. A. *Angewandte Chemie International Edition* **2010**, 49, (38), 6726-6744.
7. Dimos, K. *Current Organic Chemistry* **2016**, 20, (6), 682-695.
8. Zhai, X.; Zhang, P.; Liu, C.; Bai, T.; Li, W.; Dai, L.; Liu, W. *Chemical Communications* **2012**, 48, (64), 7955-7957.
9. Chen, B.; Li, F.; Li, S.; Weng, W.; Guo, H.; Guo, T.; Zhang, X.; Chen, Y.; Huang, T.; Hong, X.; You, S.; Lin, Y.; Zeng, K.; Chen, S. *Nanoscale* **2013**, 5, (5), 1967-1971.
10. Qu, D.; Zheng, M.; Du, P.; Zhou, Y.; Zhang, L.; Li, D.; Tan, H.; Zhao, Z.; Xie, Z.; Sun, Z. *Nanoscale* **2013**, 5, (24), 12272-12277.
11. Liu, C.; Zhang, P.; Zhai, X.; Tian, F.; Li, W.; Yang, J.; Liu, Y.; Wang, H.; Wang, W.; Liu, W. *Biomaterials* **2012**, 33, (13), 3604-3613.
12. Song, Y.; Shi, W.; Chen, W.; Li, X.; Ma, H. *Journal of Materials Chemistry* **2012**, 22, (25), 12568-12573.
13. Guo, X.; Wang, C.-F.; Yu, Z.-Y.; Chen, L.; Chen, S. *Chemical Communications* **2012**, 48, (21), 2692-2694.
14. Wang, F.; Chen, Y.-h.; Liu, C.-y.; Ma, D.-g. *Chemical Communications* **2011**, 47, (12), 3502-3504.

15. Zhi, Y.; Zhaohui, L.; Minghan, X.; Yujie, M.; Jing, Z.; Yanjie, S.; Feng, G.; Hao, W.; Liying, Z. *Nano-Micro Letters* **2013**, 5, (4), 247-259.
16. Wei, W.; Xu, C.; Ren, J.; Xu, B.; Qu, X. *Chemical Communications* **2012**, 48, (9), 1284-1286.
17. Zhou, L.; Lin, Y.; Huang, Z.; Ren, J.; Qu, X. *Chemical Communications* **2012**, 48, (8), 1147-1149.
18. Sun, Y.-P.; Zhou, B.; Lin, Y.; Wang, W.; Fernando, K. A. S.; Pathak, P.; Mezziani, M. J.; Harruff, B. A.; Wang, X.; Wang, H.; Luo, P. G.; Yang, H.; Kose, M. E.; Chen, B.; Veca, L. M.; Xie, S.-Y. *Journal of the American Chemical Society* **2006**, 128, (24), 7756-7757.
19. Zhu, H.; Wang, X.; Li, Y.; Wang, Z.; Yang, F.; Yang, X. *Chemical Communications* **2009**, (34), 5118-5120.
20. Bourlinos, A. B.; Stassinopoulos, A.; Anglos, D.; Zboril, R.; Georgakilas, V.; Giannelis, E. P. *Chemistry of Materials* **2008**, 20, (14), 4539-4541.
21. Zhao, Q.-L.; Zhang, Z.-L.; Huang, B.-H.; Peng, J.; Zhang, M.; Pang, D.-W. *Chemical Communications* **2008**, (41), 5116-5118.
22. Zhou, J.; Booker, C.; Li, R.; Zhou, X.; Sham, T.-K.; Sun, X.; Ding, Z. *Journal of the American Chemical Society* **2007**, 129, (4), 744-745.
23. Li, H.; He, X.; Liu, Y.; Huang, H.; Lian, S.; Lee, S.-T.; Kang, Z. *Carbon* **2011**, 49, (2), 605-609.
24. Tian, L.; Ghosh, D.; Chen, W.; Pradhan, S.; Chang, X.; Chen, S. *Chemistry of Materials* **2009**, 21, (13), 2803-2809.
25. Georgakilas, V.; Perman, J. A.; Tucek, J.; Zboril, R. *Chemical Reviews* **2015**, 115, (11), 4744-4822.
26. Wang, Y.; Hu, A. *Journal of Materials Chemistry C* **2014**, 2, (34), 6921-6939.
27. Kaul, A. B. *J. Mater. Res.* **2014**, 29, (03), 348-361.
28. Feng, W.; Zhenxing, W.; Qisheng, W.; Fengmei, W.; Lei, Y.; Kai, X.; Yun, H.; Jun, H. *Nanotechnology* **2015**, 26, (29), 292001.
29. Kouloumpis, A.; Zygouri, P.; Dimos, K.; Gournis, D., Layer-by-Layer Assembly of Graphene-Based Hybrid Materials. In *Functionalization of Graphene*, Wiley-VCH Verlag GmbH & Co. KGaA: 2014; pp 359-400.

30. Datta, K. K. R.; Kozak, O.; Ranc, V.; Havrdova, M.; Bourlinos, A. B.; Safarova, K.; Hola, K.; Tomankova, K.; Zoppellaro, G.; Otyepka, M.; Zboril, R. *Chemical Communications* **2014**, 50, (74), 10782-10785.
31. Zhang, M.; Yao, Q.; Lu, C.; Li, Z.; Wang, W. *ACS Applied Materials & Interfaces* **2014**, 6, (22), 20225-20233.
32. Kouloumpis, A.; Spyrou, K.; Dimos, K.; Georgakilas, V.; Rudolf, P.; Gournis, D. *Frontiers in Materials* **2015**, 2, 10.
33. Gengler, R. Y. N.; Gournis, D.; Aimon, A. H.; Toma, L. M.; Rudolf, P. *Chemistry-a European Journal* **2012**, 18, (24), 7594-7600.
34. Bourlinos, A. B.; Georgakilas, V.; Bakandritsos, A.; Kouloumpis, A.; Gournis, D.; Zboril, R. *Materials Letters* **2012**, 82, 48-50.
35. Bourlinos, A. B.; Bakandritsos, A.; Kouloumpis, A.; Gournis, D.; Krysmann, M.; Giannelis, E. P.; Polakova, K.; Safarova, K.; Hola, K.; Zboril, R. *Journal of Materials Chemistry* **2012**, 22, (44), 23327-23330.
36. Bourlinos, A. B.; Karakassides, M. A.; Kouloumpis, A.; Gournis, D.; Bakandritsos, A.; Papagiannouli, I.; Aloukos, P.; Couris, S.; Hola, K.; Zboril, R.; Krysmann, M.; Giannelis, E. P. *Carbon* **2013**, 61, 640-643.
37. Qu, S.; Wang, X.; Lu, Q.; Liu, X.; Wang, L. *Angewandte Chemie International Edition* **2012**, 51, (49), 12215-12218.
38. Gengler, R. Y. N.; Toma, L. M.; Pardo, E.; Lloret, F.; Ke, X. X.; Van Tendeloo, G.; Gournis, D.; Rudolf, P. *Small* **2012**, 8, (16), 2532-2540.
39. Kouloumpis, A.; Dimos, K.; Spyrou, K.; Georgakilas, V.; Rudolf, P.; Gournis, D. *Frontiers in Materials* **2015**, 2, 10.
40. Michopoulos, A.; Kouloumpis, A.; Gournis, D.; Prodromidis, M. I. *Electrochim. Acta* **2014**, 146, 477-484.
41. Arcudi, F.; Đorđević, L.; Prato, M. *Angewandte Chemie* **2016**, 128, (6), 2147-2152.
42. Bourlinos, A. B.; Trivizas, G.; Karakassides, M. A.; Baikousi, M.; Kouloumpis, A.; Gournis, D.; Bakandritsos, A.; Hola, K.; Kozak, O.; Zboril, R.; Papagiannouli, I.; Aloukos, P.; Couris, S. *Carbon* **2015**, 83, 173-179.
43. Gengler, R. Y. N.; Veligura, A.; Enotiadis, A.; Diamanti, E. K.; Gournis, D.; Jozsa, C.; van Wees, B. J.; Rudolf, P. *Small* **2010**, 6, (1), 35-39.

44. Bourlinos, A. B.; Gournis, D.; Petridis, D.; Szabo, T.; Szeri, A.; Dekany, I. *Langmuir* **2003**, 19, (15), 6050-6055.
45. Dreyer, D. R.; Park, S.; Bielawski, C. W.; Ruoff, R. S. *Chemical Society Reviews* **2010**, 39, (1), 228-240.
46. Dekany, I.; Kruger-Grasser, R.; Weiss, A. *Colloid and Polymer Science* **1998**, 276, (7), 570-576.
47. Ferrari, A. C.; Meyer, J. C.; Scardaci, V.; Casiraghi, C.; Lazzeri, M.; Mauri, F.; Piscanec, S.; Jiang, D.; Novoselov, K. S.; Roth, S.; Geim, A. K. *Physical Review Letters* **2006**, 97, (18), 187401.
48. Torrisi, F.; Hasan, T.; Wu, W.; Sun, Z.; Lombardo, A.; Kulmala, T. S.; Hsieh, G.-W.; Jung, S.; Bonaccorso, F.; Paul, P. J.; Chu, D.; Ferrari, A. C. *ACS Nano* **2012**, 6, (4), 2992-3006.
49. Cançado, L. G.; Jorio, A.; Ferreira, E. H. M.; Stavale, F.; Achete, C. A.; Capaz, R. B.; Moutinho, M. V. O.; Lombardo, A.; Kulmala, T. S.; Ferrari, A. C. *Nano Lett.* **2011**, 11, (8), 3190-3196.
50. Martins Ferreira, E. H.; Moutinho, M. V. O.; Stavale, F.; Lucchese, M. M.; Capaz, R. B.; Achete, C. A.; Jorio, A. *Physical Review B* **2010**, 82, (12), 125429.
51. Fan, T.-J.; Yuan, C.-Q.; Tang, W.; Tong, S.-Z.; Liu, Y.-D.; Huang, W.; Min, Y.-G.; Arthur, J. E. *Chin. Phys. Lett.* **2015**, 32, (7), 076802.
52. He, L.; Tjong, S. C. *Journal of Materials Chemistry C* **2016**, 4, (29), 7043-7051.
53. Lin, X.; Jia, J.; Yousefi, N.; Shen, X.; Kim, J.-K. *Journal of Materials Chemistry C* **2013**, 1, (41), 6869-6877.
54. Su, R.; Sun, W. F.; Tian, C.; Huang, W. M.; Lin, S. F.; Chen, D. Q.; Chen, G. H. *RSC Advances* **2015**, 5, (58), 46785-46789.
55. Zheng, Q.; Li, Z.; Yang, J.; Kim, J.-K. *Prog. Mater. Sci.* **2014**, 64, 200-247.
56. Zheng, Q.; Zhang, B.; Lin, X.; Shen, X.; Yousefi, N.; Huang, Z.-D.; Li, Z.; Kim, J.-K. *J. Mater. Chem.* **2012**, 22, (48), 25072-25082.
57. Vassilakopoulou, A.; Georgakilas, V.; Vainos, N.; Koutselas, I. *J. Phys. Chem. Solids* **2017**, 103, 190-196.

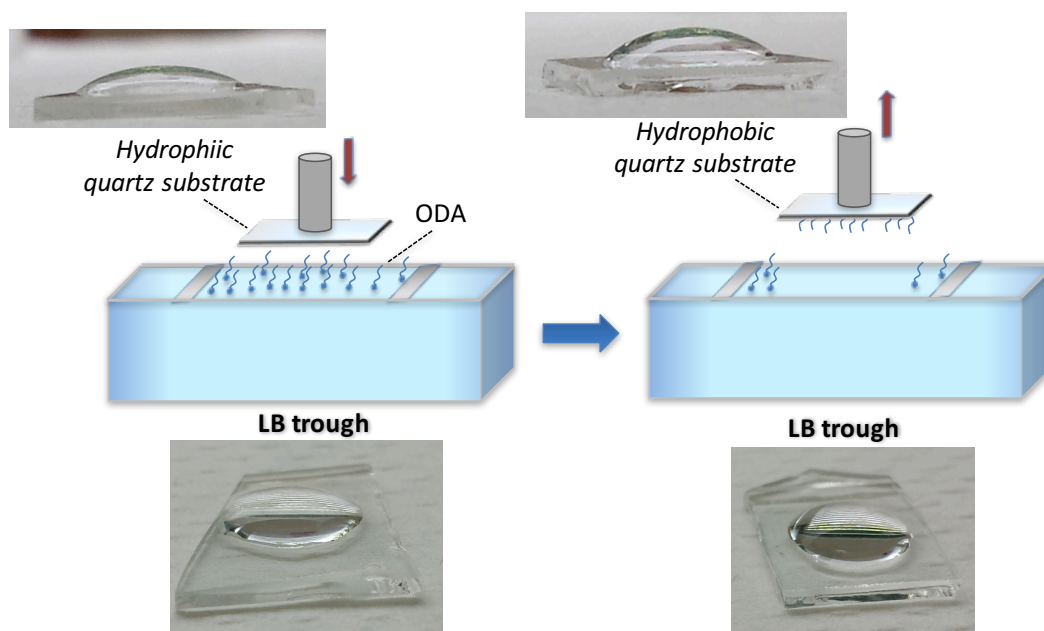
58. Zhang, X.; Zhang, Y.; Wang, Y.; Kalytchuk, S.; Kershaw, S. V.; Wang, Y.; Wang, P.; Zhang, T.; Zhao, Y.; Zhang, H.; Cui, T.; Wang, Y.; Zhao, J.; Yu, W. W.; Rogach, A. L. *ACS Nano* **2013**, 7, (12), 11234-11241.

# Appendix B

## B.1 Experimental procedures

### B.1.1 Preparation of hydrophobic quartz substrates

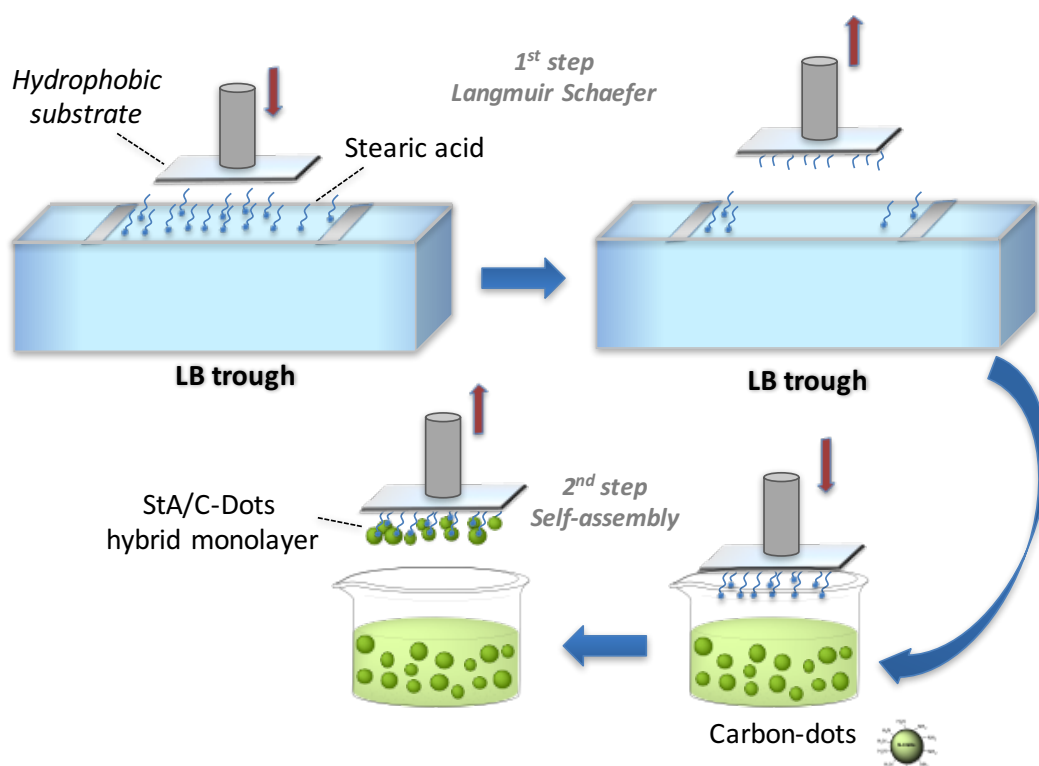
The surface modification of hydrophilic quartz substrates (Sigma Aldrich) achieved by a one-step Langmuir Schaefer (LS) deposition in a Langmuir Blodgett (LB) trough. Ultrapure water was used as subphase and octadecylamine (99%, ODA, Sigma Aldrich) ( $0.2 \text{ mg mL}^{-1}$ ) dissolved in chloroform/methanol 9/1 (v/v) was spread onto the surface with the help of a microsyringe. The hydrophilic quartz was dipped horizontally (LS method) at a constant surface pressure of  $30 \text{ mN m}^{-1}$  as shown in Scheme B1. After the LS deposition, the quartz substrate was rinsed with pure water and dried with a flow of  $\text{N}_2$  gas.



**Scheme B1.** Schematic representation of surface modification of hydrophilic quartz substrates.

### B.1.2 Deposition of isolated C-dots on Si-wafers for the AFM measurements

Isolated pristine C-dots deposited on Si-wafers (Si-Mat) were obtained by a technique which combines Langmuir-Schaefer deposition and self-assembly.<sup>1-3</sup> Ultrapure water was used as subphase in the LB trough and a stearic acid (99%, Fluka) ( $0.2 \text{ mg mL}^{-1}$ ) dissolved in chloroform-methanol (9:1) was spread onto the aqueous subphase with the help of a microsyringe. A hydrophobic Si-wafer was dipped horizontally in the air-water surface (LS method) at a constant surface pressure of  $15 \text{ mN m}^{-1}$ . After the LS deposition, the substrate was rinsed with pure water and dipped into an aqueous dispersion ( $0.2 \text{ mg mL}^{-1}$ ) of C-dots as shown in Scheme B2. Finally, the surface was rinsed copiously with pure water and dried with a flow of  $\text{N}_2$  gas.



**Scheme B2.** Schematic representation of the synthetic procedure for the deposition of isolated C-dots on a hydrophobic Si-wafer.



## B.2 Characterization of pristine C-dots

The X-ray diffraction pattern of the produced C-dots (in powder) is shown in Figure B1. The broad peak at  $\sim 25^\circ$  with a d-spacing of 3.5 Å corresponds to highly disordered carbon atoms, similar to the graphite lattice spacing.<sup>4-7</sup>

FT-IR was used in order to identify the functional groups on the surface of the carbon dots (in powder) (Figure B2). The broad absorption band at 3000-3500  $\text{cm}^{-1}$  is attributed to the stretching vibrations of O–H and N–H. The absorption bands at 1600 and 1710  $\text{cm}^{-1}$  are attributed to the stretching vibrations of C=O, whereas those at 1405 and 1355  $\text{cm}^{-1}$  to the bending vibrations of CH<sub>2</sub>. Finally, the band located at 1055  $\text{cm}^{-1}$  is attributed to the stretching vibrations of C–O–C.<sup>4, 8, 9</sup>

The UV-vis spectrum (Figure B3) of an aqueous dispersion of the carbon dots (0.2 mg mL<sup>-1</sup>) is comparable to previous literature reports<sup>4</sup> and consists of two main absorption bands at 340 and 405 nm.

The Raman spectrum (Figure B4) of the pristine C-dots (in powder) displays the characteristic D and G bands that are attributed to the sp<sup>3</sup> and sp<sup>2</sup> hybridized carbon atoms respectively. The relative intensity ( $I_D/I_G$ ) for the C-dots is equal to 0.95.

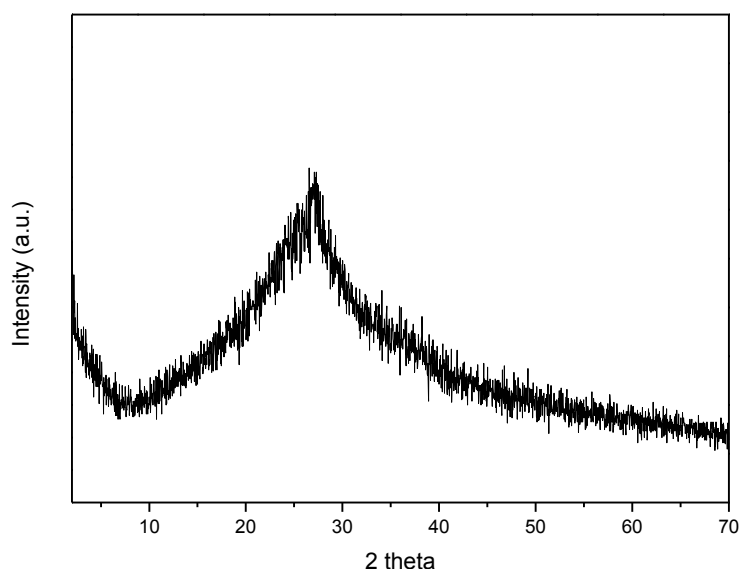


**Figure B1.** X-ray diffraction pattern of pristine C-dots.

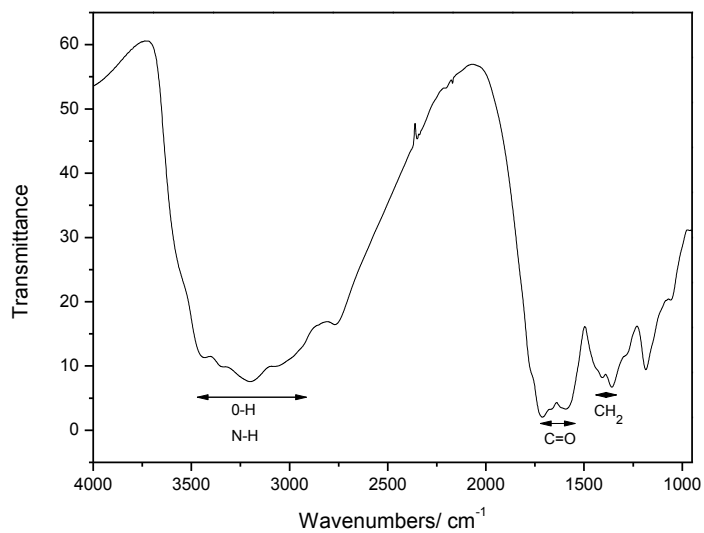


**Figure B2.** FT-IR spectrum of pristine C-dots.

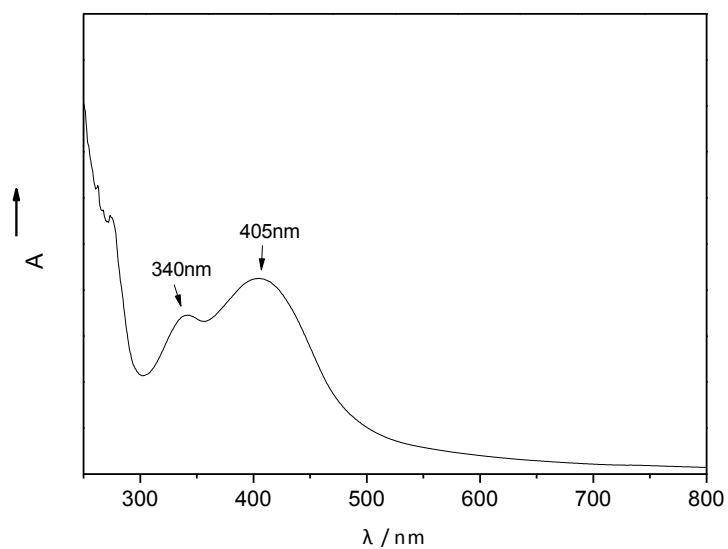


**Figure B3.** UV-Vis spectrum of an aqueous dispersion of C-dots.

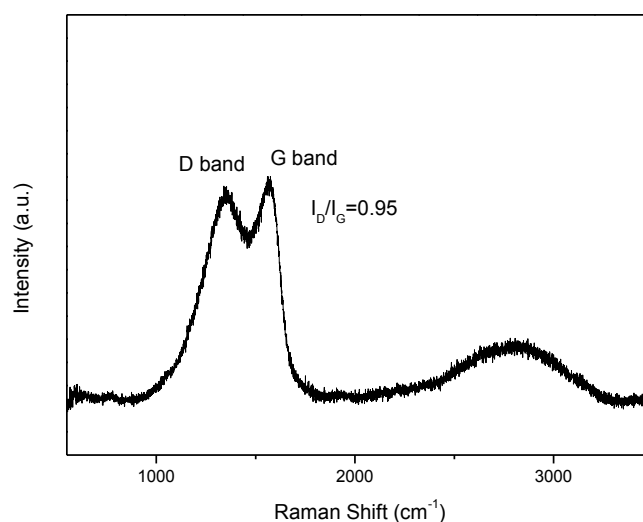


**Figure B4.** Raman spectrum of pristine C-dots.

The C1s photoelectron spectrum of carbon dots (Figure B5 left) consists of three peaks. The first one at a binding energy of 284.6 eV is attributed to the C-C and/or C-H bonds (66.7% of the total C1s spectral intensity), the second one at 286.2 eV to C-O and C-N bonds (21.0%) while the last peak at 288.0 eV arises from the C=O bonds and constitutes 12.3% of the spectral intensity. The N1s photoelectron spectrum of carbon dots (Figure B5 right) is deconvoluted into two photoelectron peaks, one at 399.8 eV binding energy,<sup>10</sup> which is attributed to the amine groups and a second one at 401.5 eV due to protonated amines of the C-dots. The atomic percentage of carbon, nitrogen and oxygen atoms is reported in Table below.

Finally, images of aqueous dispersion of C-dots under normal light and UV illumination at 254 nm and 365 nm are shown in Figure B6. Analogous optical and fluorescent images of C-dots deposited on a commercial filtration paper are shown in Figure B7.

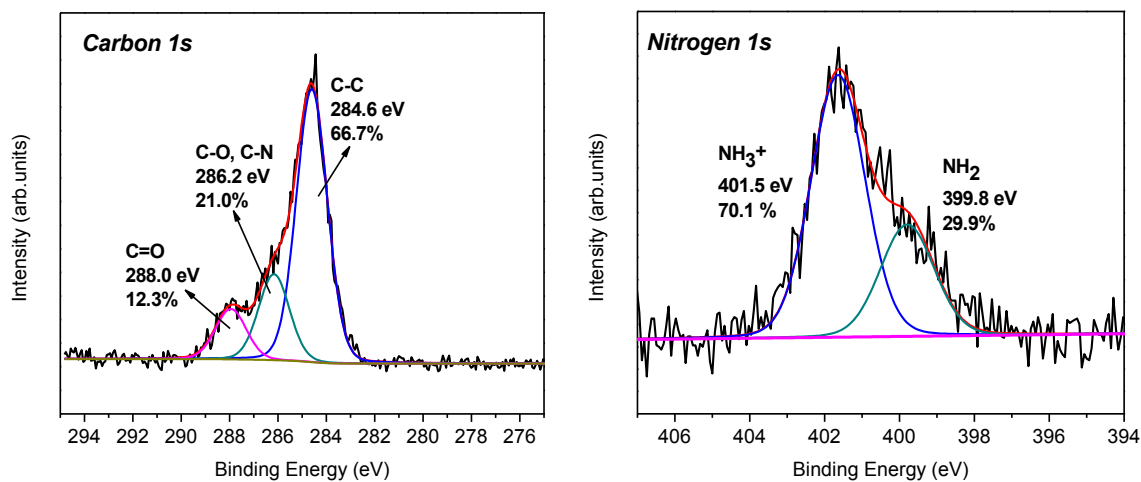


**Figure B5.** C1s (left) and N1s (right) core level X-ray photoemission spectra of carbon dots.

	Atomic Percentage %	Error %
<b>Carbon</b>	<b>63.5</b>	<b>2.5</b>
<b>Oxygen</b>	<b>29.0</b>	<b>0.6</b>
<b>Nitrogen</b>	<b>7.5</b>	<b>0.7</b>



**Figure B6.** Images of an aqueous dispersion of C-dots with room lights on (left), room lights off but UV illumination on at 254 nm (center) and 365 nm (right).

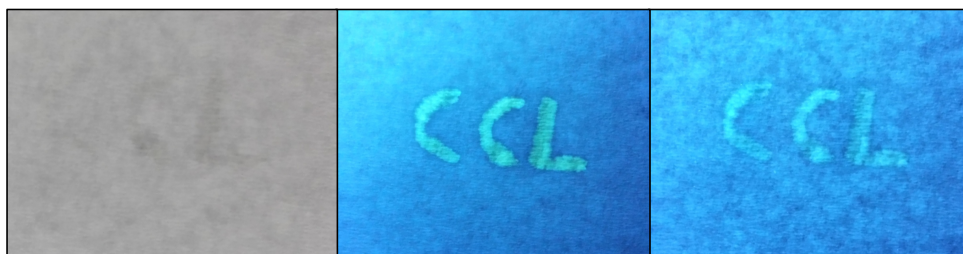


**Figure B7.** Images of C-dots deposited on an available commercial filtration paper with room lights on (left), room lights off but UV illumination at 254 nm (center) and 365 nm (right).

### **B.3 References of Appendix B**

1. Bourlinos, A. B.; Trivizas, G.; Karakassides, M. A.; Baikousi, M.; Kouloumpis, A.; Gournis, D.; Bakandritsos, A.; Hola, K.; Kozak, O.; Zboril, R.; Papagiannouli, I.; Aloukos, P.; Couris, S. *Carbon* **2015**, 83, 173-179.
2. Bourlinos, A. B.; Georgakilas, V.; Bakandritsos, A.; Kouloumpis, A.; Gournis, D.; Zboril, R. *Materials Letters* **2012**, 82, 48-50.
3. Bourlinos, A. B.; Bakandritsos, A.; Kouloumpis, A.; Gournis, D.; Krysmann, M.; Giannelis, E. P.; Polakova, K.; Safarova, K.; Hola, K.; Zboril, R. *J. Mater. Chem.* **2012**, 22, (44), 23327-23330.
4. Qu, S.; Wang, X.; Lu, Q.; Liu, X.; Wang, L. *Angewandte Chemie International Edition* **2012**, 51, (49), 12215-12218.
5. Peng, H.; Travas-Sejdic, J. *Chemistry of Materials* **2009**, 21, (23), 5563-5565.
6. Zhou, J.; Booker, C.; Li, R.; Zhou, X.; Sham, T.-K.; Sun, X.; Ding, Z. *Journal of the American Chemical Society* **2007**, 129, (4), 744-745.
7. Yang, Y.; Cui, J.; Zheng, M.; Hu, C.; Tan, S.; Xiao, Y.; Yang, Q.; Liu, Y. *Chem. Commun.* **2012**, 48, (3), 380-382.
8. Himaja, A. L.; Karthik, P. S.; Singh, S. P. *The Chemical Record* **2015**, 15, (3), 595-615.
9. Xu, M.; He, G.; Li, Z.; He, F.; Gao, F.; Su, Y.; Zhang, L.; Yang, Z.; Zhang, Y. *Nanoscale* **2014**, 6, (17), 10307-10315.
10. Moulder, J. K.; Stickle, W. F., *Handbook of X-ray photoelectron spectroscopy*. Physical Electronics, Inc.: 1995.

## Chapter 6

# Germanane: improved synthesis and application as antimicrobial agent

Over the last decade new families of two-dimensional materials have become the focus of scientific research, owing to their unique physiochemical properties and structure characteristics. The rise of inorganic 2D materials beyond graphene promises a new nanotechnology era for a diverse range of high efficiency applications in electronics, sensing, catalysis, energy production and storage as well as the biomedical sector. Germanane, a graphane analogue, has attracted significant interest due to its optoelectronic properties, however environmental and biological effects of germanane have not been studied yet. Here we report a new and facile approach for the production of germanane and investigate its antimicrobial activity for first time. Exfoliated germanane nanosheets were deposited on various substrates using a simple bottom-up procedure based on the Langmuir-Schaefer technique in order to fabricate homogeneous and dense monolayers. The results for one Gram-negative bacterial strain (*Escherichia coli*) and two Gram-positive bacterial strains (*Brevibacterium* and *Corynebacterium*) revealed the unique antimicrobial activity of germanane nanosheets for all three strains and thereby identified germanane thin films as high efficiency antimicrobial coatings.

---

This chapter is based on the articles: "Synthesis of 2D germanane (GeH): a new, fast and facile approach", by T. Giousis, G. Potsi, A. Kouloumpis, K. Spyrou, N. Chalmpes, K. Dimos, M. Antoniou, G. Papavassiliou, A. Bourlinos, H. J. Kim, H. Stamatias, G. Blake, D. Gournis, P. Rudolf (*to be submitted*) and "Extraordinary antimicrobial activity of germanane monolayer films", by A. Kouloumpis, N. Vourvou, N. Chalmpes, T. Giousis, P. Katapodis, H. Stamatias, P. Rudolf, D. Gournis (*to be submitted*).

## 6.1 Introduction

The emergence of infectious diseases or antibiotic-resistant bacterial strains increased over the last years renders the development of new antimicrobial drugs or antimicrobial coatings crucial. In order to maintain a sterile environment in industry or in health care institutions, a reduction or elimination of bacterial attachment is required. Significant efforts have been focused on the fabrication or improvement of surfaces with antimicrobial action - not only for health-related aims but also in view of keeping them clean by preventing the growth of microorganisms.<sup>1, 2</sup> Antimicrobial surfaces are widely used for a variety of applications in hospitals,<sup>3</sup> in the food<sup>4-6</sup> and clothing industry<sup>7-9</sup> or even at home. The antibacterial action can be induced by the surface roughness<sup>10, 11</sup> (textile surfaces) as well as by physical<sup>12</sup> or chemical effects achieved by functionalizing,<sup>13-17</sup> derivatizing<sup>18, 19</sup> or polymerizing<sup>20-26</sup> the surfaces. Antibacterial coatings<sup>25, 27-33</sup> include a plethora of materials like titanium,<sup>21, 34, 35</sup> hydroxyapatite,<sup>36-44</sup> fluoride ion,<sup>45-49</sup> silver nanoparticles<sup>27, 50-56</sup>, clays,<sup>57, 58</sup> carbon-based nanomaterials<sup>59-62</sup> (graphene,<sup>63-65</sup> nanotubes,<sup>59, 66-69</sup> fullerenes,<sup>70</sup> carbon-dots,<sup>71, 72</sup>) and most recently transition metal dichalcogenides (TMDs) like MoS<sub>2</sub>.<sup>73</sup> The exact interactions of 2D nanomaterials with bacterial cells are not yet clear in all cases but various interactions that cause damage to cell membranes and lead to a release of intracellular contents have been identified.<sup>74, 75</sup> The rapid growth of nanotechnology has opened new routes for thin films preparation by using a diversity of deposition methods such as plasma deposition and polymerization methods,<sup>27, 31</sup> layer-by-layer (LbL) assembly,<sup>28</sup> and (modified) Langmuir-Blodgett (LB) techniques<sup>64, 76, 77</sup> Despite the multitude of approaches for the formation of antimicrobial films and coatings, the most common problems<sup>78-80</sup> still encountered are short-term stability and non-uniformity of the films; additionally the preparation methods are often not easily transferable to an industrial environment.

After the discovery of graphene in 2004, many other 2D materials have been isolated and studied in less than a decade.<sup>81</sup> This family includes not only carbon materials but also transition metal dichalcogenides, boron nitride, black phosphorus or phosphorene and layered metal oxides, just to name a few.<sup>81, 82</sup> Because of the remarkable electronic and optoelectronic properties of these 2D solids, a new generation of superconductors, semiconductors, metallic materials and insulators



can be developed,<sup>83</sup> which in turn open new prospects for a variety of applications including high performance sensors and transistors, electronics, catalysis, gas separations and storage.<sup>82</sup>

Germanane (GeH), the germanium graphane-analogue (hydrogen-terminated germanium multilayer) is especially interesting in this context since theory predicts extraordinary properties such as a direct band gap (approximately 1.4 eV)<sup>84, 85</sup> and an electronic mobility that exceeds  $18.000 \text{ cm}^2 \text{ V}^{-1} \text{ s}^{-1}$ , five times higher than that of crystalline germanium and hence an outstanding potential for electronic and optoelectronic applications.<sup>86, 87</sup> Although these remarkable physical and chemical properties of germanane place it in the top group with regards to potential applications, its potential for bioapplications has not been explored yet.

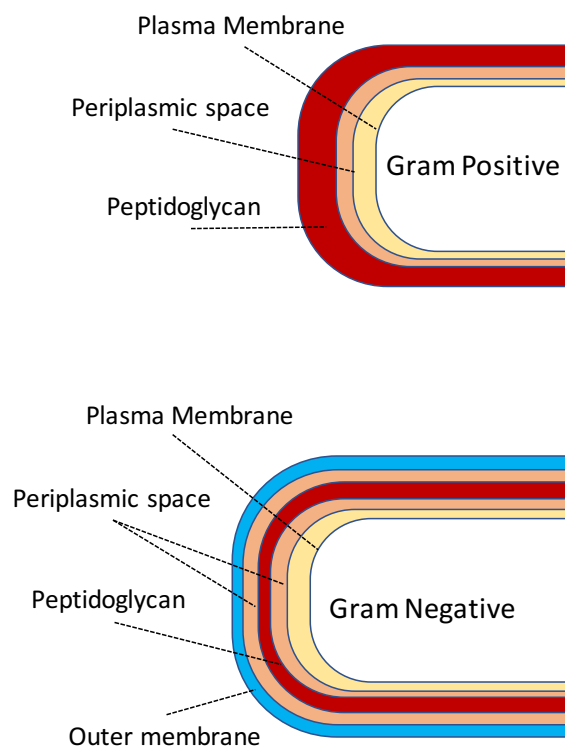
Recently germanane crystals (GeH) have been successfully synthesized from the topochemical deintercalation of  $\beta$ -CaGe<sub>2</sub> layered Zintl phase using HCl acid.<sup>86, 87</sup> The synthetic protocols reported so far use various acids (HCl, HBr, HI or acetic acid) at different temperatures (from -40 to 25 °C), requiring long reaction times (between 5 to 14 days).<sup>88</sup> In this work high quality germanane was synthesized by the topotatic deintercalation of  $\beta$ -CaGe<sub>2</sub> in aqueous HF solution (38% w/w) at room temperature for a few minutes (or even a few seconds).

To study the antimicrobial activity of germanane, coatings of this new material on a substrate suitable for cell growth were produced. Towards this aim here we describe a facile and low cost Langmuir-Schaefer (LS) deposition approach for the production of germanane monolayers and few layers, with precise control of the packing of GeH nanosheets in 2D arrays. Germanane is highly dispersible in ethanol and dimethylformamide (DMF) and easily separates into single nanosheets by liquid exfoliation in these solvents, while it is less dispersible in H<sub>2</sub>O. Such dispersions were injected at the air-water interphase of the Langmuir-Blodgett trough to form a floating monolayer on top of the water. Subsequently a compression of the GeH nanosheets with the help of the movable barriers of the Langmuir-Blodgett trough lead to a dense Langmuir layer.<sup>89</sup> Uniform monolayers of germanane with high surface coverage were transferred to hydrophilic substrates by horizontal dipping of the latter, a technique also called Langmuir Schaefer (LS) technique method.

To understand our choice of bacteria for this study, it is maybe useful for the reader to learn something about the differences between bacilli. In 1884 Christian Gram developed a special technique of staining bacteria (Gram staining or Gram's method) in order to make them more visible under microscopic examination; this method lead to a classification of bacteria based on the colour the sample exhibits. The stain is a weakly alkaline solution of crystal violet or a gentian violet.<sup>90</sup> Bacteria with a thick layer of peptidoglycan can retain the crystal violet dye and are called Gram-positive bacteria. Gram-negative bacteria do not retain the violet dye and are coloured red or pink<sup>90</sup> but that is not the only difference. The structural characteristics of Gram-negative and Gram-positive bacteria are shown in Scheme 6.1 while their cell wall differences are summarized in Table 6.1.

**Table 6.1.** Difference in the cell wall of Gram-negative and Gram-positive bacteria.

	Gram negative	Gram positive
Gram reaction	Do not retain the dye colour after washing with alcohol or acetone	Remain coloured with Gram staining even after washing with alcohol or acetone
Peptidoglycan layer	Thin (single-layered)	Thick (multi-layered)
Teichoic acids	Absent	Present
Periplasmic space	Present	Absent
Outer membrane	Present	Absent
Lipid & lipoprotein content	High (due to presence of outer membrane)	Low (acid-fast bacteria have lipids linked to peptidoglycan)
Susceptibility to anionic detergents	Low	High
Cell wall Composition	The cell wall is 70-120 Å thick and built up from two layers. The lipid content is 20-30% (High) Murein content is 10-20% (Low)	The cell wall is 100-120 Å thick and built up from a single layer. The Lipid content of the cell wall is low Murein content is 70-80% (Higher)
Antibiotic Resistance	Resistant to antibiotics	Susceptible to antibiotics
Mesosome	Mesosome is less prominent	Mesosome is more prominent



**Scheme 6.1.** Structure characteristics of Gram-negative (bottom) and Gram-positive (top) bacteria.

Therefore to get an idea of the antimicrobial activity of germanane with respect to different types of bacteria, we investigated three strains as models, namely one Gram-negative bacterial strain (*Escherichia coli*) and two Gram-positive strains (*Brevibacterium* and *Corynebacterium*). *Escherichia coli* is a facultative anaerobe, rod-shaped bacterium of the genus *Escherichia*, found in the normal flora of the lower intestine of endothermic organism. Most of *E. coli* bacterial strains are harmless and have a double role in the intestine, they produce vitamin K<sup>91</sup> and prevent the colonization of the intestine by pathogenic bacteria.<sup>92, 93</sup> Some types of *E. coli* can cause food poisoning in their hosts. *Brevibacterium* and *Corynebacterium* belong to the order of Actinomycetales and are widely present in animal and human microbiota. *Corynebacterium* is a club-shaped bacillus; *Brevibacterium* is a rod-shaped bacterium, which can change the cell morphology during growth and become granules, a characteristic depending sometimes on the nutrients of the growth medium. *Brevibacterium* and *Corynebacterium* are harmless but some types can cause food contamination as well as human diseases; *i.e.* Diphtheria is caused by *C. diphtheriae*.

## 6.2 Experimental Section

### 6.2.2 Materials

Ethylenediaminetetraacetic acid (EDTA,  $\geq 99\%$ ) was purchased from Fluka. Ge powder ( $\geq 99\%$ ), Ca granules ( $\geq 99\%$ ), acetone, methanol, ethanol and dimethylformamide (DMF) were purchased from Sigma-Aldrich. Hydrogen fluoride (38%) was purchased from Merck. Ultrapure deionized water (18.2 M $\Omega$ ) produced by a Millipore Simplicity® system was used throughout. The Si-wafer (P/Bor, single side polished purchased from Si-Mat) and mylar (thickness of 0.35 mm, purchased from Sabic Innovate Plastics BV Snij-Unie HiFi) substrates were cleaned prior to use by 15 min ultra sonication in water and ethanol. All reagents were of analytical grade and were used without further purification.

### 6.2.3 Synthesis of Germanane<sup>4</sup>

Germanane (GeH) was synthesized by the topotactic deintercalation of  $\beta$ -CaGe<sub>2</sub> in aqueous HF (38% w/w) (12M) at room temperature. The initial phase of  $\beta$ -CaGe<sub>2</sub> was formed by sealing stoichiometric ratios 1:1 of calcium and germanium in a cylindrical alumina crucible (external diameter of 11 mm), enclosed in an evacuated fused quartz tube (internal diameter of 12 mm). The mixing of the two metals and the filling of the crucible took place in a glove box under nitrogen atmosphere. The sealed quartz tube was placed in a box furnace with the following temperature path:

- I. Heating to 1025 °C within 2 h at a rate of 8.3 °C/min
- II. Homogenization at 1025 °C for 20 h.
- III. Slow cooling to 500 °C at a rate of 0.1 °C/min.
- IV. Reach the room temperature at a rate of 0.2 °C/min.

Small crystals (2-6 mm) of CaGe<sub>2</sub> were collected and treated with an aqueous HF solution (38% w/w) (12M) at room temperature under stirring for 15 min. The resulting material contained apart from GeH also salts (mainly CaF<sub>2</sub>) that were removed by ethylenediaminetetraacetic acid (EDTA) addition. The final material

---

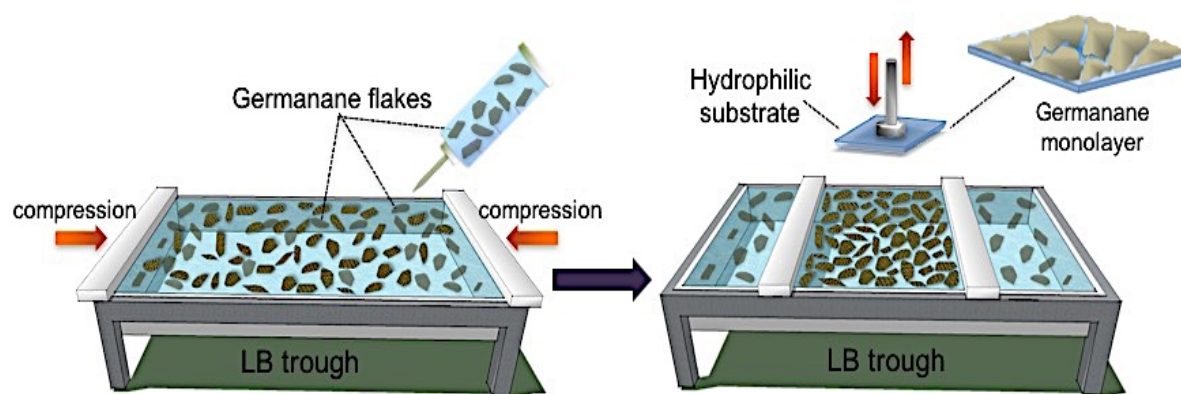
<sup>4</sup> Germanane samples were provided by Theodosios Giousis (University of Ioannina, Greece)

(GeH) separated by centrifugation, washed several times with distilled water (and methanol at the end) and finally left to dry under vacuum.

#### 6.2.4 Preparation of germanane monolayers

Germanane dispersions in ethanol and DMF ( $0.04 \text{ mg mL}^{-1}$ ) were prepared for the LB assembly. The dispersions were sonicated for 30 min using a probe ultrasonic sonicator (Ultrasonicator biobase UCD150L, 150 W). A centrifuge for 15 min at 1000 rpm was performed to purify the dispersions by removing aggregates and larger germanane flakes.

A Langmuir Blodgett trough (KSV 2000 Nima Technology model) was cleaned with ethanol and distilled-deionized water. Ultra pure water ( $18.2 \text{ M}\Omega$ ) was used as subphase. A Pt Wilhelmy plate was used to monitor the surface pressure during the compression and deposition procedures. Ethanol and DMF dispersions of germanane (1-15 mL) were slowly spread onto the water surface using a glass syringe. After a waiting time of 30 min to allow for the solvent to mix with the water, the germanane layers were compressed at a rate of  $5 \text{ mm min}^{-1}$  until the target surface pressure of  $10 \text{ mN m}^{-1}$  was reached, forming dense germanane Langmuir films<sup>94, 95</sup> as shown in Scheme 6.2. The GeH Langmuir films were transferred onto hydrophilic substrates by the LS technique (horizontal dipping), with downward and lifting speeds of  $10$  and  $5 \text{ mm min}^{-1}$ , respectively. After each deposition step the substrates were rinsed several times by dipping into ultrapure water (to remove any weakly attached GeH flakes that remained from the deposition step) and dried with nitrogen flow.<sup>94, 95</sup> Hydrophilic surfactant-treated Si-wafer and mylar substrates (as reported in Chapter 5, see Appendix B) were used for the LS deposition.



**Scheme 6.2.** Schematic representation of the LS procedure followed for the production of germanane monolayers.

### 6.2.5 Bacterial strains and growth media<sup>5</sup>

The bacteria strains *Escherichia coli* (ECO), *Corynebacterium glutamicum* (COR) and *Brevibacterium lactofermentum* (BRE) were grown in Luria-Bertani (L-B) broth at 37 °C with rotary shaking (180 rpm) until the stationary growth phase (approximately 20 h of incubation) was reached. Exponential-growth-phase cultures of bacteria were grown as described above but cells were harvested after 4 h. The cultivated bacteria were washed three times by normal saline solution (0.9 % NaCl w/v) before use.

### 6.2.6 Preparation of bacteria and treatment of germanane<sup>6</sup>

The antibacterial activity of GeH dispersions was studied with the microtiter plate method, adapted with some modifications to this nanomaterial.<sup>96</sup> Bacterial cell suspensions were diluted with a normal saline solution to obtain cell samples containing  $10^6$  CFU/mL. 200  $\mu$ L of bacteria cells were transferred into a sterile 96-well microplate. GeH were added aseptically in each micro-culture at a final concentration of 50  $\mu$ g/mL and then the microplates were shaken at 180 rpm at 37 °C for 20 h. In a control test, the bacteria suspension was put into the wells of the microtiter plate but without the addition of antimicrobial material. Subsequently, 50  $\mu$ L from each well was transferred aseptically into a new microplate diluted with

<sup>5</sup> Provided by Prof. Haralambos Stamatis (University of Ioannina, Greece)

<sup>6</sup> The preparation of bacteria and the treatment of germanane were performed by Nikolina Vourvou (University of Ioannina, Greece)

200  $\mu\text{L}$  fresh L-B medium. The microplates were agitated by the microplate reader and then incubated at  $37 \pm 1$   $^{\circ}\text{C}$  for 20 h. Turbidity was measured as absorbance at 600 nm. Growth inhibition (%) at different time intervals was calculated using the following equation:

$$\text{Growth inhibition (\%)} = \frac{\text{OD}_{\text{control}} - \text{OD}_{\text{GeH}}}{\text{OD}_{\text{control}}} \cdot 100$$

where  $\text{OD}_{\text{GeH}}$  is the absorbance of the microculture at 600 nm after exposures in GeH nanomaterial at the specified time intervals and  $\text{OD}_{\text{control}}$  is the absorbance of the control respectively. To confirm reproducibility, each test was repeated at least three times.

In addition, we also investigated the antibacterial activity of GeH thin films deposited on mylar substrates by means of viable cells survival on GeH surfaces.<sup>97</sup> Aliquots of 50  $\mu\text{L}$  bacterial suspension containing  $10^5$ ,  $10^6$  and  $10^7$  CFU/mL were applied as a standing droplet on GeH films (2 cm x 2 cm). Control samples were placed on the same substrate without the GeH layer. To avoid contamination from the laboratory environment, the samples were incubated in sterile Petri dishes at  $37^{\circ}\text{C}$  for 20 h before being washed extensively with an autoclaved PBS (phosphate-buffered saline) buffer. In detail, eluents were serially diluted in the PBS buffer and plated on L-B agar for aerobic incubation at  $37$   $^{\circ}\text{C}$ . After 20 h, the bacterial colonies on each plate were counted. The viable cell number was calculated as colony forming units per milliliter (CFU/mL). The antibacterial activity was calculated as the equation below:

$$\text{Bacterial Inhibition (\%)} = \frac{N_{\text{control}} - N_{\text{GeH}}}{N_{\text{control}}} \cdot 100$$

where  $N_{\text{GeH}}$  is the number of viable cells that survived on the GeH-covered substrate and  $N_{\text{control}}$  is the number of viable cells that survived on the control substrate. To confirm reproducibility, each test was repeated at least three times.

## 6.3 Results and Discussion

### 6.3.1 Structural and morphological characterization of germanane

Initially we characterized the produced GeH by FT-IR, Raman and  $^1\text{H}$  MAS NMR spectroscopies. The spectra were collected as described in Appendix A and are presented in Figure 6.1. Figure 6.1a shows  $^1\text{H}$  MAS NMR spectra of the GeH sample at room temperature, as well as upon thermal treatment at various temperatures (up to 275 °C). At each temperature the sample was heated for two hours, subsequently cooled to room temperature in vacuum and then shielded into the rotor for performing the NMR experiment. In the case of the unheated sample (room temperature) the  $^1\text{H}$  MAS NMR spectrum was dominated by a peak at 5.6 ppm, attributed to the Ge-H. A very small quantity of adsorbed water (at 4.8 ppm) cannot be excluded. A Ge-H resonance at 5.16 ppm has been previously reported in 2,2'-diphenylene germane.<sup>98</sup> At elevated treatment temperatures part of the GeH hydrogen dissociates as deduced from the strong signal decrease. However, a big part of the signal remains not only upon heating at 200 °C but even at the highest temperature of 275 °C. At the same time, a slight shift of the peak to lower chemical shift values is observed, especially at 275 °C, which is indicative of slightly more effective electron shielding. In the Raman spectrum (Figure 6.1b) of the synthesized powder flake a characteristic peak associated with Ge-H bond is observed at 288  $\text{cm}^{-1}$ <sup>87</sup> that clearly reveals the presence of this bond in the studied material, thus confirming its composition. Moreover, the FTIR spectrum (Figure 6.1c) of germanane shows a strong peak at 2000  $\text{cm}^{-1}$  due to the Ge-H stretching vibration, while peaks at 477 and 575  $\text{cm}^{-1}$  are assigned to multiple wagging modes of Ge-H and<sup>86, 99</sup> strong peaks at 770 and 825  $\text{cm}^{-1}$  to H-Ge-H bending modes from neighbouring Ge atoms at the edges of the crystalline germanane layer and/or Ge vacancies within the layered germanane lattice.<sup>86</sup> FTIR spectroscopy therefore confirms the hydrogen termination of the germanium atoms.



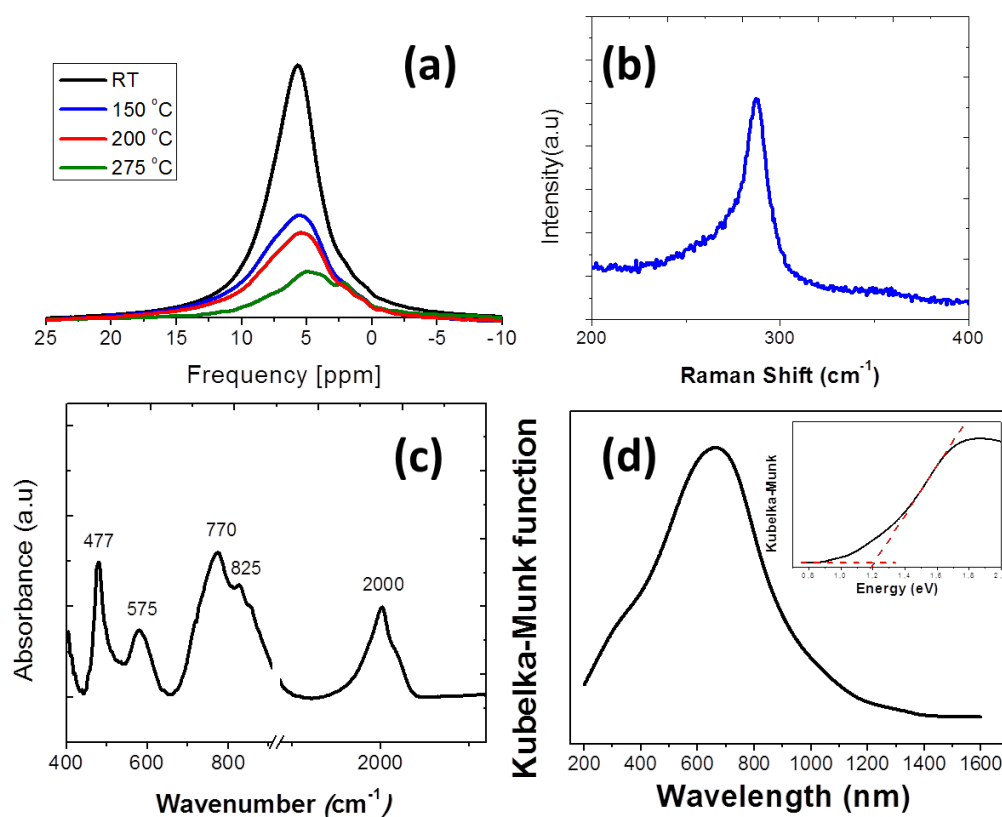


**Figure 6.1.** (a)  $^1\text{H}$  MAS NMR of GeH sample before and after thermal treatment at various temperatures (150, 200 and 275 °C). (b) Raman and (c) FTIR spectrum of GeH. (d) DRA spectrum of GeH plotted in Kubelka-Munk function versus wavenumbers and (e) photon energy (inset).

The UV-Vis-NIR diffuse reflectance spectrum of germanane is presented in Figure 6.1d. The reflectance spectrum was converted to Kubelka-Munk function,  $F(R_\infty)$  and plotted against wavenumbers (nm) and photon energy (eV). The sample shows a strong light absorption in the whole visible light region. The line tangent to the point of inflection of the curve (Figure 6.1d inset) determines the band gap ( $E_g$ ) as close to 1.2 eV, a value lower to that reported in the literature for germanane synthesized using HCl (1.58 eV).<sup>86, 100 87</sup>

A platelet-like morphology was revealed for the produced GeH as shown in Scanning Electron Microscopy (SEM) picture of Figure 6.2 (top). Flakes of several  $\mu\text{m}$  are visible that are fully covered with calcium fluoride salt as a byproduct of the reaction.

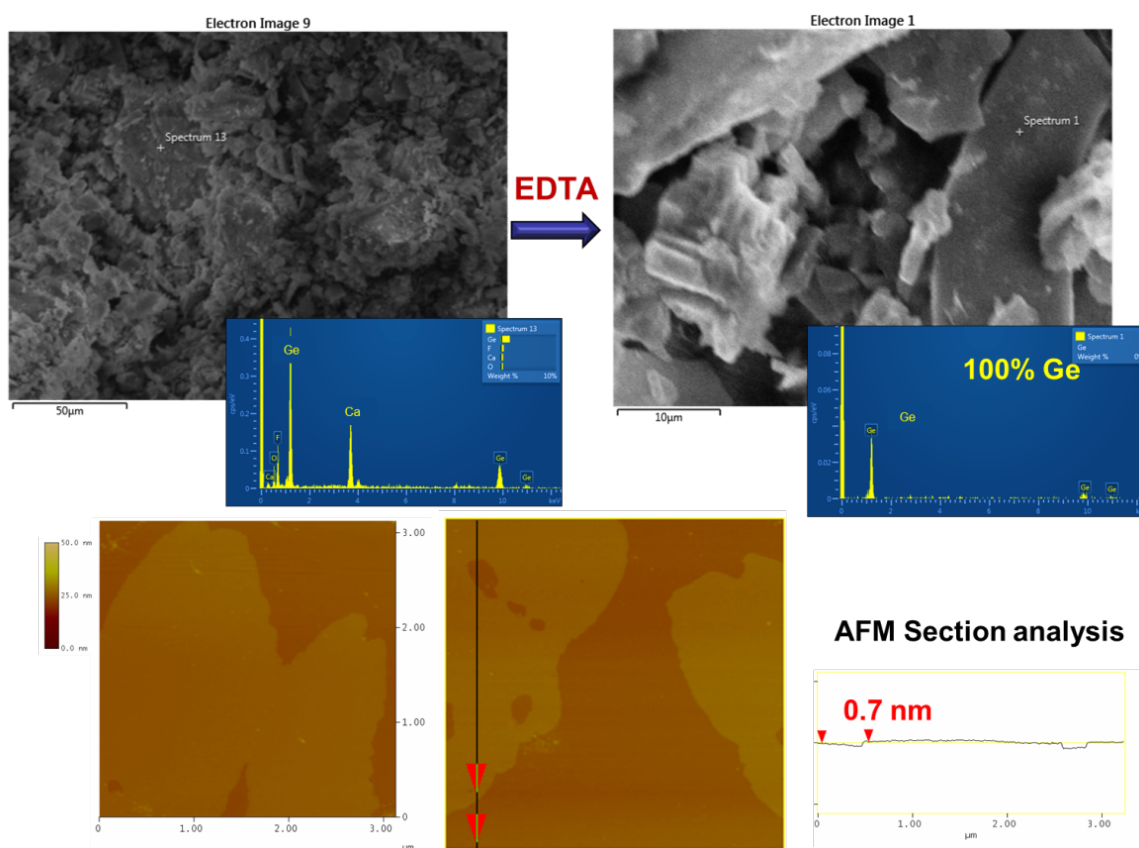


**Figure 6.2.** Top: SEM images (and corresponding EDX spectra) of germanane product before and after treatment with EDTA. Bottom: AFM images (including section analysis) of germanane films prepared by drop-casting of ethanol dispersions.

In order to remove the residual  $\text{CaF}_2$ , the material was treated with a saturated aqueous solution of EDTA, filtered and washed several times with water and methanol. The resulting product is a layered material consisting of germanium and free of any residual salt as revealed from energy dispersive X-ray spectroscopy (EDX) where no Ca and F signals can be detected. A first idea about the quality of the produced GeH can also be gained from representative AFM height images of GeH layers deposited on a Si wafer by drop-casting from an ethanol dispersion, shown in Figure 6.2 (bottom). The topographic image reveals GeH flakes, which are several micrometers large and have an average thickness of 0.7 nm as determined from the cross-section analysis. This value is very close to the height of a single germanane layer (0.6 nm).<sup>86</sup>

### 6.3.2 Structural control and characterization of GeH monolayers

To be able to deposit GeH by the Langmuir-Schaefer technique, we first have to prove that it is possible to form stable Langmuir films at the subphase surface in the Langmuir-Blodgett trough. To this end we recorded  $\pi$ -A isotherms during the compression of Langmuir films formed after different amounts of ethanol dispersions of exfoliated germanane were introduced at the air-water interphase. The  $\pi$ -A isotherms for injections ranging from 1 to 15 mL are shown in Figure 6.3. The curves show a change in slope when the pressure is such that a phase transition in the Langmuir film of GeH sheets occurs during the compression process, first from a 2D gas to a condensed liquid and then to solid state.<sup>94, 95</sup> More specifically, following the isotherm from right to left, the first discontinuity is the lift-off area, defined as the molecular area where the surface pressure becomes different from zero; here the flakes start to order and therefore to interact as a two-dimensional liquid. For the  $\pi$ -A isotherm recorded when adding a small amount of GeH dispersion (1 mL) to the water surface, the lift-off area is  $14 \text{ \AA}^2$  and the maximum surface pressure reaches the value of  $12 \text{ mN m}^{-1}$ .

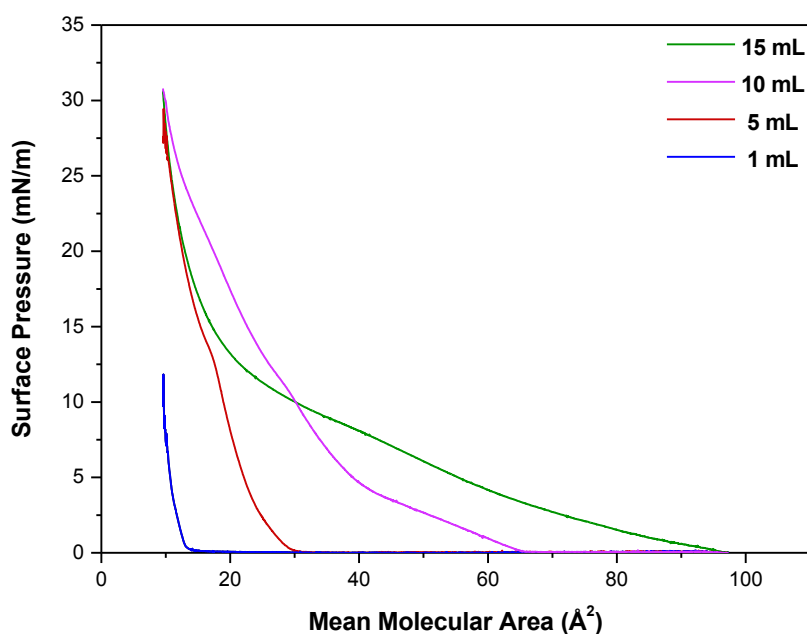


**Figure 6.3.**  $\pi$ -A isotherms of floating GeH nanosheets in water surface for different ethanol dispersion volumes (1 to 15 mL).

The phase transitions of the GeH Langmuir films are clearly observed (by the change of the isotherm slope) when the dispersion volumes in the water surface are increased to 5 mL and 10 mL, resulting higher lift-of areas of 30 Å<sup>2</sup> and 63 Å<sup>2</sup> respectively, while the surface pressure reaches a maximum value of 31 mN m<sup>-1</sup> in both cases. Moreover further increasing the GeH dispersion volume to 15 mL causes an absence of the gas phase and therefore suggests that domains of higher density have formed at the water/air interphase. From these results we can clearly conclude that stable Langmuir films are formed whose density at a certain surface pressure depends on the amount of GeH flakes injected at the water surface.

In addition to studying the stability of the Langmuir films when GeH flakes were delivered to the water surface in the Langmuir-Blodgett trough in the form of a dispersion in ethanol, we also collected  $\pi$ -A isotherms of germanane delivered in DMF dispersions. Also in this case no surfactant was employed. The results for different amounts of dispersion ranging from 1 to 15 mL are shown in Figure 6.4. As for case of the ethanol dispersion, the curves show a change in slope corresponding to the phase transitions of Langmuir film of GeH nanosheets during the compression process, from 2D gas to condensed liquid and then to the solid state.<sup>94, 95</sup> For the smallest amount of GeH dispersion (1 mL) spread on the water surface, the lift-off area is 20 Å<sup>2</sup> and the maximum surface pressure reaches the value of 18 mN m<sup>-1</sup>. The phase transitions of the Langmuir film are clearly observed when the dispersion volume is increased to 5 mL resulting in a 57 Å<sup>2</sup> lift-of area and a surface pressure that reaches the maximum value of 24 mN m<sup>-1</sup>. The absence of the gas phase is observed for larger dispersion volumes of GeH injected at the water surface (10 and 15 mL), suggesting domains of higher density form before the compression is started.

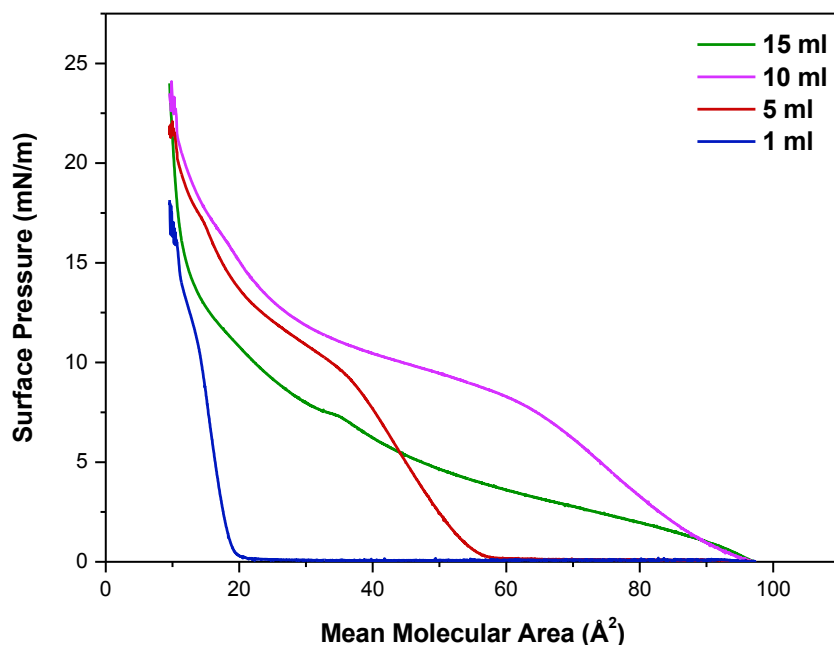


**Figure 6.4.**  $\pi$ -A isotherms for Langmuir films of floating GeH nanosheets at the water surface, recorded for different volumes of the injected DMF dispersions (1 to 15 mL)

The success of the transfer of the GeH Langmuir films to the hydrophilic Si-wafer with the LS technique was proven by atomic force microscopy. Representative AFM height images of GeH Langmuir Schaefer films deposited at different surface pressures are shown in Figure 6.5. The topographic images show that the surface coverage of the substrate is higher as the surface pressure increases. More specifically, after the addition of GeH dispersion (5 mL) at the water surface and before the compression starts (at 0 mN m<sup>-1</sup> surface pressure) single nanosheets with well defined edges and widely spaced one from the other are observed. This again testifies to the formation of a floating layer (without the need for any surfactant) at the air-water interphase (Figure 6.5a). When the compression was started and the floating film reached the surface pressure of 2 mN m<sup>-1</sup> when the transfer was performed, the LS film consists of isolated GeH flakes with an empty space between them (Figure 6.5b).

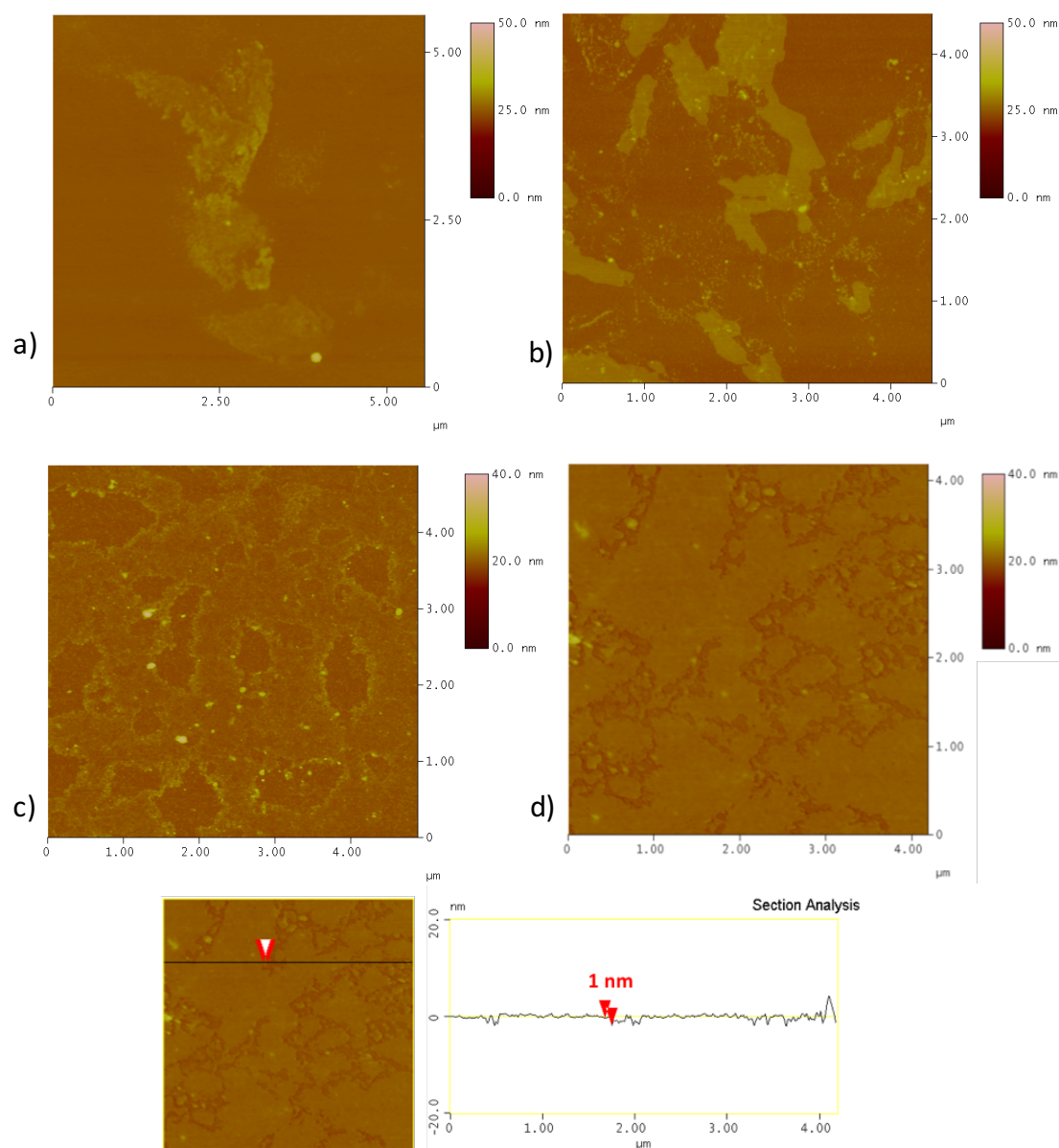


**Figure 6.5.** AFM height images and cross section analysis of GeH layers deposited by the Langmuir Schaefer method on functionalized Si wafers at surface pressures of: (a)  $0 \text{ mN m}^{-1}$ , (b)  $2 \text{ mN m}^{-1}$ , (c)  $6 \text{ mN m}^{-1}$  and (d)  $10 \text{ mN m}^{-1}$ .

If the transfer takes place at higher surface pressure ( $6 \text{ mN m}^{-1}$ ) the GeH nanosheets are almost in contact with each other, with some voids between them (Figure 6.5c). Still further compression of the floating layer to surface pressure of  $10 \text{ mN m}^{-1}$  before transfer results in a closely packed LS film where the GeH form a homogeneous and dense monolayer which covers  $\geq 80\%$  of the substrate. The average thickness of the GeH flakes is  $1 \text{ nm}$  as derived from topographical height profile (section analysis) corresponding to single germanane layers.<sup>86</sup> The

micrographs in Figure 6.5 conclusively prove that the Langmuir Schaefer method without the use of a surfactant allows for the homogeneous deposition of sparsely or closely packed GeH single layers on substrates, identifying this technique as an ideal tool for fabricating thin films of this new 2D material.

### 6.3.3 Antimicrobial activity of germanane<sup>7</sup>

The antibacterial activity of GeH was evaluated using *Escherichia coli* (ECO), *Corynebacterium glutamicum* (COR) and *Brevibacterium lactofermentum* (BRE) as model organisms. Overnight exposure of bacteria in aqueous GeH dispersions at a concentration of 50 µg/mL inhibits the bacteria growth by more than 80% during the first 6 h of growth for both Gram-negative and Gram-positive bacterial strains as shown in Figure 6.6. GeH exhibits higher antimicrobial activity against Gram-positive bacteria than against Gram-negative ones; probably the more complex cell wall of *E. coli* (see Table 6.1 and Scheme 6.1) acts as a barrier in antimicrobial effect.<sup>101</sup>

Similar results were obtained for GeH monolayers deposited on mylar substrates. More specifically, the antibacterial activity of GeH thin films was evaluated using the same model organisms but this time an antimicrobial drop-test was used and the ability of the exposed bacteria to form colonies in a Luria-Bertani growth medium was determined. The number of bacterial colonies grown on Luria Broth medium plates is shown in Figure 6.7.

---

<sup>7</sup> The results of germanane's antimicrobial activity were provided by Prof. Haralambos Stamatis (University of Ioannina, Greece) and Prof. Petros Katapodis (University of Ioannina, Greece).

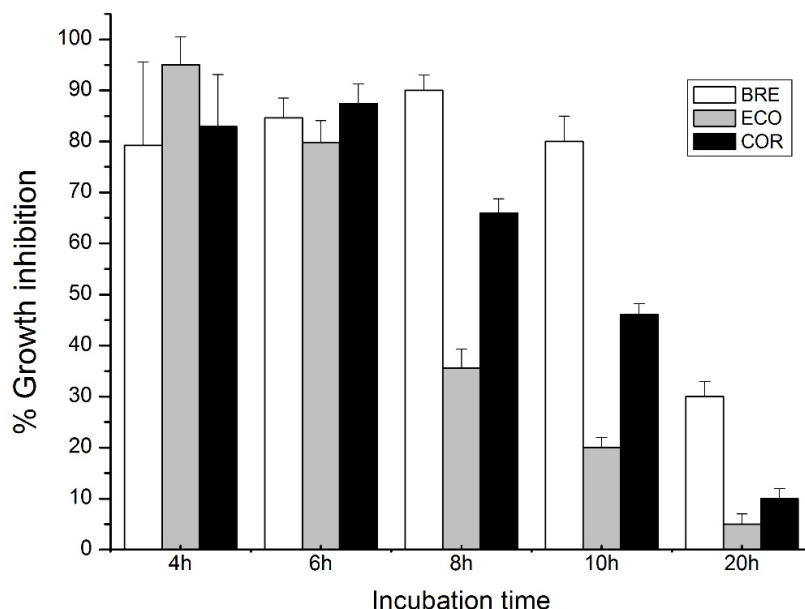


**Figure 6.6.** Antibacterial activity of GeH against gram-negative (*Escherichia coli*) and gram-positive (*Corynebacterium glutamicum*, *Brevibacterium sp.*) bacteria, after 20 h exposure.

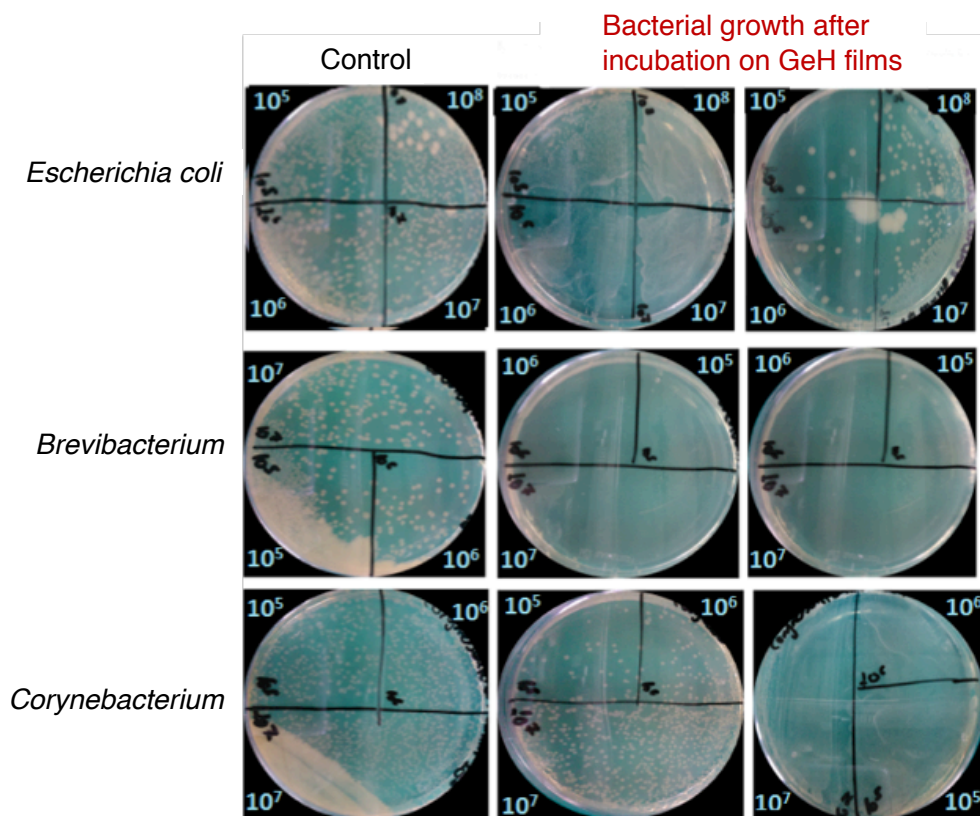


**Figure 6.7.** Typical images of bacterial growth after incubation of bacterial strains (*E. coli*, *Brevibacterium* and *Corynebacterium*) on germanane Langmuir-Schaefer films on functionalized Si wafer in a Luria Broth medium.



**Table 6.2.** Antibacterial activity of GeH Langmuir-Schaefer films against gram-negative (*Escherichia coli*) and gram-positive (*Corynebacterium glutamicum*, *Brevibacterium sp.*) bacteria, after 20 h exposure.

Strain	Bacterial inhibition of GeH films		
	Initial Inoculum		
	10 <sup>5</sup> (CFU/mL)	10 <sup>6</sup> (CFU/mL)	10 <sup>7</sup> (CFU/mL)
<i>Escherichia coli</i>	95%	80%	30%
<i>Corynebacterium glutamicum</i>	>99%	95%	60%
<i>Brevibacterium sp.</i>	>99%	>99%	>99%

The bacterial population for all bacterial strains is decreased after the incubation on GeH films while the antimicrobial effect of the films depends on the bacterial strain. The bacterial population for all bacterial strains decreased after the incubation on GeH thin films as shown in Table 6.2. The percentage of bacteria remaining viable after the exposure depends on the number of cells that was applied. When 10<sup>5</sup> CFU/mL were applied, the antimicrobial effect was more than 95% for all the strains. For higher bacterial populations from 10<sup>6</sup> to 10<sup>7</sup> CFU/mL the bacterial inhibition of the films depends on the bacterial strain. More specifically, the GeH films exhibit a remarkable antimicrobial activity against *Brevibacterium lactofermentum*, this effect is slightly lower for *C. glutamicum* strains and even more for *E. coli*, probably due to the more complex cell wall structure (see Table 6.1 and Scheme 6.1).

Although the antimicrobial mechanism of GeH nanosheets (as well as of other 2D materials like graphene oxide<sup>101</sup> and MoS<sub>2</sub><sup>73</sup>) is not clear yet, these results suggest that the cell wall of bacteria act as a barrier to the antimicrobial effect. Different authors attribute the antimicrobial action of 2D nanomaterials both to physical and/or chemical features.<sup>64, 101</sup> The atomically sharp edges of the nanosheets can pierce the cell membrane causing cell rupture. Possible chemical damage involves an oxidative stress either by the lipid peroxidation induced by the reactive oxygen species (ROS) of the nanomaterials or by ROS-independent oxidative stress,<sup>73</sup> which entails that nanomaterials may disturb or oxidize the cellular structure (without ROS production)<sup>73</sup> leading to cell membrane disintegration.

According to our microscopy studies, the GeH nanosheets have been deposited flat and uniform on the substrates by the LS method, forming homogeneous and closely packed monolayers suggesting that the robust antibacterial activity of the GeH should not have been observed if the sharp edges of the nanosheets were the main cause for rupture of the cell membrane.

## **6.4 Conclusions**

Germanane, a germanium graphane-analogue is a new inorganic 2D material not only with outstanding potential for (opto)electronic applications but can also be exploited for its environmental and biological properties. High quality germanane was synthesized by the topotatic deintercalation of  $\beta$ -CaGe<sub>2</sub> in aqueous HF solution (38% w/w) at room temperature for few minutes. A Langmuir-Blodgett trough was used to form germanane Langmuir films in the air-water interphase without the use of surfactants. The packing density of exfoliated germanane nanosheets could be easily controlled from sparsely spaced isolated sheets in a 2D gas to close-packed films. These Langmuir films could be efficiently transferred to a substrate using the Langmuir Schaefer technique, with perfect control over of coverage, uniformity and percentage of single-layer flakes, as confirmed by  $\pi$ -A isotherms and AFM measurements. The antimicrobial activity of GeH coatings and dispersions against one Gram-negative bacterial strain and two Gram-positive bacterial strains was investigated for first time, revealing that the bacterial populations incubated into germanane films were importantly decreased. More specifically, GeH thin films exhibit high effectiveness in antimicrobial activity against *E. coli* and *Corynebacterium* strains for 10<sup>5</sup> CFU/mL. In addition an extraordinary antimicrobial activity against *Brevibacterium* bacterial strain was revealed for all cell concentrations. GeH aqueous dispersions inhibit the bacterial growth for 6 h for both Gram-negative and Gram-positive bacteria. The large-scale and facile Langmuir-Schaefer assembly constitutes a novel method for the design and fabrication of uniform germanane monolayers that could be ideally used as a candidate

nanomaterial in diverse bio-applications such as high efficiency antimicrobial surfaces in hospitals and in the food industry.

## 6.5 References

1. Hasan, J.; Crawford, R. J.; Ivanova, E. P. *Trends in Biotechnology* **2013**, 31, (5), 295-304.
2. Mitchell, A.; Spencer, M.; Edmiston, C. *Journal of Hospital Infection* **2015**, 90, (4), 285-292.
3. Dancer, S. J. *European Journal of Clinical Microbiology and Infectious Diseases* **2011**, 30, (12), 1473-1481.
4. Irkin, R.; Esmer, O. K. *Journal of Food Science and Technology* **2015**, 52, (10), 6095-6111.
5. Bastarrachea, L. J.; Denis-Rohr, A.; Goddard, J. M. *Annual Review of Food Science and Technology* **2015**, 6, 97-118.
6. De Azeredo, H. M. C. *Trends in Food Science and Technology* **2013**, 30, (1), 56-69.
7. Liu, J.; Liu, C.; Liu, Y.; Chen, M.; Hu, Y.; Yang, Z. *Colloids and Surfaces B: Biointerfaces* **2013**, 109, 103-108.
8. Ashjaran, A.; Ghazi-Saeidi, R.; Yazdanshenas, E.; Rashidi, A. *World Academy of Science, Engineering and Technology* **2010**, 64, 8-11.
9. Fukuda, F.; Yamaguchi, H.; Higuchi, M. *Biocontrol Science* **2002**, 7, (2), 91-99.
10. McArthur, J. V.; Tuckfield, R. C.; Baker-Austin, C., Antimicrobial textiles. In *Handbook of Experimental Pharmacology*, 2012; Vol. 211, pp 135-152.
11. Sportelli, M. C.; Picca, R. A.; Cioffi, N., Nano-Antimicrobials Based on Metals. In *Novel Antimicrobial Agents and Strategies*, 2014; pp 181-218.
12. Asri, L. A. T. W.; Crismaru, M.; Roest, S.; Chen, Y.; Ivashenko, O.; Rudolf, P.; Tiller, J. C.; van der Mei, H. C.; Loontjens, T. J. A.; Busscher, H. J. *Advanced Functional Materials* **2014**, 24, (3), 346-355.
13. Karam, L.; Casetta, M.; Chihib, N. E.; Bentiss, F.; Maschke, U.; Jama, C. *Journal of the Taiwan Institute of Chemical Engineers* **2016**, 64, 299-305.
14. Emam, H. E.; Rehan, M.; Mashaly, H. M.; Ahmed, H. B. *Dyes and Pigments* **2016**, 133, 173-183.

15. Gomes, A. P.; Mano, J. F.; Queiroz, J. A.; Gouveia, I. C., Layer-by-layer assembly for biofunctionalization of cellulosic fibers with emergent antimicrobial agents. In *Advances in Polymer Science*, 2015; Vol. 271, pp 225-240.
16. Vukomanović, M.; Logar, M.; Škapin, S. D.; Suvorov, D. *Journal of Materials Chemistry B* **2014**, 2, (11), 1557-1564.
17. Alves, D.; Olívia Pereira, M. *Biofouling* **2014**, 30, (4), 483-499.
18. Carmona-Ribeiro, A. M.; de Melo Carrasco, L. D. *International Journal of Molecular Sciences* **2013**, 14, (5), 9906-9946.
19. Ghanbari, H.; Cousins, B. G.; Seifalian, A. M. *Macromolecular Rapid Communications* **2011**, 32, (14), 1032-1046.
20. Misdan, N.; Ismail, A. F.; Hilal, N. *Desalination* **2016**, 380, 105-111.
21. Zhang, L.; Ning, C.; Zhou, T.; Liu, X.; Yeung, K. W. K.; Zhang, T.; Xu, Z.; Wang, X.; Wu, S.; Chu, P. K. *ACS Applied Materials and Interfaces* **2014**, 6, (20), 17323-17345.
22. Mi, L.; Jiang, S. *Angewandte Chemie - International Edition* **2014**, 53, (7), 1746-1754.
23. Gour, N.; Ngo, K. X.; Vebert-Nardin, C. *Macromolecular Materials and Engineering* **2014**, 299, (6), 648-668.
24. Raj, P. A.; Dentino, A. R. *Future Medicinal Chemistry* **2013**, 5, (14), 1635-1645.
25. Arora, S.; Yadav, V.; Kumar, P.; Gupta, R.; Kumar, D. *International Journal of Pharmaceutical Sciences Review and Research* **2013**, 23, (2), 279-290.
26. Timofeeva, L.; Kleshcheva, N. *Applied Microbiology and Biotechnology* **2011**, 89, (3), 475-492.
27. Nikiforov, A.; Deng, X.; Xiong, Q.; Cvelbar, U.; Degeyter, N.; Morent, R.; Leys, C. *Journal of Physics D: Applied Physics* **2016**, 49, (20).
28. Zhu, X.; Jun Loh, X. *Biomaterials Science* **2015**, 3, (12), 1505-1518.
29. Swartjes, J. J. T. M.; Sharma, P. K.; VanKooten, T. G.; Van DerMei, H. C.; Mahmoudi, M.; Busscher, H. J.; Rochford, E. T. J. *Current Medicinal Chemistry* **2015**, 22, (18), 2116-2129.
30. Salwiczek, M.; Qu, Y.; Gardiner, J.; Strugnell, R. A.; Lithgow, T.; McLean, K. M.; Thissen, H. *Trends in Biotechnology* **2014**, 32, (2), 82-90.

31. Vasilev, K.; Griesser, S. S.; Griesser, H. J. *Plasma Processes and Polymers* **2011**, 8, (11), 1010-1023.
32. De Kwaadsteniet, M.; Botes, M.; Cloete, T. E. *Nano* **2011**, 6, (5), 395-407.
33. Cagri, A.; Ustunol, Z.; Ryser, E. T. *Journal of Food Protection* **2004**, 67, (4), 833-848.
34. Visai, L.; de Nardo, L.; Punta, C.; Melone, L.; Cigada, A.; Imbriani, M.; Arciola, C. R. *International Journal of Artificial Organs* **2011**, 34, (9), 929-946.
35. Dunnill, C. W.; Parkin, I. P. *Dalton Transactions* **2011**, 40, (8), 1635-1640.
36. Tian, B.; Chen, W.; Yu, D.; Lei, Y.; Ke, Q.; Guo, Y.; Zhu, Z. *Journal of the Mechanical Behavior of Biomedical Materials* **2016**, 61, 345-359.
37. Huxtar, Y.; Wang, Y. B.; Abibulla, M.; Abdukeyum, A.; Muhtar, N.; Su, Z. *Acta Polymerica Sinica* **2016**, (4), 528-537.
38. Ciuca, S.; Badea, M.; Pozna, E.; Pana, I.; Kiss, A.; Floroian, L.; Semenescu, A.; Cotrut, C. M.; Moga, M.; Vladescu, A. *Journal of Microbiological Methods* **2016**, 125, 12-18.
39. Buckholtz, G. A.; Reger, N. A.; Anderton, W. D.; Schimoler, P. J.; Roudebush, S. L.; Meng, W. S.; Miller, M. C.; Gawalt, E. S. *Materials Science and Engineering C* **2016**, 65, 126-134.
40. Tian, J.; Shen, S.; Zhou, C.; Dang, X.; Jiao, Y.; Li, L.; Ding, S.; Li, H. *Journal of Materials Science: Materials in Medicine* **2015**, 26, (2).
41. Cai, R.; Wang, H.; Cao, M.; Hao, L.; Zhai, L.; Jiang, S.; Li, X. *Materials and Design* **2015**, 87, 17-24.
42. Yu, J.; Chu, X.; Cai, Y.; Tong, P.; Yao, J. *Materials Science and Engineering C* **2014**, 37, (1), 54-59.
43. Wang, L.; He, S.; Wu, X.; Liang, S.; Mu, Z.; Wei, J.; Deng, F.; Deng, Y.; Wei, S. *Biomaterials* **2014**, 35, (25), 6758-6775.
44. Murakami, A.; Arimoto, T.; Suzuki, D.; Iwai-Yoshida, M.; Otsuka, F.; Shibata, Y.; Igarashi, T.; Kamijo, R.; Miyazaki, T. *Nanomedicine: Nanotechnology, Biology, and Medicine* **2012**, 8, (3), 374-382.
45. Salehi, S.; Davis, H. B.; Ferracane, J. L.; Mitchell, J. C. *American Journal of Dentistry* **2015**, 28, (2), 111-115.

46. Caldeira, É. M.; Osório, A.; Oberosler, E. L. C.; Vaitsman, D. S.; Alviano, D. S.; Nojima, M. C. G. *Journal of Applied Oral Science* **2013**, 21, (4), 327-334.
47. Lellouche, J.; Friedman, A.; Lellouche, J. P.; Gedanken, A.; Banin, E. *Nanomedicine: Nanotechnology, Biology, and Medicine* **2012**, 8, (5), 702-711.
48. Lellouche, J.; Friedman, A.; Gedanken, A.; Banin, E. *International Journal of Nanomedicine* **2012**, 7, 5611-5624.
49. Ogaard, B.; Larsson, E.; Henriksson, T.; Birkhed, D.; Bishara, S. E. *American Journal of Orthodontics and Dentofacial Orthopedics* **2001**, 120, (1), 28-35.
50. Prasad, T. N. V. K. V.; Kambala, V. S. R.; Naidu, R. *Current Nanoscience* **2011**, 7, (4), 531-544.
51. Zhang, C.; Hu, Z.; Deng, B. *Water Research* **2016**, 88, 403-427.
52. Le Ouay, B.; Stellacci, F. *Nano Today* **2015**, 10, (3), 339-354.
53. Ishihara, M.; Nguyen, V. Q.; Mori, Y.; Nakamura, S.; Hattori, H. *International Journal of Molecular Sciences* **2015**, 16, (6), 13973-13988.
54. Austin, L. A.; MacKey, M. A.; Dreaden, E. C.; El-Sayed, M. A. *Archives of Toxicology* **2014**, 88, (7), 1391-1417.
55. Ravindran, A.; Chandran, P.; Khan, S. S. *Colloids and Surfaces B: Biointerfaces* **2013**, 105, 342-352.
56. Maillard, J. Y.; Hartemann, P. *Critical reviews in microbiology* **2013**, 39, (4), 373-383.
57. Drelich, J.; Li, B.; Villeneuve, B.; Bowen, P. *Surface Innovations* **2013**, 1, (1), 15-26.
58. Ruiz-Hitzky, E.; Darder, M.; Fernandes, F. M.; Wicklein, B.; Alcântara, A. C. S.; Aranda, P. *Progress in Polymer Science* **2013**, 38, (10–11), 1392-1414.
59. Bociaga, D.; Komorowski, P.; Batory, D.; Szymanski, W.; Olejnik, A.; Jastrzebski, K.; Jakubowski, W. *Applied Surface Science* **2015**, 355, 388-397.
60. Hosseini, S. I.; Sharifian, M.; Shokri, B. *Surface & Coatings Technology* **2012**, 213, 285-290.
61. Marciano, F. R.; Bonetti, L. F.; Mangolin, J. F.; Da-Silva, N. S.; Corat, E. J.; Trava-Airoldi, V. J. *Vacuum* **2011**, 85, (6), 662-666.
62. Marciano, F. R.; Lima-Oliveira, D. A.; Da-Silva, N. S.; Corat, E. J.; Trava-Airoldi, V. J. *Surface & Coatings Technology* **2010**, 204, (18-19), 2986-2990.

63. Zhao, C.; Deng, B.; Chen, G. C.; Lei, B.; Hua, H.; Peng, H. L.; Yan, Z. M. *Nano Research* **2016**, 9, (4), 963-973.
64. Mangadlao, J. D.; Santos, C. M.; Felipe, M. J. L.; de Leon, A. C. C.; Rodrigues, D. F.; Advincula, R. C. *Chemical Communications* **2015**, 51, (14), 2886-2889.
65. Dellieu, L.; Lawaree, E.; Reckinger, N.; Didembourg, C.; Letesson, J. J.; Sarrazin, M.; Deparis, O.; Matroule, J. Y.; Deparis, J. F. *Carbon* **2015**, 84, 310-316.
66. Karumuri, A. K.; He, L. M.; Mukhopadhyay, S. M. *Applied Surface Science* **2015**, 327, 122-130.
67. Kazmi, S. J.; Shehzad, M. A.; Mehmood, S.; Yasar, M.; Naeem, A.; Bhatti, A. S. *Sensors and Actuators A: Physical* **2014**, 216, 287-294.
68. Yoosefi Booshehri, A.; Wang, R.; Xu, R. *Chemical Engineering Journal* **2013**, 230, 251-259.
69. Akhavan, O.; Abdolahad, M.; Abdi, Y.; Mohajezadeh, S. *Journal of Materials Chemistry* **2011**, 21, (2), 387-393.
70. Lyon, D. Y.; Brown, D.; Sundstrom, E. R.; Alvarez, P. J. J. *International Biodeterioration & Biodegradation* **2008**, 62, (4), 475-478.
71. Saud, P. S.; Pant, B.; Alam, A. M.; Ghouri, Z. K.; Park, M.; Kim, H. Y. *Ceramics International* **2015**, 41, (9), 11953-11959.
72. Baslak, C.; Kars, M. D.; Karaman, M.; Kus, M.; Cengeloglu, Y.; Ersoz, M. *Journal of Luminescence* **2015**, 160, 9-15.
73. Yang, X.; Li, J.; Liang, T.; Ma, C.; Zhang, Y.; Chen, H.; Hanagata, N.; Su, H.; Xu, M. *Nanoscale* **2014**, 6, (17), 10126-10133.
74. Yang, K.; Li, Y.; Tan, X.; Peng, R.; Liu, Z. *Small* **2013**, 9, (9-10), 1492-1503.
75. Wang, Z.; Zhu, W.; Qiu, Y.; Yi, X.; von dem Bussche, A.; Kane, A.; Gao, H.; Koski, K.; Hurt, R. *Chemical Society Reviews* **2016**, 45, (6), 1750-1780.
76. Maget-Dana, R. *Biochimica et Biophysica Acta (BBA) - Biomembranes* **1999**, 1462, (1-2), 109-140.
77. Kaur, H.; Yadav, S.; Srivastava, A. K.; Singh, N.; Schneider, J. J.; Sinha, O. P.; Agrawal, V. V.; Srivastava, R. *Scientific Reports* **2016**, 6, 34095.
78. Ding, S.-J.; Lee, T.-L.; Chu, Y.-H. *Journal of Materials Science Letters* **2003**, 22, (6), 479-482.



79. Ajaev, V. S.; Gatapova, E. Y.; Kabov, O. A. *Advances in Colloid and Interface Science* **2016**, 228, 92-104.
80. Costa, F.; Carvalho, I. F.; Montelaro, R. C.; Gomes, P.; Martins, M. C. L. *Acta Biomaterialia* **2011**, 7, (4), 1431-1440.
81. Gupta, A.; Sakthivel, T.; Seal, S. *Progress in Materials Science* **2015**, 73, 44-126.
82. Nicolosi, V.; Chhowalla, M.; Kanatzidis, M. G.; Strano, M. S.; Coleman, J. N. *Science* **2013**, 340, (6139).
83. Wang, Q. H.; Kalantar-Zadeh, K.; Kis, A.; Coleman, J. N.; Strano, M. S. *Nat Nano* **2012**, 7, (11), 699-712.
84. Lew Yan Voon, L. C.; Sandberg, E.; Aga, R. S.; Farajian, A. A. *Applied Physics Letters* **2010**, 97, (16), 163114.
85. Houssa, M.; Scalise, E.; Sankaran, K.; Pourtois, G.; Afanas'ev, V. V.; Stesmans, A. *Applied Physics Letters* **2011**, 98, (22), 223107.
86. Bianco, E.; Butler, S.; Jiang, S.; Restrepo, O. D.; Windl, W.; Goldberger, J. E. *ACS Nano* **2013**, 7, (5), 4414-4421.
87. Madhushankar, B. N.; Kaverzin, A.; Giousis, T.; Potsi, G.; Gournis, D.; Rudolf, P.; Blake, G. R.; Wal, C. H. v. d.; Wees, B. J. v. *2D Materials* **2017**, 4, (2), 021009.
88. Jiang, S.; Bianco, E.; Goldberger, J. E. *Journal of Materials Chemistry C* **2014**, 2, (17), 3185-3188.
89. Cote, L. J.; Kim, F.; Huang, J. X. *Journal of the American Chemical Society* **2009**, 131, (3), 1043-1049.
90. Bergey, D. H.; Buchanan, R. E.; Gibbons, N. E.; American Society for, M., *Bergey's manual of determinative bacteriology*. Williams & Wilkins Co.: Baltimore, 1974.
91. Bentley, R.; Meganathan, R. *Microbiological Reviews* **1982**, 46, (3), 241-280.
92. Hudault, S.; Guignot, J.; Servin, A. *Gut* **2001**, 49, (1), 47-55.
93. Reid, G.; Howard, J.; Gan, B. S. *Trends in Microbiology* **2001**, 9, (9), 424-428.
94. Kouloumpis, A.; Dimos, K.; Spyrou, K.; Georgakilas, V.; Rudolf, P.; Gournis, D. *Frontiers in Materials* **2015**, 2, (10).
95. Michopoulos, A.; Kouloumpis, A.; Gournis, D.; Prodromidis, M. I. *Electrochimica Acta* **2014**, 146, 477-484.

96. Giannakas, A.; Vlachas, M.; Salmas, C.; Leontiou, A.; Katapodis, P.; Stamatis, H.; Barkoula, N.-M.; Ladavos, A. *Carbohydrate polymers* **2016**, 140, 408-415.
97. Santo, C. E.; Taudte, N.; Nies, D. H.; Grass, G. *Applied and Environmental Microbiology* **2008**, 74, (4), 977-986.
98. Drummond, I. M. A. A study of Germanium Hydrides, Anions and related Species. PhD Thesis, McMaster University, 1970.
99. Jiang, S.; Butler, S.; Bianco, E.; Restrepo, O. D.; Windl, W.; Goldberger, J. E. *Nature Communications* **2014**, 5.
100. Liu, Z.; Lou, Z.; Li, Z.; Wang, G.; Wang, Z.; Liu, Y.; Huang, B.; Xia, S.; Qin, X.; Zhang, X.; Dai, Y. *Chemical Communications* **2014**, 50, (75), 11046-11048.
101. Epand, R. M.; Epand, R. F. *Biochimica et Biophysica Acta (BBA) - Biomembranes* **2009**, 1788, (1), 289-294.
102. Perreault, F.; de Faria, A. F.; Nejati, S.; Elimelech, M. *ACS Nano* **2015**, 9, (7), 7226-7236

## Summary

The extraordinary physicochemical properties and the high specific area of 2D materials render them very attractive for a plethora of potential applications; they can be used as platforms for integrating different moieties, clusters, molecules or nanomaterials into hybrids, allowing for the creation of composites with new or enhanced properties. On the other hand, the importance of preparing layer-by-layer hybrid films relies on the ability to control the architecture, the thickness, and the functionality of the formed nanostructures.

The aim of this thesis focuses on the development and study of novel low-dimensional films and hybrids based on layered nanomaterials such as graphene and germanane, assembled with the help of the Langmuir-Blodgett (LB) technique.

The Langmuir-Blodgett technique is one of the most promising layer-by-layer methods for preparing thin films with varying layer composition (organic or/and inorganic nanostructures). This bottom-up approach allows to accurately control the thickness of the deposited film and allows for a homogeneous deposition over large areas with a high degree of structural order. Numerous studies have been reported during the past years concerning the assembly of graphene sheets and different building blocks by the LB method in order to produce hybrid thin films with enhanced optoelectronic and mechanical properties. Such single layer or multilayer systems can be employed in a variety of different application areas such as in electronics, solar cells and sensors, as described in Chapter 2.

Much of the research effort on graphene focuses on its use in the development of new hybrid nanostructures suitable for applications in gas storage, heterogeneous catalysis, gas/liquid separations, nanosensing, and biomedicine. Towards this aim, in Chapter 3 we describe a bottom-up approach, which combines the self-assembly with the Langmuir-Schaefer (LS) deposition technique in order to fabricate graphene-based layered hybrid materials that host fullerene molecules within the interlayer space. As was revealed by conductivity measurements, the presence of C<sub>60</sub> within the interlayer spacing lowers the resistivity of the hybrid material as compared to the pure organo-graphene matrix. This graphene/fullerene hybrid could ideally be used as transparent electrodes as well as in thin film transistors or supercapacitors.

Motivated by the previous work, a further investigation of graphene-based hybrid thin films fabricated by the same bottom-up approach but hosting fullerene derivatives was reported in Chapter 4. More specifically, fullerols ( $C_{60}(OH)_{24}$ ) and bromo-fullerenes ( $C_{60}Br_{24}$ ) molecules were integrated in graphene oxide (GO) layers by combining the Langmuir-Schaefer technique with one and two self-assembly steps respectively. The hybrid thin films were characterized by a variety of techniques in order to prove the presence of the fullerene derivatives between the GO layers. Moreover, wetting experiments revealed that the ODA-GO- $C_{60}(OH)_{24}$  hybrid system exhibits a more hydrophobic character than ODA-GO- $C_{60}Br_{24}$ , suggesting that the hydrophobicity doesn't depend on the functional groups of the pristine nanomaterials but on the morphology of the hybrid system. These novel fullerene-based hybrid films could be candidates for potential applications in photovoltaics, sensors, or optoelectronic devices as well as in photocatalysis and drug delivery.

In Chapter 5 a new class of highly ordered hydrophilic luminescent carbon dot (C-dot) intercalated graphene oxide structures was reported for the first time; the material was produced by combining the Langmuir-Schaefer method with self-assembly. The precise thickness control combined with homogeneous deposition makes the LS technique ideal for preventing aggregation of carbon-based nanostructures such as fullerene or carbon dots in hybrid systems. C-dots with a mean diameter of 4 nm were produced by microwave-assisted pyrolysis, which is a convenient method because it is low-cost, facile and efficient. The transparency of the hybrid multilayers consisting of C-dots sandwiched between graphene oxide showed could be controlled by adjusting the number of the deposited layers. The high quality photoluminescence with narrow emissions of C-dots is preserved in these multilayer films. These novel hybrid systems are suitable for applications such as nanoprobe, optoelectronic devices and transparent electrodes as well as for drug delivery.

Germanane (GeH), the germanium graphene-analogue has recently attracted considerable interest due to its high mobility, non-zero band gap and optoelectronic properties. In Chapter 6, we describe how germanane was produced at room temperature by a new synthetic approach based on the topotactic deintercalation of  $\beta$ -

CaGe<sub>2</sub> in aqueous HF solution. The exfoliated germanane nanosheets can be assembled into deposited monolayer films with different packing density exploiting the Langmuir-Schaefer method. The coverage, uniformity and single-layer level control of the assembly was confirmed by  $\pi$ -A isotherms and AFM measurements. The antimicrobial activity of germanane in aqueous dispersion and in monolayers form was investigated for the first time. Our results revealed that an antimicrobial effect of germanane for Gram-negative and Gram-positive bacteria, with an especially outstanding activity against *Brevibacterium* bacterial strains. The monolayers produced by the Langmuir-Schaefer might be applied in the future as high efficiency antimicrobial surfaces in hospitals and in the food industry.



# Samenvatting

De buitengewone fysisch-chemische eigenschappen en het grote specifieke oppervlak van 2D materialen maken een overvloed aan applicaties mogelijk; ze kunnen gebruikt worden als platform voor de integratie van verschillende eenheden, clusters, moleculen of nanomaterialen in hybriden, wat kan leiden tot composieten met nieuwe en verbeterde eigenschappen. Anderzijds is de mate van controle over de architectuur, dikte en functionaliteit van de gevormde nanostructuren van groot belang voor het bereiden van laag-bij-laag hybride films.

Het doel van dit proefschrift concentreert zich op de ontwikkeling en het bestuderen van nieuwe laag-dimensionale films en hybrides gebaseerd op gelaagde nanomaterialen, zoals grafeen en germanaan, geassembleerd met behulp van de Langmuir-Blodgett (LB) techniek.

De Langmuir-Blodgett techniek is een veelbelovende methode voor laag-bij-laag formatie van dunne films met een gevarieerde laag-compositie (organische of/en anorganische nanostructuren). Deze bottom-up aanpak maakt precieze controle over de dikte van de gedeponeerde film mogelijk, evenals homogene depositie over grote oppervlakken met een hoge graad van structurele orde. In de afgelopen jaren zijn veel studies gepubliceerd over de assemblage van grafeen en verschillende bouwblokken met behulp van de LB methode, om hybride dunne films met verbeterde opto-elektronische en mechanische eigenschappen te produceren. Dergelijke enkellaagse of multilaagse systemen kunnen toegepast worden in een verscheidenheid van gebieden, zoals elektronica, zonnecellen en sensoren, zoals beschreven in Hoofdstuk 2.

Veel van de onderzoeksinspanningen naar grafeen richten zich op zijn nut in de ontwikkeling van nieuwe hybride nanostructuren die geschikt zijn voor applicaties in gasopslag, heterogene katalyse, gas/vloeistof separatie, nanosensoren en biomedicijnen. In Hoofdstuk 3 wordt een bottom-up aanpak beschreven die zelfassemblage combineert met de Langmuir-Schaefer (LS) depositietechniek, om op grafeen gebaseerde gelaagde hybride materialen te vormen die fullereenmoleculen in de tussenlaagruimtes bevatten. Zoals blijkt uit

geleidingsmetingen verlaagt de aanwezigheid van  $C_{60}$  in de tussenlaagruimtes de weerstand van het hybride materiaal vergeleken met de zuivere organisch gefunctionaliseerde grafeen matrix. Deze grafeen/fullereen hybride zou perfect gebruikt kunnen worden in dunne film transistoren, supercondensatoren of dienst doen als transparante elektrodes.

Gemotiveerd door het voorgaande werk is verder onderzoek verricht naar de op grafeen gebaseerde hybride dunne films gefabriceerd met dezelfde bottom-up aanpak, echter bevatten deze films fullereenderivaten in de tussenlaagruimtes; dit is beschreven in Hoofdstuk 4. Deze fullereenderivaten zijn fullerols ( $C_{60}(OH)_{24}$ ) en broomfullereen ( $C_{60}Br_{24}$ ) die geïntegreerd zijn in grafeenoxide (GO) lagen door de combinatie van de Langmuir-Schaefer techniek met respectievelijk één en twee zelfassemblage stappen. De hybride dunne lagen zijn gekarakteriseerd door verscheidene technieken om de aanwezigheid van de fullereenderivaten tussen de GO lagen aan te tonen. Verder hebben bevochtigbaarheidsexperimenten aangetoond dat het ODA-GO- $C_{60}(OH)_{24}$  hybride systeem een meer hydrofoob karakter vertoont dan ODA-GO-HEX- $C_{60}Br_{24}$ , wat suggereert dat de hydrofobiciteit niet afhangt van de functionele groepen van ongerepte nanomaterialen, maar van de morfologie van het hybride systeem. Deze nieuwe op fullereen gebaseerde hybride films zijn mogelijk kandidaten voor applicaties in fotonische systemen, sensoren of opto-elektronische apparatuur, evenals in fotokatalyse en medicijnafgifte.

In Hoofdstuk 5 wordt voor het eerst een nieuwe klasse beschreven van hoog geordend hydrofiel luminescerend intercaleerde koolstof kwantum punten (C-dot) in grafeenoxide structuren; het materiaal werd geproduceerd door de Langmuir-Schaefer methode met zelfassemblage te combineren. De precieze dikte controle gecombineerd met homogene depositie maakt de LS techniek ideaal voor het voorkomen van aggregatie van koolstofgebaseerde nanostructuren, zoals fullereen of koolstof kwantum punten in hybride systemen. C-dots met een gemiddelde diameter van 4 nm werden geproduceerd door microgolf-geassisteerde pyrolyse; een geschikte methode vanwege zijn lage kosten, simpliciteit en efficiëntie. De transparantie van de hybride multilagen bestaande uit C-dots ingeklemd tussen grafeenoxide, kon gecontroleerd worden door het aanpassen van het aantal gedeponeerde lagen. De hoge kwaliteit fotoluminescentie met nauwe emissies van



C-dots is behouden in deze multilaag-films. Deze nieuwe hybride systemen zijn geschikt voor applicaties zoals nanoprobe, opto-elektronische apparatuur, transparante elektrodes en medicijnafgifte.

Germanaan (GeH), het germanium grafeen-analoog, heeft onlangs veel aandacht getrokken vanwege zijn hoge mobiliteit, bandkloof groter dan nul en opto-elektronische eigenschappen. In hoofdstuk 6 wordt beschreven hoe germanaan werd geproduceerd door een nieuwe synthetische aanpak gebaseerd op topotactische deintercalatie van  $\beta$ -CaGe<sub>2</sub> in waterige HF oplossing. De gefolieerde germanaan nanovellen kunnen geassembleerd worden in gedeponeerde monolaag films met verschillende pakkingsdichtheid gebruikmakend van de Langmuir-Schaefer methode. De dekkingsgraad, uniformiteit en de enkellaagse niveau controle van de assemblage werd bevestigd met  $\pi$ -A isothermen en AFM metingen. De antimicrobiële activiteit van germanaan in een waterige dispersie en in monolaagvorm werd voor het eerst onderzocht. Uit onze resultaten bleek een antimicrobiële werking van germanaan voor Gram-negatieve en Gram-positieve bacteriën, met een uitstekende activiteit tegen de *Brevibacterium* bacteriestammen. De monolagen die door de Langmuir-Schaefer techniek worden geproduceerd, zouden in de toekomst kunnen worden toegepast als zeer efficiënte antimicrobiële oppervlakken in ziekenhuizen en in de voedingsindustrie.



## Περίληψη

Οι εξαιρετικές φυσικοχημικές ιδιότητες και η υψηλή ειδική επιφάνεια των 2D υλικών, τα καθιστούν ιδιαίτερα ελκυστικά σε μια πληθώρα εφαρμογών. Ανάμεσα σε άλλα μπορούν να χρησιμοποιηθούν ως πλατφόρμες για την ενσωμάτωση διαφορετικών συστάδων, μορίων ή νανοϋλικών επιτρέποντας τη δημιουργία υβριδίων και σύνθετων υλικών με νέες ή βελτιωμένες ιδιότητες. Από την άλλη πλευρά, η σπουδαιότητα της παρασκευής στρώμα με στρώμα (layer-by-layer) υβριδικών υμενίων, έγκειται στο γεγονός του ελέγχου της αρχιτεκτονικής, του πάχους, και της λειτουργικότητας των σχηματιζόμενων νανοδομών.

Τα κεφάλαια της παρούσας διδακτορικής διατριβής επικεντρώνονται στην ανάπτυξη και μελέτη χαμηλοδιάστατων υβριδικών υμενίων αποτελούμενων από ανόργανες φυλλόμορφες νανοδομές όπως το γραφένιο και το γερμανάνιο, κάνοντας χρήση της μεθόδου Langmuir-Blodgett (LB).

Η τεχνική Langmuir-Blodgett είναι μια από τις πιο ελπιδοφόρες στρώμα-με-στρώμα τεχνικές για την προετοιμασία λεπτών υμενίων με ποικίλες συστάσεις στρωμάτων (οργανικές ή/και ανόργανες νανοδομές). Αυτή η bottom-up προσέγγιση δίνει τη δυνατότητα για τον ακριβή έλεγχο του πάχους του μονοστρώματος ενώ επιτρέπει την ομοιογενή εναπόθεσή του σε μεγάλες περιοχές και επιφάνειες με υψηλό βαθμό δομικής τάξης. Πολυάριθμες μελέτες έχουν αναφερθεί τα τελευταία χρόνια, στην τροποποίηση των φύλλων γραφενίου με την LB τεχνική με σκοπό την παραγωγή υβριδικών λεπτών υμενίων για την βελτιστοποίηση των οπτοηλεκτρονικών και μηχανικών ιδιοτήτων του γραφενίου. Αυτά τα μονοστρωματικά ή πολυστρωματικά συστήματα με τις εξαιρετικές ιδιότητες, χρησιμοποιούνται σε ένα μεγάλο εύρος εφαρμογών, από ηλεκτρονικά συστήματα, φωτοβολταϊκά ως και αισθητήρες όπως περιγράφεται στο 2<sup>ο</sup> κεφάλαιο.

Ένα μεγάλο μέρος της επιστημονικής έρευνας σχετικά με το γραφένιο επικεντρώνεται στη χρήση του ως δομικό στοιχείο για την ανάπτυξη νέων υβριδικών νανοδομών με σαφώς καθορισμένες διαστάσεις και ιδιότητες,

κατάλληλες για εφαρμογές όπως η αποθήκευση αερίων, η ετερογενής κατάλυση, ο διαχωρισμός αερίων/υγρών, οι νανοαισθητήρες και η βιοϊατρική. Προς την κατεύθυνση αυτή, στο 3<sup>ο</sup> κεφάλαιο περιγράφεται μια bottom-up προσέγγιση, η οποία συνδυάζει την αυτο-οργάνωση με την τεχνική εναπόθεσης Langmuir-Schaefer (LS) με σκοπό την δημιουργία υβριδικών υμενίων με βάση το γραφένιο στο οποίο περιέχονται μόρια φουλερενίων ( $C_{60}$ ) εντός του ενδοστρωματικού χώρου του φυλλόμορφου υλικού. Συμπερασματικά, παρατηρήθηκε ότι η παρουσία των μορίων  $C_{60}$  στον ενδοστρωματικό χώρο του γραφενίου οδηγεί σε αύξηση της ηλεκτρικής αγωγιμότητας του υβριδικού υμενίου συγκριτικά με το οργανοτροποποιημένο γραφένιο. Τέτοια υβριδικά υλικά σαν το αυτό του γραφενίου/φουλερενίου μπορούν να χρησιμοποιηθούν ως υλικά σε εφαρμογές όπως τα διαφανή ηλεκτρόδια, τα τρανζίστορ ή ως υπερπυκνωτές.

Μια περαιτέρω έρευνα για την ανάπτυξη υβριδικών υμενίων με βάση το γραφένιο στο οποίο περιέχονται παράγωγα μόρια των  $C_{60}$  παρουσιάζεται στο 4<sup>ο</sup> κεφάλαιο. Πιο συγκεκριμένα, φουλερόλια ( $C_{60}(OH)_{24}$ ) και βρώμοφουλερένια ( $C_{60}Br_{24}$ ) εντέθηκαν ανάμεσα στα φύλλα οξειδίου του γραφενίου (GO) συνδυάζοντας την τεχνική Langmuir-Schaefer με ένα ή δύο στάδια της τεχνικής αυτο-οργάνωσης, αντίστοιχα. Τα υβριδικά λεπτά υμένια χαρακτηρίστηκαν με μια πληθώρα τεχνικών με στόχο την επιβεβαίωση της ύπαρξης των παραγώγων των φουλερενίων ανάμεσα στα φύλλα του GO. Όπως παρατηρήθηκε από τις μετρήσεις διαβροχής το υβριδικό σύστημα ODA-GO- $C_{60}(OH)_{24}$ , παρουσιάζει έναν πιο υδρόφοβο χαρακτήρα συγκριτικά με το σύστημα ODA-GO-HEX- $C_{60}Br_{24}$  υποδηλώνοντας ότι η υδροφοβικότητα δεν εξαρτάται από τις λειτουργικές ομάδες των αρχικών νανοϋλικών αλλά από την σχηματιζόμενη μορφολογία του υβριδικού συστήματος. Τα παραγόμενα υβριδικά λεπτά υμένια με βάση το γραφένιο στο οποίο περιέχονται παράγωγα των  $C_{60}$  μορίων συνιστούν νέα υβριδικά συστήματα που θα μπορούσαν να χρησιμοποιηθούν ως ιδανικά νανοϋλικά για εφαρμογές στα οπτοηλεκτρονικά συστήματα, στα φωτοβολταϊκά, στα φάρμακα καθώς επίσης και στον τομέα της φωτοκατάλυσης.

Στο 5<sup>ο</sup> κεφάλαιο, περιγράφεται η ενσωμάτωση νανοτελειών άνθρακα (C-dots) στη δομή του γραφενίου για πρώτη φορά, κάνοντας χρήση μιας τροποποιημένης Langmuir-Schaefer τεχνικής. Πιο συγκεκριμένα νέα υβριδικά πολυστρωματικά υμένα αποτελούμενα από οξειδίο του γραφενίου και εντεθειμένες φωτοβόλες νανοτελείες άνθρακα παρασκευάστηκαν συνδυάζοντας την τεχνική Langmuir-Schaefer με την τεχνική της αυτο-οργάνωσης. Ο ακριβής έλεγχος σε συνδυασμό με την ομοιογενή εναπόθεση, καθιστά την LS τεχνική ιδανική για την πρόληψη της συσσωμάτωσης των νανοδομών άνθρακα σε υβριδικά συστήματα, όπως τα φουλερένια και οι νανοτελείες άνθρακα. Οι νανοτελείες άνθρακα, με μέση διάμετρο 4 nm, παρήχθησαν με πυρόλυση υποβοηθούμενη από μικροκύματα, η οποία είναι μια προτιμητέα μέθοδος εξαιτίας τους χαμηλού κόστους, της εύκολης εγκατάστασης και της αποτελεσματικότητάς της. Τα υβριδικά πολυστρωματικά υμένα αποτελούμενα από εντεθειμένες νανοτελείες άνθρακα ανάμεσα στα φύλλα του οξειδίου του γραφενίου, παρουσίασαν ελεγχόμενη διαφάνεια ανάλογα με την προσαρμογή του αριθμού των εναποτεθειμένων στρωμάτων. Τέλος, τα υβριδικά πολυστρωματικά υμένα εμφανίζουν υψηλής ποιότητας φωτοφωταύγεια με στενές εκπομπές γεγονός που οφείλεται στην επιτυχημένη ενσωμάτωση των νανοτελειών άνθρακα ανάμεσα σε φύλλα γραφενίου. Αυτά τα πολυστρωματικά υμένα αποτελούν ένα καινοτόμο υβριδικό σύστημα κατάλληλο για μια πληθώρα εφαρμογών όπως οι νανοανιχνευτές, οι οπτοηλεκτρονικές διατάξεις και τα διαφανή ηλεκτρόδια, καθώς επίσης και σε συστήματα χορήγησης φαρμάκων.

Το γερμανάνιο (GeH), ένα ανάλογο του γραφενίου, έχει προσελκύσει πρόσφατα ιδιαίτερο ενδιαφέρον λόγω των οπτοηλεκτρονικών ιδιοτήτων του καθώς και λόγω της σταθερότητάς του. Η υψηλή κινητικότητα των ηλεκτρονίων, το μη μηδενικό ενεργειακό χάσμα και οι χαμηλές διαστάσεις καθιστούν το γερμανάνιο ένα πολλά υποσχόμενο δισδιάστατο υλικό για μια πληθώρα εφαρμογών υψηλής απόδοσης. Στο 6<sup>ο</sup> κεφάλαιο, το γερμανάνιο παρασκευάστηκε σε θερμοκρασία περιβάλλοντος με μία καινούρια μέθοδο σύνθεσης βασιζόμενη στην τοποτακτική απένθεση της φάσης  $\beta$ -CaGe<sub>2</sub> σε υδατικό διάλυμα HF. Επιπλέον χρησιμοποιήθηκε η οργάνωση Langmuir-

Schaefer για τον έλεγχο της πυκνότητας των αποφυλλοποιημένων νανοφυλλιδίων γερμανίου, με σκοπό την δημιουργία νέων μονοστρωματικών υμενίων. Η επικάλυψη, η ομοιομορφία και ο έλεγχος της οργάνωσης σε μονοατομικό επίπεδο επιβεβαιώθηκαν από τις π-Α ισόθερμες καμπύλες καθώς και από την μικροσκοπία ατομικών δυνάμεων (AFM). Η αντιμικροβιακή δράση του γερμανίου σε υδατική διασπορά καθώς και σε μορφή μονοστρωματικού υμενίου διερευνήθηκε για πρώτη φορά με τη βοήθεια της μεθόδου πλάκας μικροτίτλου και των βιώσιμων κυττάρων επιβίωσης σε επιφάνειες επικαλυπτόμενες με γερμανάνιο, αντίστοιχα. Σύμφωνα με τα αποτελέσματα η αντιμικροβιακή δράση του γερμανίου εξαρτάται από τη δομική διαφορά των κυτταρικών μεμβρανών και τη σύνθεση του κυτταρικού τοιχώματος των Gram-αρνητικών και Gram-θετικών βακτηριδίων. Πιο συγκεκριμένα, τα αποτελέσματα της υδατικής διασποράς του γερμανίου αποκάλυψαν ότι κατά τη διάρκεια των πρώτων έξι ωρών η βακτηριακή ανάπτυξη καταστέλλεται πολύ έντονα ενώ μία εξαιρετική αντιμικροβιακή δράση των υμενίων γερμανίου παρατηρήθηκε για τα βακτηριακά στελέχη *Brevibacterium*. Τα μονοατομικά υμένια που παρασκευάστηκαν με την μέθοδο Langmuir-Schaefer θα μπορούσαν να εφαρμοστούν στο μέλλον ως αντιμικροβιακές επιφάνειες υψηλών αποδόσεων σε νοσοκομεία καθώς επίσης και στη βιομηχανία τροφίμων.

# Acknowledgements

This PhD thesis is the result of an effort that it was performed at the Ceramics and Composites Laboratory of Materials Science and Engineering department of University of Ioannina, Greece and at the Zernike Institute for Advanced Materials in University of Groningen, Netherlands. However I could never finish this thesis without any support and help. At this point I would like to express my gratitude to all of these people that helped me during these years for accomplishing this dissertation.

First of all I am grateful to my promoters Prof. Petra Rudolf and Prof. Dimitrios Gournis who motivated and inspired me all these years.

More specifically, I would like to thank Prof. Dimitrios Gournis for changing my life in 2009. He was the person that inspired me to continue in the fields of science and research after my undergraduate studies guiding me also in my Diploma and Master thesis. Beside the immense knowledge gained from him I would like to thank him also for his patience, his trust and his support. Besides the above, the most important thing for me is that after all these years I consider him family.

At the same time I would like to thank Prof. Petra Rudolf for giving me the chance to join her group. Her valuable guidance, suggestions and advices during my PhD studies were very helpful for this thesis to be completed. Moreover, her positive energy and her enthusiasm gave me a lot of encouragement to overcome any barrier.

Besides my promoters, I would like to thank the members of the reading committee Prof. Francesco Picchioni, Prof. Georg Düsberg, Prof. Alkiviadis Paipetis and Prof. George Froudakis for their willingness to read my thesis. Moreover I would like to thank the rest members of the committee in Greece, Prof. Michael Karakassides, Prof. Athanasios Bourlinos, Prof. George Froudakis, Prof. Alkiviadis Paipetis and Prof. Haralambos Stamatis.

I would also like to acknowledge Jos Noteboom and Hilda Riemens for translating and correcting the Dutch summary in this thesis.

For an ideally excellent collaboration, I would like to express my gratitude to Prof. Athanasios B. Bourlinos from Physics Department, University of Ioannina and to Prof. Vasilios Georgakilas from Department of Material Science, University of Patras.

Nevertheless, I am also grateful to all the collaborators during my studies. Thanks to: Prof. Michael A. Karakassides, Prof. Haralambos Stamatis, Prof. Richard, F. Reidy, Prof. Hae Jin Kim, Prof. Radek Zbořil, Prof. Mamas I. Prodromidis, Prof. Yiannis Deligiannakis, Prof. Dimosthenis L. Giokas, Prof. Petros Katapodis, Prof. Vasillios Stathopoulos, Dr. Georgios Papavassiliou, Dr. Theodoros Tsoufis, Dr. Georgia Potsi, Dr. Michaela Patila, Dr. Panagiota Zygouri, Dr. Konstantinos Dimos, Dr. Konstantinos Spyrou, Dr. Vasillios Kostas, Dr. Maria Baikousi, Dr. Nikolaos Vourdas, Dr. Andreas Rossos, Dr. Myrsini Antoniou, Dr. Eleni Bletsas, Eleftherios Mouzourakis, Eleni Thomou, Nikolaos Chalmpes, Theodosios Giousis and Nikolina Vourvou.

I would like to acknowledge the European Union (European Social Fund-ESF) and Greek national funds through the Operational Program "Thalis" for funding me during my studies.

Thanks a lot to the members of the both groups that beside my fellow labmates are most of them also good friends: Souzana, Fouli, M. Maria, A. Maria, K. Maria, Vasilli, V. Kosta, D. Kosta, S. Kosta, Giouli, Myrsini, Klairi, Christina, Lefteri, P. Eleni, Kyriaki-Marina, Elina, Lena, Niki, Theodosi, Niko, Mohammed, Michaela, Valentina, Katerina, Foteini, Eva, Ali, Leonid, Jiquan, Sumit, Tashfeen, Martina, Jun Li, Lam, Nico, and Stefano.

Sincere thanks to my unique, weird and lovely friends, Thanasis, S. Aggelos, M. Aggelos, Giorgos and Vaso for being there and believing in me. Words are not enough to express my gratitude.



Special thanks to Georgia that supported me, encouraged me and helped me to overcome every kind of difficulty during the last years. As a pillar of strength, she was there for me in every step of the way, and I entirely appreciate everything she had done for me.

Last but not least, I would like to thank from the bottom of my heart my father Γιώργο, my mother Αγνή and my sister Έλλη, for always supporting and believing in me throughout my years of studies.

«The acceptance of Doctoral Dissertation from the Department of Materials Science and Engineering of University of Ioannina, Greece, does not imply the acceptance of the author's opinion.» (Law 5343/1932, article 202).



# Publications

During these past six years I have contributed to 28 projects. The ones I have chosen to include in this dissertation are marked with \*.

1. *Gd(III)-doped carbon dots as a dual fluorescent-MRI probe*, A. B. Bourlinos, A. Bakandritsos, A. Kouloumpis, D. Gournis, M. Krysmann, E. P. Giannelis, K. Polakova, K. Safarova, K. Hola, R. Zboril, *Journal of Materials Chemistry*, (2012) 22, 44, 23327-23330.

2. *Aqueous-dispersible fullerol-carbon nanotube hybrids*, A. B. Bourlinos, V. Georgakilas, A. Bakandritsos, **A. Kouloumpis**, D. Gournis, R. Zboril, *Materials Letters* (2012) 82, 48-50.

3. *Synthesis, characterization and non-linear optical response of organophilic carbon dots*, A. B. Bourlinos, M. A. Karakassides, **A. Kouloumpis**, D. Gournis, A. Bakandritsos, I. Papagiannouli, P. Aloukos, S. Couris, K. Hola, R. Zboril, M. Krysmann, E. P. Giannelis, *Carbon*, (2013) 61, 640-643.

4. *Tuning the Dispersibility of Carbon Nanostructures from Organophilic to Hydrophilic: Towards the Preparation of New Multipurpose Carbon-Based Hybrids*, V. Georgakilas, **A. Kouloumpis**, D. Gournis, A. Bourlinos, C. Trapalis, R. Zboril, *Chemistry - A European Journal*, (2013) 19, 12884-12891.

5. *Wetting behavior of plasma treated low-k films in dHF cleans solutions*, T.S. Smith, K.M. Lynch, C.M. Cooper, O. Okobiah, E. Osei-Yiadom, M. Bischof, **A. Kouloumpis**, M. Baikousi, K. Dimos, R.F. Reidy, *Microelectronic Engineering* 128 (2014) 79-84.

6. *Performance of layer-by-layer deposited low dimensional building blocks of graphene-prussian blue onto graphite screen-printed electrodes as sensors for hydrogen peroxide*, A. Michopoulos, **A. Kouloumpis**, D. Gournis, M. I. Prodromidis, *Electrochimica Acta* 146 (2014) 477-484.

7. *Green and simple route toward boron doped carbon dots with significantly enhanced non-linear optical properties*, A. B. Bourlinos, G. Trivizas, M. A. Karakassides, M. Baikousi, **A. Kouloumpis**, D. Gournis, A. Bakandritsos, K. Hola, O. Kozak, R. Zboril, I. Papagiannouli, P. Aloukos, S. Couris, *Carbon* 83 (2015) 173-179.

8. *Hydrophilic nanotube supported graphene-water dispersible carbon superstructure with excellent conductivity*, V. Georgakilas, A. Demeslis, E. Dararas, **A. Kouloumpis**, K. Dimos, D. Gournis, M. Kocman, M. Otyepka, R. Zboril, *Advanced Functional Materials*, 25 (10) (2015) 1481-1487.

9.\* *A bottom-up approach for the synthesis of highly ordered fullerene-intercalated graphene hybrids*, **A. Kouloumpis**, K. Spyrou, K. Dimos, V. Georgakilas, P. Rudolf, D. Gournis, *Frontiers in Materials* (2015), 2, 10.

10. *In situ growth of capping-free magnetic iron oxide nanoparticles on liquid-phase exfoliated graphene*, T. Tsoufis, Z. Syrgiannis, N. Akhtar, M. Prato, F. Katsaros, Z. Sideratou, **A. Kouloumpis**, D. Gournis, P. Rudolf, *Nanoscale*, (2015) 7, 8995-9003.

11. *Highly dispersible disk-like graphene nanoflakes*, V. Georgakilas, K. Vrettos, K. Katomeri, **A. Kouloumpis**, K. Dimos, D. Gournis and R. Zborilc, *Nanoscale*, (2015), 7, 15059.

12. *Introduction of micronuclei by multi-walled carbon nanotubes interacting with humic acids in cultured human*, M. S. Vidali, E. Bletsas, **A. Kouloumpis**, C. G. Skoutelis, Y. Deligiannakis, D. Gournis, D. Vlastos, *Environ. Sci.: Nano*, (2016) 3, 74.

13. *Carbon nanostructures containing polyhedral oligomeric silsesquioxanes (POSS)*, G. Potsi, A. Rossos, **A. Kouloumpis**, M. K. Antoniou, K. Spyrou, M. A. Karakassides, D. Gournis, P. Rudolf, *Current Organic Chemistry*, (2016) 20(6): 662-673.

14. *Functionalized graphene oxide nanomaterials as supports for stabilization of cytochrome c*, M. Patila, I. V. Pavlidis, **A. Kouloumpis**, K. Dimos, K. Spyrou, P. Katapodis, D. Gournis, H. Stamatis, *International Journal of Biological Macromolecules*, (2016), 84, 227-235.

15. *Laccase-functionalized graphene oxide assemblies as efficient nanobiocatalysts for oxidation reactions*, M. Patila, **A. Kouloumpis**, D. Gournis, P. Rudolf, H. Stamatis, *Sensors (Basel)*, (2016), 16 (3), 287.
16. *Unexpected orbital magnetism in Bi-rich Bi<sub>2</sub>Se<sub>3</sub> nanoplatelets*, H. J. Kim, M. S. Katsiotis, S. Alhassan, I. Zafiropoulou, M. Pissas, Y. Sanakis, G. Mitrikas, N. Panopoulos, N. Boukos, V. Tzitzios, M. Fardis, J. G. Kim, S. G. Lee, Y. M. Kim, S. J. Yoo, J. H. Lee, **A. Kouloumpis**, D. Gournis, M. Karakassides, G. Papavassiliou, *NPG Asia Mater* (2016), 8, e271.
17. *Determination of phenolic compounds using spectral and color transitions of rhodium nanoparticles*, V. Gatselou, D. C. Christodouleas, **A. Kouloumpis**, D. Gournis, D. L. Giokas, *Analytica Chimica Acta*, (2016), 932, 80-87.
18. *Graphene nanobuds: synthesis and selective organic derivatisation*, V. Georgakilas, A. B. Bourlinos, E. Ntararas, A. Ibraliu, D. Gournis, K. Dimos, **A. Kouloumpis**, R. Zboril, *Carbon* (2016), 110, 51-55.
19. *Fe(III)-functionalized carbon dots - highly efficient photoluminescence redox catalyst for hydrogenations of olefins and decomposition of hydrogen peroxide*, A. B. Bourlinos, A. K. Rathi, M. B. Gawande, K. Hola, A. Goswami, S. Kalytchuk, M. A. Karakassides, **A. Kouloumpis**, D. Gournis, Y. Deligiannakis, E. P. Giannelis, R. Zboril, *Applied Materials Today* (2017), 7, 179-184.
- 20.\* *Graphene/Carbon-dot hybrid thin films prepared by a modified Langmuir-Schaefer method*, **A. Kouloumpis**, E. Thomou, N. Chalmpes, K. Dimos, K. Spyrou, A. B. Bourlinos, I. Koutselas, D. Gournis, P. Rudolf, *ACS Omega* (2017), 2 (5), 2090-2099.
21. *Fullerol-Graphene Nanobuds: Novel Water Dispersible and Highly Conductive Nanocarbon for Electrochemical Sensing*, A. B. Bourlinos, V. Georgakilas, V. Mouselimis, **A. Kouloumpis**, E. Mouzourakis, A. Koutsioukis, M-K. Antoniou, D. Gournis, M. A. Karakassides, Y. Deligiannakis, V. Urbanova, K. Cepe, A. Bakandritsos, R. Zboril, *Applied Materials Today* (2017), 9, 71-76.
22. *Top-down and bottom-up approaches to transparent, flexible and luminescent*

*nitrogen-doped carbon nanodots-clay hybrid films*, K. Dimos, F. Arcudi, **A. Kouloumpis**, I. Koutselas, P. Rudolf, D. Gournis, M. Prato, *Nanoscale* (2017), DOI: 10.1039/C7NR02673K

23. *Hydrophilic oxidized carbon nanodiscs: A promising multifunctional material for bioapplications*, P. Zygouri, T. Tsoufis, **A. Kouloumpis**, M. Patila, G. Potsi, A. A. Sevastos, Z. Sideratou, F. Katsaros, G. Charalambopoulou, H. Stamatis, P. Rudolf, T. A. Steriotis, Dimitrios Gournis. **(Submitted)**

24.\* *Controlled deposition of fullerene derivatives within a graphene template by means of a modified Langmuir-Schaefer method*, **A. Kouloumpis**, N. Vourdas, P. Zygouri, V. Kostas, N. Chalmpes, G.Potsi, K. Spyrou, V. Stathopoulos, P. Rudolf, D. Gournis. **(Submitted)**

25.\* *Synthesis of 2D germanane (GeH): a new, fast and facile approach*, T. Giousis, G. Potsi, **A. Kouloumpis**, K. Spyrou, N. Chalmpes, K. Dimos, M. K. Antoniou, G. Papavassiliou, A. Bourlinos, H. J. Kim, H. Stamatis, G. Blake, D. Gournis, P. Rudolf. **(to be submitted)**

26.\* *Extraordinary antimicrobial activity of germanane monolayer films*, **A. Kouloumpis**, N. Vourvou, N. Chalmpes, T. Giousis, P. Katapodis, H. Stamatis, P. Rudolf, D. Gournis. **(to be submitted)**

27. *In-situ formation of molecularly thin Mn-Fe Prussian Blue analogues on a layered double hydroxide monolayer by means of a Langmuir-Schaefer approach*, M. Katsiaflaka, **A. Kouloumpis**, R. Y. N. Gengler, G. Potsi, K. Spyrou, M. Prodromidis, A. Siozios, P. Patsalas, R. J. D. Miller, D. Gournis. **(to be submitted)**

## **BOOK CHAPTERS**

1.\* **A. Kouloumpis**, P. Zygouri, K. Dimos, D. Gournis, (2014) *Layer-by-layer assembly of graphene-based hybrid materials*, 2014, (ed. V. Georgakilas), Chapter 11, pp. 359-399, **Wiley-VCH Verlag GmbH & Co. KGaA**, Weinheim, Germany, ISBN-9783527672790, DOI: 10.1002/9783527672790. **(Invited)**

# Curriculum Vitae

## Honours - Scholarships

- Oral presentation award for the talk “*A bottom-up synthesis of transparent flexible clay-carbon dot hybrid films*” at the 7<sup>th</sup> PanHellenic Symposium on Porous Materials, University of Ioannina, 2-4 June 2016, Ioannina, Greece.
- Poster award at the 6<sup>th</sup> PanHellenic Symposium on Porous Materials for the poster “*Graphene/Fullerene hybrid thin films by a modified Langmuir-Schaefer method*”, T.E.I. Kavala, 9-11 September 2013, Kavala, Greece.
- Scholarship from the Christodoulou Euthimiou Foundation during undergraduate studies (2004-2009) at the Department of Materials Science and Engineering, at University of Ioannina, Greece.

## Contributions to Conferences

1. 5<sup>th</sup> PanHellenic Symposium on Porous Materials, 31 June-1 July 2011, Heraklion, Crete, Greece, poster presentation: *Synthesis, characterization and thermal properties analysis of nylon 6.10 nanocomposites with layered materials*, (**A. Kouloumpis**, E. K. Diamanti, A. Enotiadis and D. Gournis).
2. 6<sup>th</sup> PanHellenic Symposium on Porous Materials, 9-10 September 2013, Kavala, Greece, poster presentation: *Graphene/Fullerene hybrid thin films by a modified Langmuir-Schaefer method*, (**A. Kouloumpis**, K. Spyrou, K. S. Triantafyllidis and D. Gournis) (**Best poster presentation award**).
3. 5<sup>th</sup> PanHellenic Symposium on Green Chemistry and Sustainable Development, 30/10-1/11/2014, Ioannina, Greece, poster presentation: *A bottom-up approach for the synthesis of highly ordered fullerene-intercalated graphene hybrids*, (**A. Kouloumpis**, P. Zygouri, G. Potsi, K. Spyrou, K. Dimos, M. A. Karakassides and D. Gournis).

4. E-MRS 2016 Spring Meeting, 2-6 May 2016, Lille, France, poster presentation: *Graphene/C-dots hybrid thin films by a modified Langmuir-Schaefer method*, (**A. Kouloumpis**, E. Thomou, K. Dimos, I. Koutselas, D. Gournis and P. Rudolf).
5. 7<sup>th</sup> Panhellenic Symposium on Porous Materials, 2-4 June 2016, Ioannina, Greece, oral contribution: *A bottom-up synthesis of transparent flexible clay-carbon dot hybrid films*, (**A. Kouloumpis**, K. Dimos, F. Arcudi, I.B. Koutselas, M. Prato, P. Rudolf and D. Gournis). (**Best oral presentation award**)
6. Condensed Matter (CMD16), 4-9 September 2016, Groningen, The Netherlands, oral contribution: *Fullerene-intercalated graphene hybrid thin films by a modified Langmuir-Schaefer approach*, (**A. Kouloumpis**, P.Zygouri, K. Spyrou, P. Rudolf D. Gournis).

### **Teaching Experience**

- Research guidance and supervision for 9 Diploma Theses (final semester research projects) of undergraduate students relevant to my research interests at the Department of Materials Science and Engineering, University of Ioannina, Greece, during years 2013-2016.
- Teaching Assistant for the courses *Chemistry Lab*, *Materials Lab II* and *Physical Chemistry Lab* at the Department of Materials Science and Engineering, University of Ioannina, Greece, during the academic years: 2010-2011, 2011-2012, 2012-2013, 2013-2014, 2014-2015 and 2015-2016.